



Title	A Study on Optical Fiber Characterization Method for Space Division Multiplexing Transmission Line Utilizing Swept-Frequency Interferometer
Author(s)	大野, 慎悟
Citation	北海道大学. 博士(工学) 乙第7061号
Issue Date	2018-09-25
DOI	10.14943/doctoral.r7061
Doc URL	<a href="http://hdl.handle.net/2115/71853">http://hdl.handle.net/2115/71853</a>
Type	theses (doctoral)
File Information	Shingo_Ohno.pdf



[Instructions for use](#)

**Doctoral thesis**

**A Study on Optical Fiber Characterization  
Method for Space Division Multiplexing  
Transmission Line Utilizing  
Swept-Frequency Interferometer**

**September 2018**

**Shingo Ohno**

**Graduate School of Engineering  
Hokkaido University**



*This thesis is based on the research work conducted at Access Network Service Systems  
Laboratories, NIPPON TELEGRAPH and TELEPHONE (NTT) Corporation.*





# Contents

<b>1. Introduction.....</b>	<b>1</b>
1.1. Background.....	1
1.2. Space division multiplexing technology.....	3
1.3. Characterization of SDM transmission line.....	6
1.4. Objective and outline of this thesis.....	10
<b>2. Rayleigh backscattering signature measured with C-OFDR .....</b>	<b>15</b>
2.1. Introduction.....	15
2.2. Measurement principles.....	18
2.3. Experimental setup.....	22
2.4. Experimental results and discussion.....	24
2.5. Conclusion.....	36
<b>3. Distributed measurement of differential mode delay along few-mode fiber.....</b>	<b>37</b>
3.1. Introduction.....	37
3.2. Measurement principle.....	39
3.3. Experimental setup.....	41
3.4. Experimental results.....	44
3.5. Conclusion.....	48

<b>4. Distributed measurement of spatial mode dispersion along coupled multicore fiber.....</b>	<b>49</b>
4.1. Introduction .....	49
4.2. Measurement principles .....	51
4.3. Experimental setup.....	58
4.4. Experimental results and discussion .....	62
4.5. Conclusion.....	69
<b>5. High-resolution measurement of differential mode delay of few-mode fiber link.....</b>	<b>71</b>
5.1. Introduction .....	71
5.2. Measurement principles .....	73
5.3. Experimental setup and results .....	80
5.4. Conclusion.....	88
<b>6. Summaries and conclusions.....</b>	<b>89</b>
<b>Appendix.....</b>	<b>93</b>
Appendix A. C-OFDR beat signal with one-dimensional scatter model .....	93
Appendix B. Auto-correlation of Rayleigh backscattering amplitude in coupled multicore fiber .....	95
Appendix C. FMCW phase signal with mode coupling.....	97

*Contents*

<b>References .....</b>	<b>101</b>
<b>List of figures.....</b>	<b>113</b>
<b>List of acronyms .....</b>	<b>117</b>
<b>Acknowledgements .....</b>	<b>119</b>
<b>List of publications and awards .....</b>	<b>121</b>



# 1. Introduction

## 1.1. Background

In the 1980s, optical fiber transmission lines were deployed using single-mode fibers (SMFs) with the aim of providing broadband communications economically [1-1], [1-2]. The first fiber-to-the-home (FTTH) service was introduced in 1997, and now the number of FTTH subscribers in Japan is about to reach 30 million [1-3]. Optical fiber links also play a role in the backbone networks of mobile communications including 4G/LTE, which has rapidly become widely used along with smartphones in recent years, and the number of 4G/LTE subscribers in Japan has exceeded 110 million [1-3]. With the expansion of broadband services, data traffic in transmission lines has inevitably grown. To meet the growing demand for broadband communications, large-capacity transmission systems have been developed with signal multiplexing technologies. Figure 1-1 shows the evolution of the transmission capacities of commercial systems [1-4], [1-5]. During the first decade, the transmission capacity per fiber was expanded mainly by using time-division multiplexing (TDM) technology. In the 1990s, wavelength-division multiplexing (WDM) technology was developed [1-6], and it enabled the transmission capacity to be further increased. Moreover, digital coherent technology [1-7], which utilizes the phase and polarization of light for signal transmission in addition to its amplitude, has boosted transmission capacity to a higher level with the convergence of TDM and WDM. However, the launched optical power must inevitably increase to meet the growth in capacity, while it must be limited to avoid nonlinear effects or a fiber fuse [1-8]. The achievable capacity in SMF is fundamentally limited to around 100 Tbit/s/fiber, which is imposed by the optical

power limit and Shannon's information theory [1-9]. In terms of research activity, the SMF-based transmission capacity has already reached its fundamental limit [1-10]. New signal multiplexing technologies based on new-structure fibers will be necessary for any further enhancement of transmission capacity.

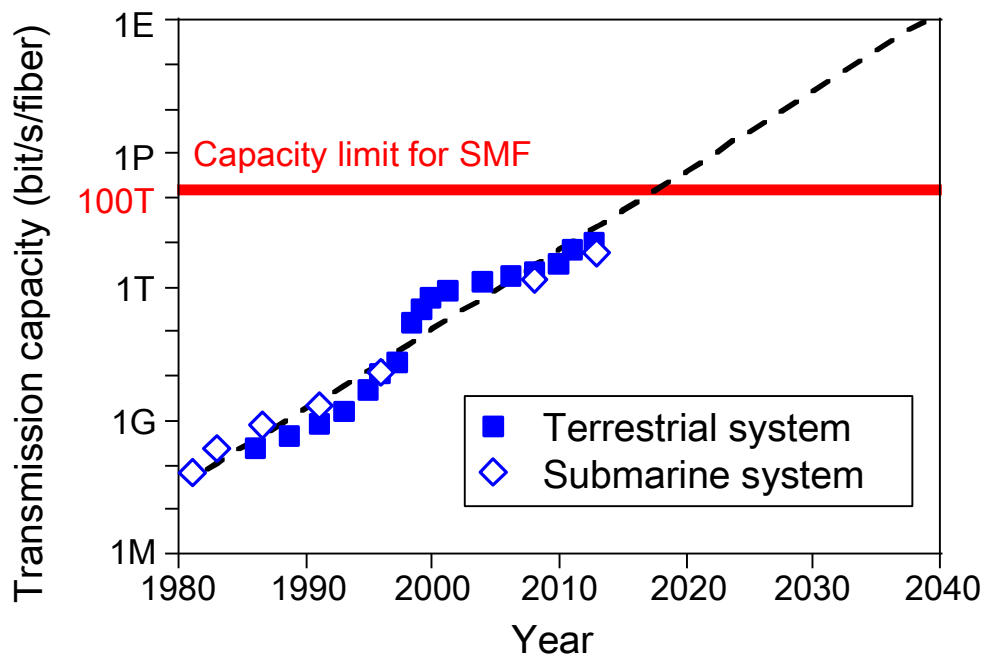


Figure 1-1. Evolution of transmission capacities in commercial systems.

## 1. Introduction

### 1.2. Space division multiplexing technology

With a view to exceeding the capacity limit of SMF, space division multiplexing (SDM) technologies, including mode-division multiplexing (MDM) using few-mode fibers (FMFs) [1-11], [1-12] and/or core-multiplexing using multicore fibers (MCFs) [1-13]-[1-15], have attracted considerable attention. With SDM, transmitted signals are multiplexed with multiple propagation modes or cores called "spatial channels". The concept of SDM is almost as old as optical fiber communication itself. The first approach using MCF was reported in 1979 [1-13], and the MDM concept was proposed in 1982 [1-11]. In recent years, SDM studies have rapidly progressed because of the convergence of an enabling technology and the demand for transmission capacity. In 2017, a 10 Pbit/s/fiber transmission using 114 spatial channels (6 modes x 19 cores) was reported [1-16].

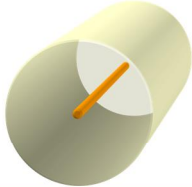
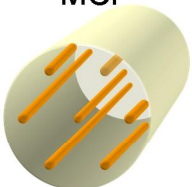
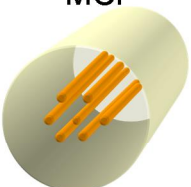
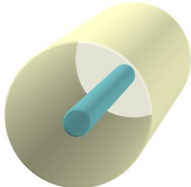
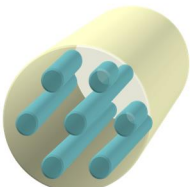
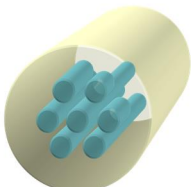
Figure 1-2 shows an overview of SDM fibers. SDM fibers can be categorized into few-mode, multicore, and combined types [1-4], [1-15].

FMF, which is designed with a larger core radius and/or a larger refractive index difference between the core and cladding than SMF, supports multiple propagation modes that satisfy the boundary condition. Under a weakly-guiding approximation [1-17], the propagation modes can be categorized into "linearly polarized (LP) mode" groups. Figure 1-3 shows the optical intensity distribution of each LP mode in the fiber cross-section. As regards the  $LP_{ml}$  mode, the suffixes  $m$  and  $l$  are related to the mode order of angular and radial coordinates, respectively. The  $LP_{01}$  mode is the fundamental mode, and the others are the higher-order modes. In most case of MDM, each signal is transmitted in an arbitrary LP mode by using a mode multiplexer/demultiplexer (MUX/DEMUX) [1-18], [1-19].

MCFs can be divided into non-coupled and coupled MCFs. In a non-coupled MCF,



whose core pitch is sufficiently large to suppress inter-core crosstalk (XT), each core acts as an independent transmission path. On the other hand, coupled MCF has a lower core pitch and a larger inter-core XT compared with non-coupled MCF, while the inter-core XT can be compensated for by employing multiple-input multiple-output (MIMO) processing at the receiver [1-14], [1-15]. MIMO processing is also adopted in most FMF-based SDM transmissions, because the propagation modes in FMFs are sensitively coupled with each other as a result of structural imperfections or the bending/twisting condition [1-12]. As we increase the number of spatial channels in SDM, more complex MIMO processing is needed to extract each signal.

	Single core	Multicore	
		Non-coupled	Coupled
Single mode	SMF 	Non-coupled MCF 	Coupled MCF 
Few mode	FMF 	Non-coupled FM-MCF 	Coupled FM-MCF 

**SDM fibers**

Figure 1-2. SDM fibers.

1.2. Space division multiplexing technology

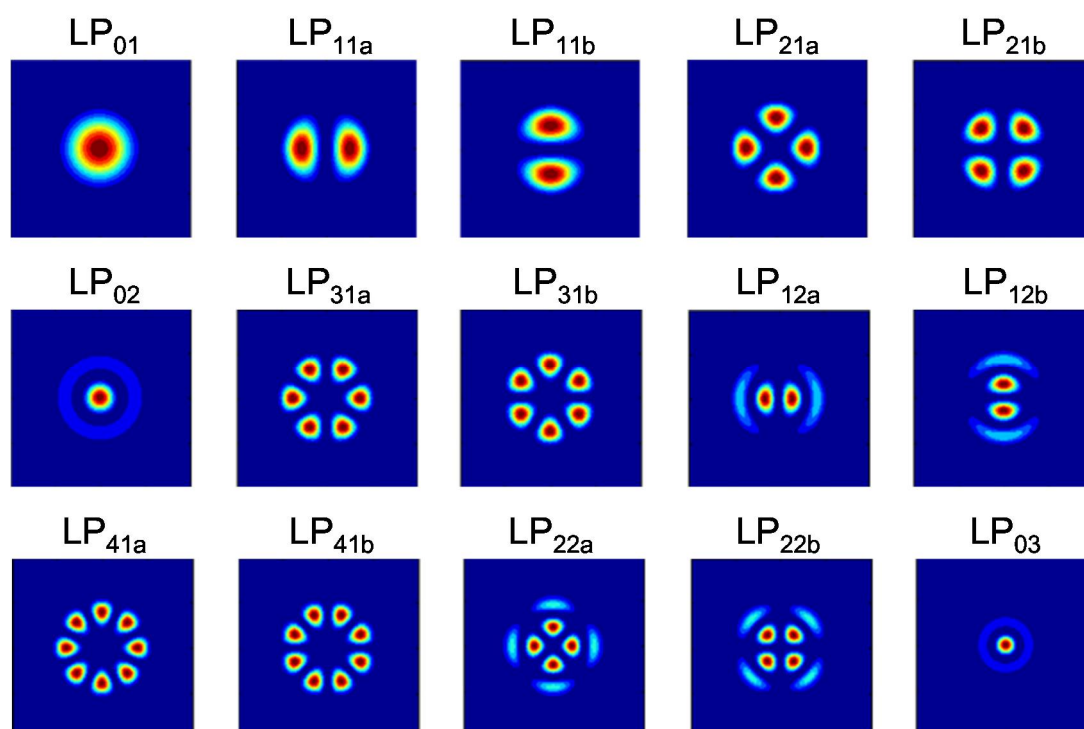


Figure 1-3. Optical intensity distribution of each LP mode.

### 1.3. Characterization of SDM transmission line

With SDM, in contrast to the capacity benefit, the transmission performance is critically affected by spatial channel-dependent parameters, namely differential loss, XT, and differential delay between spatial channels. The maximum optical loss among spatial channels restricts the transmission distance in SDM, however, an optical amplifier or mode scrambling technique can mitigate the effect of differential loss [1-20]. Although XT degrades the purity of transmitted signals, it can be compensated for by applying MIMO processing at the receiver. The differential delay between spatial channels, or the resulting delay spread, causes a difference in detection timing, or an increase in the tap number of FIR filters in MIMO processing [1-21]. The differential delay can be managed by concatenating fibers whose differential delays have opposite signs [1-22], however, this is difficult to realize in an actual transmission line. This is because individual fiber lengths cannot be precisely adjusted since they depend on the geometrical layout of facilities. Moreover, the differential delay changes sensitively due to the fiber bending and twisting condition [1-23], [1-24], thus the actual value of the differential delay cannot be precisely predicted before the construction of a transmission line. Therefore, to confirm the transmission performance or estimate the MIMO complexity, it is very important to measure the differential delay in many scenarios including the construction and maintenance of the transmission line.

There are several methods for measuring the differential delay, including a time-domain method [1-25], and a frequency-domain method [1-26]-[1-28]. The time-domain method, which is generally called impulse response measurement, is standardized in Ref. [1-25] and has been widely used in previous work. Figure 1-4 shows the basic setup for impulse response measurement. This method launches a short optical pulse into the fiber under test (FUT), and characterizes the differential delay

### *1.3. Characterization of SDM transmission line*

from the shape of the output pulse. Thus the temporal pulse width corresponds to the delay resolution, and is typically a few tens of picoseconds. However, the setup needs complicated and expensive instruments including a fast detector and a sampling oscilloscope for high-resolution measurement. In contrast, the frequency-domain method, which is called the frequency-modulated continuous wave (FMCW) method, is very attractive because the measurements can be easily performed by using a simple Mach-Zehnder interferometer and a frequency-sweeping continuous light source. Figure 1-5 shows the basic setup of the FMCW method. The FMCW method can be performed with transmission and reflection type configurations. The reflection-type FMCW method is often called coherent optical frequency-domain reflectometry (C-OFDR) [1-29], [1-30]. With the FMCW method, a continuous light wave whose frequency is swept linearly with respect to time is divided by an optical coupler, and used as local and probe lights. The probe light propagates through the FUT, and the transmitted/end-reflected light is coherently detected with the local light. Then, the frequency of the detected beat signal is proportional to the propagation delay time, thus an impulse response-like waveform can be obtained by analyzing the spectrum of the beat signal as shown in Fig. 1-6. With the FMCW method a slower detector can be adopted to detect the beat signal (generally slower than 1 GHz) than with the time-domain method. Moreover, the delay resolution of the FMCW method can be easily improved by expanding the frequency sweep range, because it is inversely proportional to the frequency sweep range. References [1-26] and [1-27] report ps-order resolution measurements using the FMCW method.

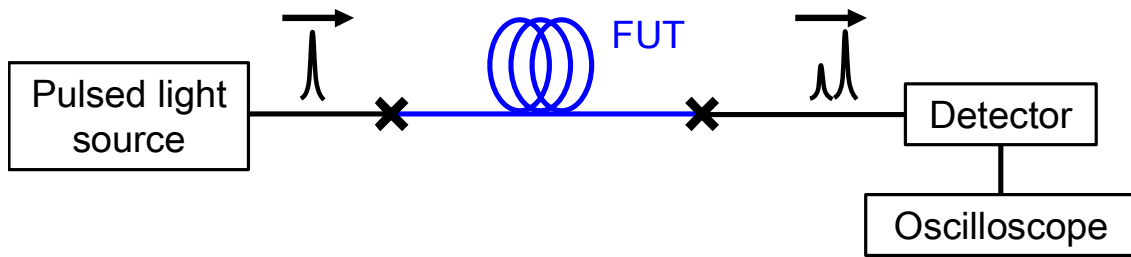


Figure 1-4. Basic setup of impulse response measurement.

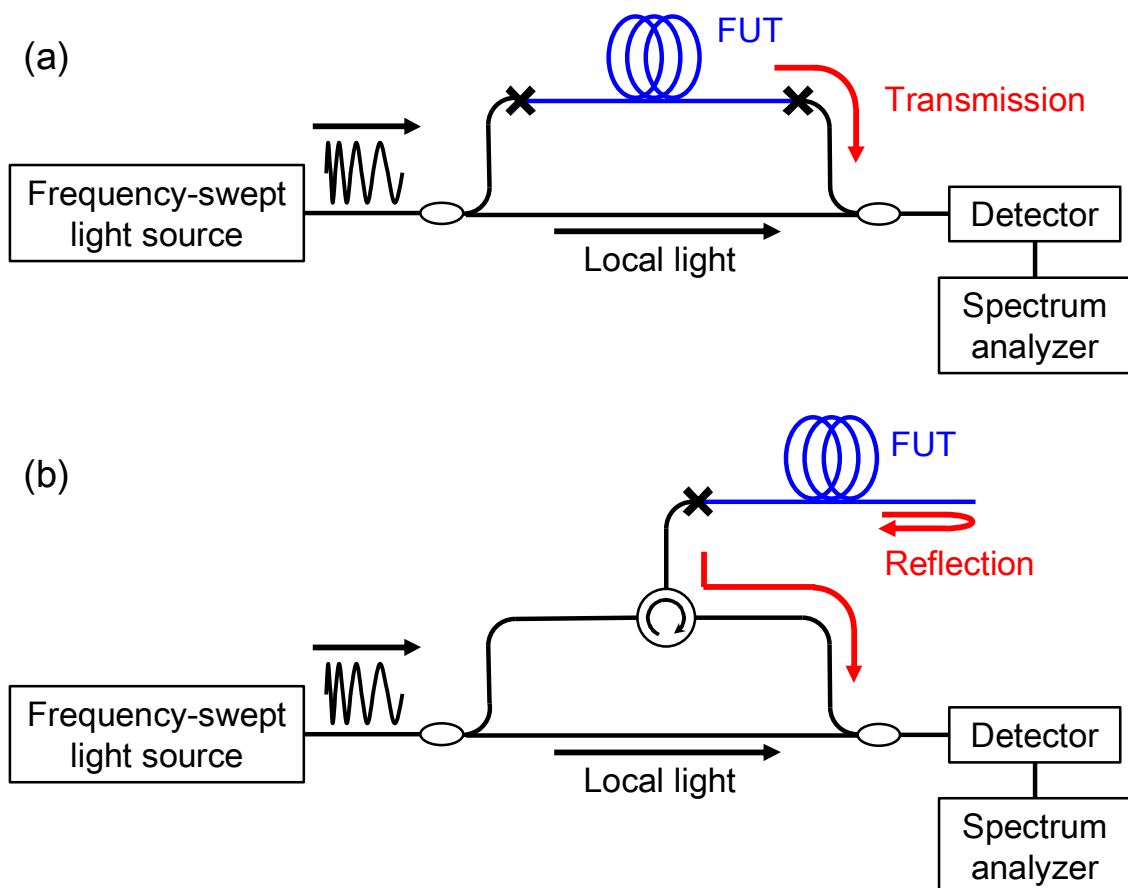


Figure 1-5. Basic setup of FMCW method. (a) Transmission and (b) reflection types.

1.3. Characterization of SDM transmission line

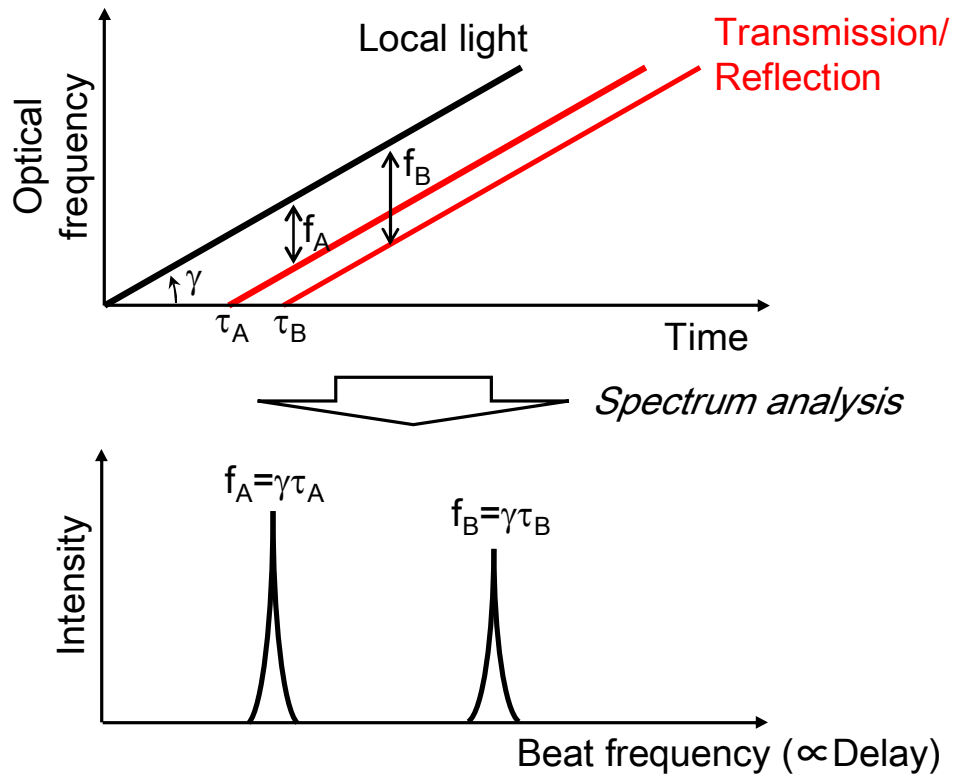


Figure 1-6. Schematic diagram of measurement principle with FMCW method.

## 1.4. Objective and outline of this thesis

The conventional method characterizes the total propagation delay of end-to-end SDM fiber link. However, the local differential delay values, or delay accumulation process along the fiber, cannot be measured without cutting the fiber at an arbitrary position, while the differential delay is expected to change locally due to fiber bending or twisting caused by cabling or cable installation. If we could measure the differential delay at arbitrary fiber positions non-destructively, it would constitute a powerful tool for characterizing SDM transmission line in many scenarios such as when identifying fiber portions that affect the end-to-end characteristic, which is essential for system design.

On the other hand, improving the fundamental performance of the delay measurement itself is also important for characterizing SDM transmission line. In recent work, differential delay reduction techniques including FMFs designed with graded-index based profiles [1-31], [1-32] and a differential delay managed transmission line [1-22] have been aggressively studied. High-resolution delay measurements are required if we are to characterize such low-differential delay transmission lines accurately.

The main purpose of this thesis is to realize the effective maintenance and management of future optical fiber networks by expanding and improving the capability of differential delay measurement for SDM transmission line. Figure 1-7 is a schematic illustration of the study approaches employed in this thesis. There are basically two kinds of approaches:

- (1) Realizing the distributed measurement of differential delay/delay spread,
- (2) Improving the resolution of differential delay measurement.

#### *1.4. Objective and outline of this thesis*

In this thesis, I focus on the FMCW method and its utilization, because it has the potential for meeting the above challenges with a simple configuration. The techniques described in this thesis are performed mainly with signal processing after acquiring FMCW beat signals, thus they can be easily applied to the conventional FMCW setup.

Figure 1-8 shows the organization of this thesis, which consists of 6 chapters. Chapter 1 is an introduction including an overview of SDM transmission and its characterization method. Chapters 2 to 4 relate to the distributed measurement of differential delay and delay spread for both non-coupled and coupled SDM fibers. Chapter 5 concerns a technique that improves the delay resolution of the FMCW method.

After this introduction, chapter 2 describes the basic principle of C-OFDR (reflection-type FMCW method) for measuring the Rayleigh backscattering signature, which is utilized for the distributed measurement of the differential delay in SDM fiber. The fundamental characteristics of the Rayleigh backscattering signature are also described in this chapter. Then, a signal processing technique for improving the repeatability of the backscattering signature degraded by laser phase noise is demonstrated with several experiments including long-range measurement in a temperature-changing environment.

In chapter 3, the distributed measurement of differential mode delay (DMD) along a FMF is proposed and demonstrated using the Rayleigh backscattering signature with the signal processing technique described in chapter 2. This measurement method is realized by carrying out the C-OFDR measurement with each propagation mode of an FMF, and comparing the delay times, which correspond to the fiber position where the backscattering signature spectrally shifts due to environmental disturbances.



In chapter 4, which focuses on the characterization of coupled-MCF, the distributed measurement of spatial mode dispersion (SMD), namely the delay spread caused by differential mode delay and mode coupling, is proposed and demonstrated. Rayleigh backscattering measurement with C-OFDR is also performed with coupled MCF, and local SMDs are characterized by auto-correlating the backscattering amplitude at arbitrary fiber positions. This chapter also describes a technique for improving the measurement accuracy of this method.

Chapter 5 describes the high-resolution end-to-end measurement of DMD in an FMF link. The high-resolution measurement is performed by comparing the temporal phase variations of beat signals with different modes obtained with a transmission-type FMCW method. This chapter also discusses the effect of mode coupling on this measurement and a technique for its reduction.

Chapter 6 concludes this thesis. I summarize the results obtained in this study for the characterization of SDM transmission line.

1.4. Objective and outline of this thesis

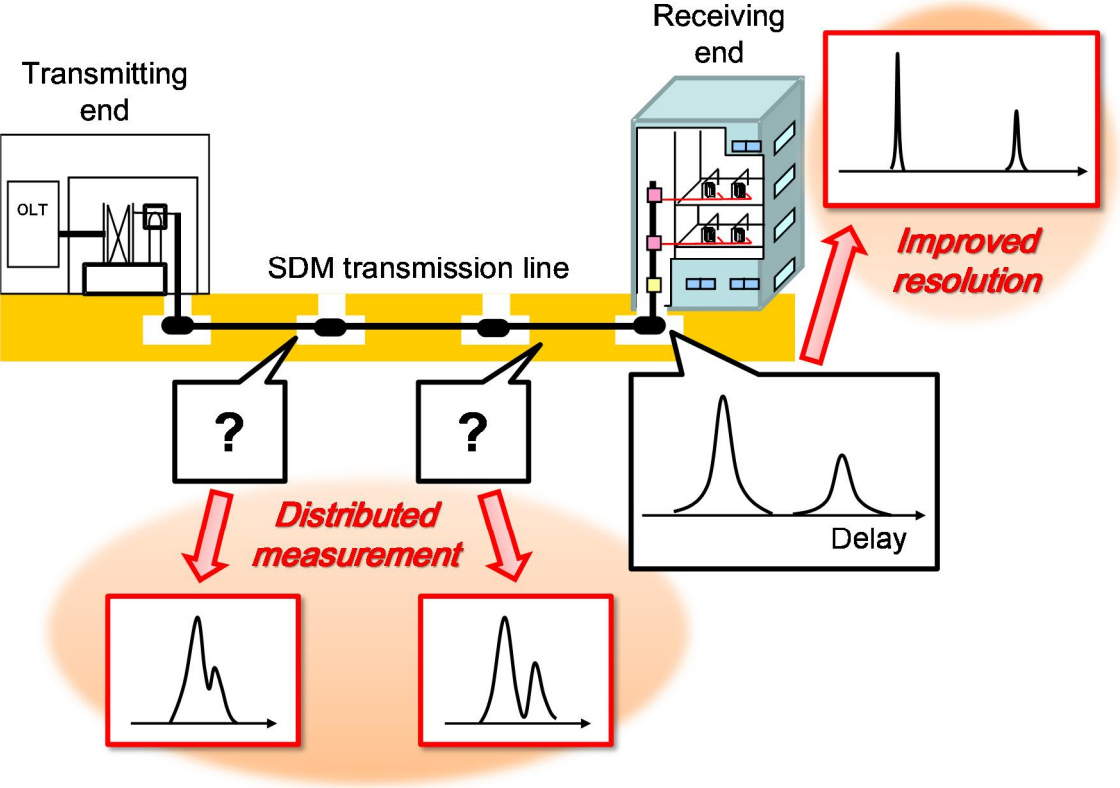


Figure 1-7. Study approaches in this thesis.

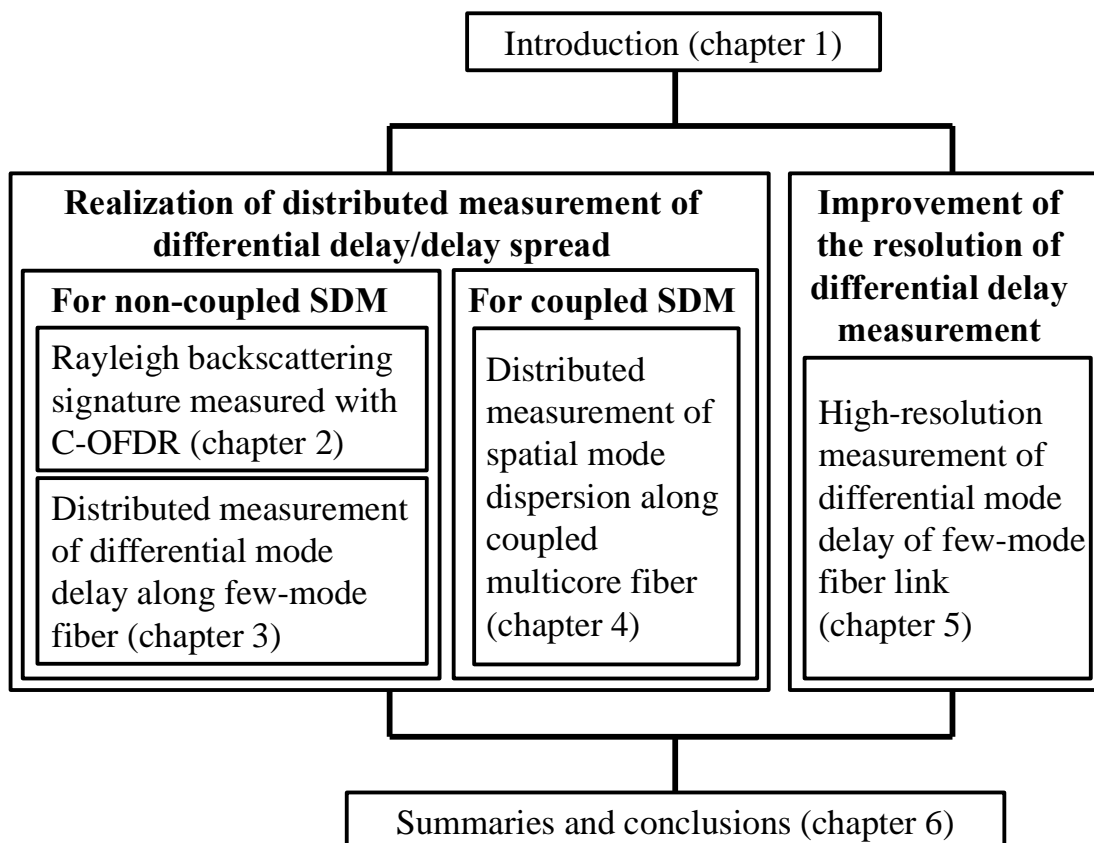


Figure 1-8. Thesis organization.

## 2. Rayleigh backscattering signature measured with C-OFDR

### 2.1. Introduction

Rayleigh scattering measurements performed using an optical reflectometer have been widely used for fault detection and evaluation in optical fiber networks and optical components [2-1]-[2-3]. Recently, some attractive applications of Rayleigh scattering measurement including a fiber identification [2-4], highly sensitive temperature or strain sensing [2-4]-[2-6], and 3D shape sensing [2-7] have been proposed. In these applications, a randomly jagged scatter amplitude waveform which is measured by employing optical reflectometry with coherent detection is used as a "signature" for identification or sensing. The origin of the jagged appearance is interference between Rayleigh backscatters caused by random refractive indices generated when fiber is manufactured [2-8]. The measured waveforms are thus identical and unique for individual fibers and for fiber segments when the fiber and measurement conditions are the same. In the applications mentioned above, the signature must be measured with high repeatability.

Certain methods have been proposed for measuring the Rayleigh scatter signature. Reference [2-5] proposed a highly-sensitive temperature measurement using coherent optical time domain reflectometry (C-OTDR) with a gas-stabilized distributed feedback laser whose frequency was precisely controlled. This approach makes it possible to perform measurements on long fibers (over tens of kilometers) with a temperature resolution of 0.01 °C and a spatial resolution of one meter. However, the C-OTDR setup is complex, especially as regards frequency stabilization and control

## *2. Rayleigh backscattering signature measured with C-OFDR*

when the aim is to achieve measurements with high repeatability. Moreover, it requires a lot of time to undertake many measurements at different laser frequencies. In contrast, an approach using C-OFDR (reflection-type FMCW method) is very attractive because Rayleigh backscatter responses in both the time and spectral domains are easily and quickly obtained by sweeping the optical frequency of the laser. For this reason, C-OFDR is now the most common approach for scatter signature applications [2-4], [2-6], [2-7]. However, the use of C-OFDR for scatter signature applications is limited to short measurement ranges (up to several hundred meters) since scatter signature repeatability is not maintained for long fibers beyond the laser coherence length due to laser phase noise. The expansion of the scatter signature measurement range with C-OFDR would be useful as it would mean the possibility of using the approach for identification or sensing in, for example, telecommunication-scale fiber networks.

In this chapter, as a basis of the SDM characterization method described in chapter 3, I present a way to realize scatter signature measurements with C-OFDR for the range beyond the laser coherence length. The laser phase noise limitation is overcome by introducing the optical power spectrum of local Rayleigh backscatter as the signature. I also investigate the influence of the remaining phase noise on the repeatability of the proposed method with various measurement ranges and spatial resolutions. In addition, I employ signal averaging for the proposed method to enhance the repeatability degraded by the detector noise for long-range measurement and discuss the effect of signal averaging on the proposed method. With this method, I demonstrate distributed spectral shift measurement of the backscattering signature over a 100-km range with a temperature sensitivity of better than 0.01 °C and confirm the potential for long-scale applications.

This chapter is organized as follows. Section 2.2 reviews the theoretical background

## *2.1. Introduction*

to the scatter signature measurements with C-OFDR using the conventional and proposed methods. Section 2.3 describes the C-OFDR configuration I used in the experiment. Section 2.4 includes our experimental results and discussion, and Section 2.5 provides the conclusion of this chapter.

## 2.2. Measurement principles

### 2.2.1. Complex scatter spectrum with conventional method

In this section, I review the principle of the conventional method used to obtain the scatter signature with C-OFDR.

Figure 2-1 shows an example of a C-OFDR setup. A continuous light wave whose frequency is swept with respect to time is divided by the coupler and used as probe and local lights, and the backscattered lights are mixed and then detected by a coherent receiver. Then, the beat signal  $I_R(t)$  produced by the interference between the local and backscattered lights can be written as [2-9], [2-10] (see Appendix A.)

$$I_R(t) \propto \sum_{i=1}^M a_{R,i} \cos \left[ 2\pi(\nu_0 + \gamma t) \frac{2nz_{R,i}}{c} + \theta(t) - \theta \left( t - \frac{2nz_{R,i}}{c} \right) \right], \quad (2-1)$$

where  $M$  is the number of scatterers in the fiber,  $a_{R,i}$  is the  $i$ th scatter amplitude,  $z_{R,i}$  is the position of the  $i$ th scatterer,  $\nu_0$  is the initial frequency of the probe light,  $\gamma$  is the frequency sweep rate,  $n$  is the effective refractive index of the fiber,  $c$  is the speed of light in a vacuum, and  $\theta(t)$  and  $\theta(t - 2nz_{R,i}/c)$  are the laser phase noises of the local and backscattered lights, respectively. Here, I define a one-dimensional scatter model [2-5], [2-8], in which discrete scatterers are distributed along the fiber as shown in Fig. 2-2. Since the beat frequency of  $I_R(t)$  is proportional to  $z_i$ , the complex amplitude of the scatter as a function of distance can be obtained by Fourier transforming  $I_R(t)$ . After the Fourier transform, a complex optical spectrum of the Rayleigh backscatter for a local segment of the fiber can be obtained by performing an inverse Fourier transform on windowed distance domain data (a segment of OTDR-like traces) [2-6], and it is used as a fiber signature in the conventional method. Since the optical frequency of the probe light is swept, the inverse Fourier transformed data can be translated to the optical frequency domain. If the segment size is much larger than the spatial resolution

## 2.2. Measurement principles

of C-OFDR, the complex scatter spectrum for the segment  $z_{R,a} < z_{R,i} < z_{R,b}$ ,  $\sigma_{ab}(t)$ , can be represented by

$$\sigma_{ab}(t) \cong \sum_{i=a}^b a_{R,i} \exp \left\{ j \left[ 2\pi(\nu_0 + \mathcal{N}) \frac{2nz_{R,i}}{c} + \theta(t) - \theta \left( t - \frac{2nz_{R,i}}{c} \right) \right] \right\}. \quad (2-2)$$

Here the complex scatter spectrum is written as a function of  $t$  since the probe light frequency is swept with respect to time. It is noteworthy that the difference between the phase noises of the local and backscattered light,  $\theta(t) - \theta(t - 2nz_{R,i}/c)$  depend on the scattering position. Thus the phase component of  $\sigma_{ab}(t)$  is perturbed randomly at every measurement if the scattering position is far beyond the laser coherence length. This leads directly to the degradation of the scatter signature repeatability. Therefore, the maximum measurable range with the conventional method is limited by the laser coherence length.



## 2. Rayleigh backscattering signature measured with C-OFDR

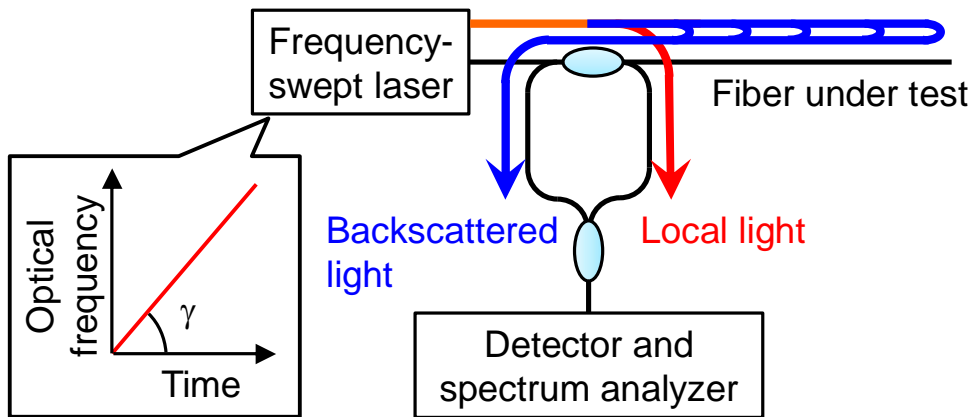


Figure 2-1. Basic setup of C-OFDR.

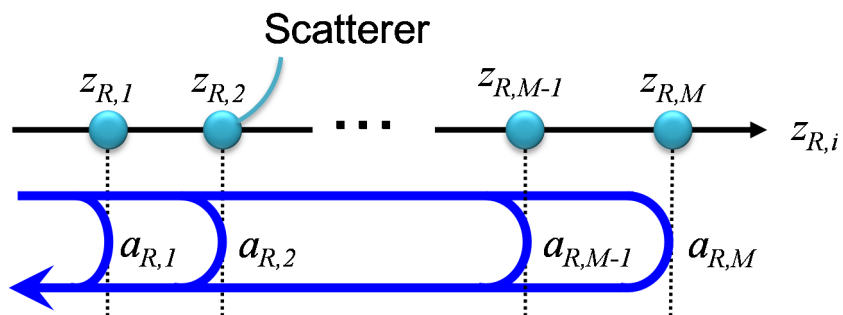


Figure 2-2. One-dimensional scatterer model.

## 2.2. Measurement principles

### 2.2.2 Scatter power spectrum in proposed method

To obtain the scatter signature with high repeatability for long distances beyond the laser coherence length, I introduce the square of the absolute value of the complex scatter spectrum, which we call the scatter power spectrum. The scatter power spectrum  $|\sigma_{ab}(t)|^2$  can be written as [2-11]

$$|\sigma_{ab}(t)|^2 = \sum_{i=a}^b a_{R,i}^2 + 2 \sum_{i=a}^b \sum_{j=i+1}^b a_{R,i} a_{R,j} \cos \left\{ 2\pi \left( \nu_0 + \mathcal{N} \left( \frac{2nz_{R,j}}{c} - \frac{2nz_{R,i}}{c} \right) - \left[ \theta \left( t - \frac{2nz_{R,j}}{c} \right) - \theta \left( t - \frac{2nz_{R,i}}{c} \right) \right] \right) \right\}, \quad (2-3)$$

where the first term shows the summation of the optical power of the scatters in  $z_{R,a} < z_{R,i} < z_{R,b}$ , and the second term stands for the interference between the backscattered lights from different scatterers in the segment. It is noteworthy that the phase noise of the local light is cancelled out in the second term, which indicates that the influence of the laser phase noise in  $|\sigma_{ab}(t)|^2$  does not depend on the scattering position, whereas the difference between the phase noises of the scatter remains in the segment,  $\theta(t - 2nz_{R,j}/c) - \theta(t - 2nz_{R,i}/c)$ . Therefore, the repeatability of the scatter power spectrum is not limited by the measurement range. In contrast, the segment size determines the influence of the laser phase noise. The scatter power spectrum is expected to be given precisely when the segment size is enough small compared with the laser coherence length. Although the scatter power spectrum does not contain the phase components of the Rayleigh backscatter, it can be handled by the signature for individual fibers as well as the complex spectrum because its waveform is randomly jagged due to random refractive index fluctuations in the fiber. The scatter power spectrum can be considered as a reflected power spectrum from a weak and random period grating, thus a spectral shift in the scatter power spectrum also occurs when the temperature or strain is changed as in the reflection spectrum of fiber Bragg gratings [2-12].

### 2.3. Experimental setup

Figure 2-3 shows our experimental setup. I prepared two lasers with different coherence lengths, namely Lasers 1 and 2, to investigate the influence of the laser phase noise. The coherence lengths of Lasers 1 and 2 were about 10 km and 500 m respectively, which were estimated in [2-13]. The optical frequencies were swept with a single side band (SSB) modulator [2-14], and the sweep range and rate were controlled by changing the modulation signal generated by an RF synthesizer. In this study, the sweep range was set at 2 GHz, which corresponds to the ideal spatial resolution of 5 cm if the laser phase noise is not taken into account. I changed only the sweep rate in the experiment. A 100-km long SMF was used as the FUT, and placed in a soundproof box to reduce acoustic noise. To investigate the temperature response, I placed a relevant fiber section in a temperature-controlled water bath whose temperature was accurate to 0.01°C. A polarization diversity scheme was employed in the interferometer to eliminate polarization-dependent effects due to such factors as birefringence. The Rayleigh backscatter of the P- and S-polarization states were individually detected by two balanced photodetectors, and acquired by a two-channel A/D converter. A Fourier-transform and an inverse Fourier-transform were performed on these two sets of polarization data individually, and a vector sum was calculated to generate a polarization-independent spectrum. The repeatability of the scatter signature was evaluated by calculating the cross-correlation between the two sets of measurement results.

### 2.3. Experimental setup

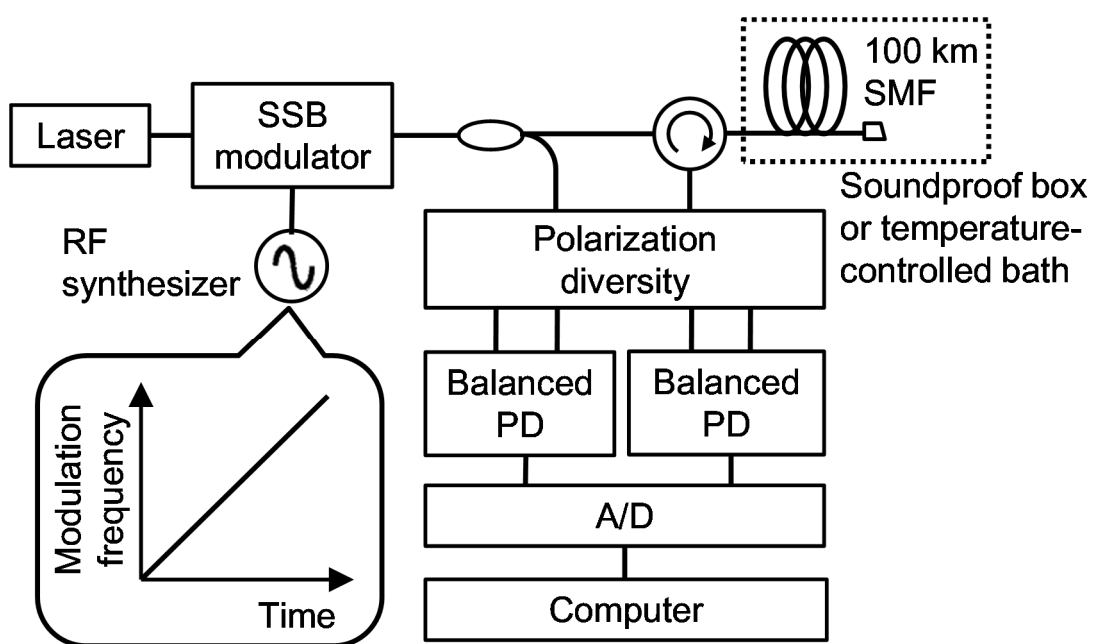


Figure 2-3. Experimental setup of C-OFDR.

## 2.4. Experimental results and discussion

### 2.4.1. Rayleigh scatter signatures beyond laser coherence length

Figure 2-4 (a) and (b) show the cross-correlation of the complex scatter spectrum and the scatter power spectrum at each segment position of the FUT. The optical frequency sweep rate and the segment size were 100 GHz/s and 100 m, respectively. The time interval of the measurements was 0.1 sec during which the fiber conditions were expected to remain stable. The complex scatter spectrum was not maintained at positions beyond the coherence length. On the other hand, the scatter power spectrum was identified over a long range. The repeatability degradation of the scatter power spectrum in the region beyond 70 km seemed to be affected by the detector noise whose power relative to the signal was increased by the attenuation of the FUT.

Figure 2-5 (a) and (b) show the scatter power spectra and cross-correlation measured at temperatures of 35.00 and 35.02 °C, respectively. I changed the temperature of a fiber section at around 40 km, and carried out the measurement with Laser 1. The scatter power spectrum was shifted after the temperature change, resulting in a correlation peak shift. Figure 2-6 shows the temperature dependence of the spectral shift of the scatter power spectrum. Applying a linear least squares fit to the plot, I estimated the sensitivity of the scatter power spectrum to the temperature change at  $-1.28 \text{ GHz}/^\circ\text{C}$ , which is similar to the result obtained with the conventional method [2-6].

## 2.4. Experimental results and discussion

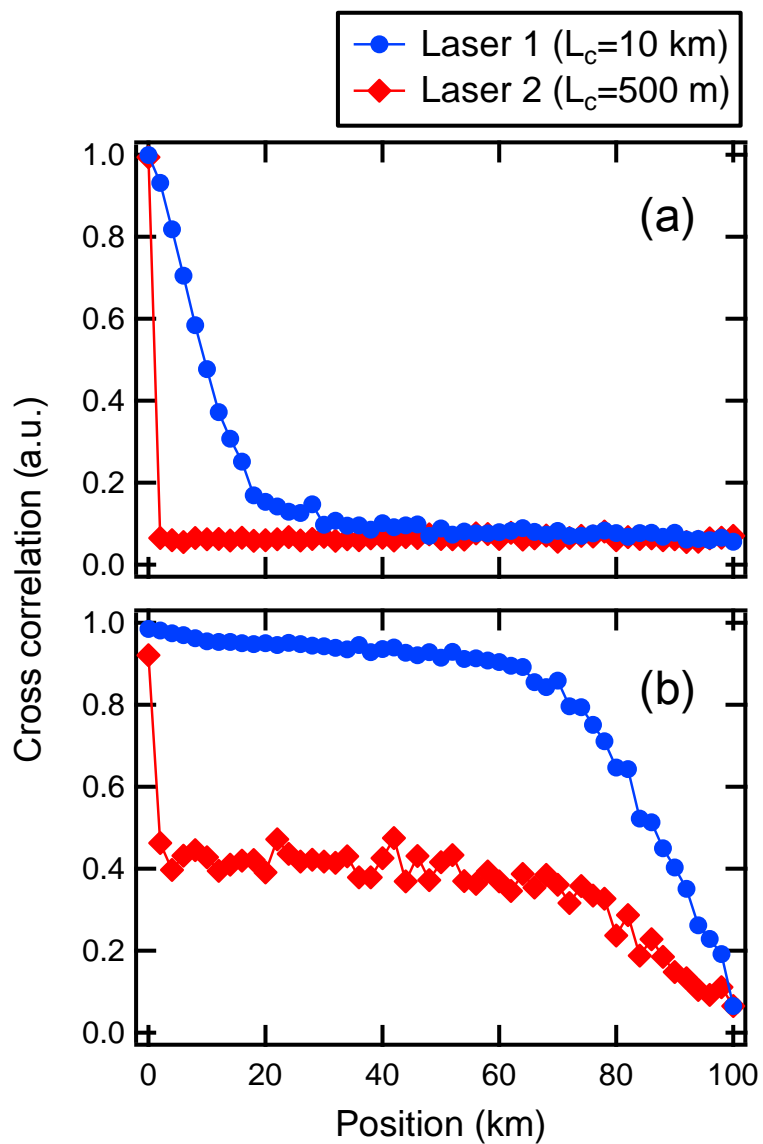


Figure 2-4. Cross-correlations of (a) complex scatter spectrum, (b) scatter power spectrum at each segment position. The segment size was 100 m.

## 2. Rayleigh backscattering signature measured with C-OFDR

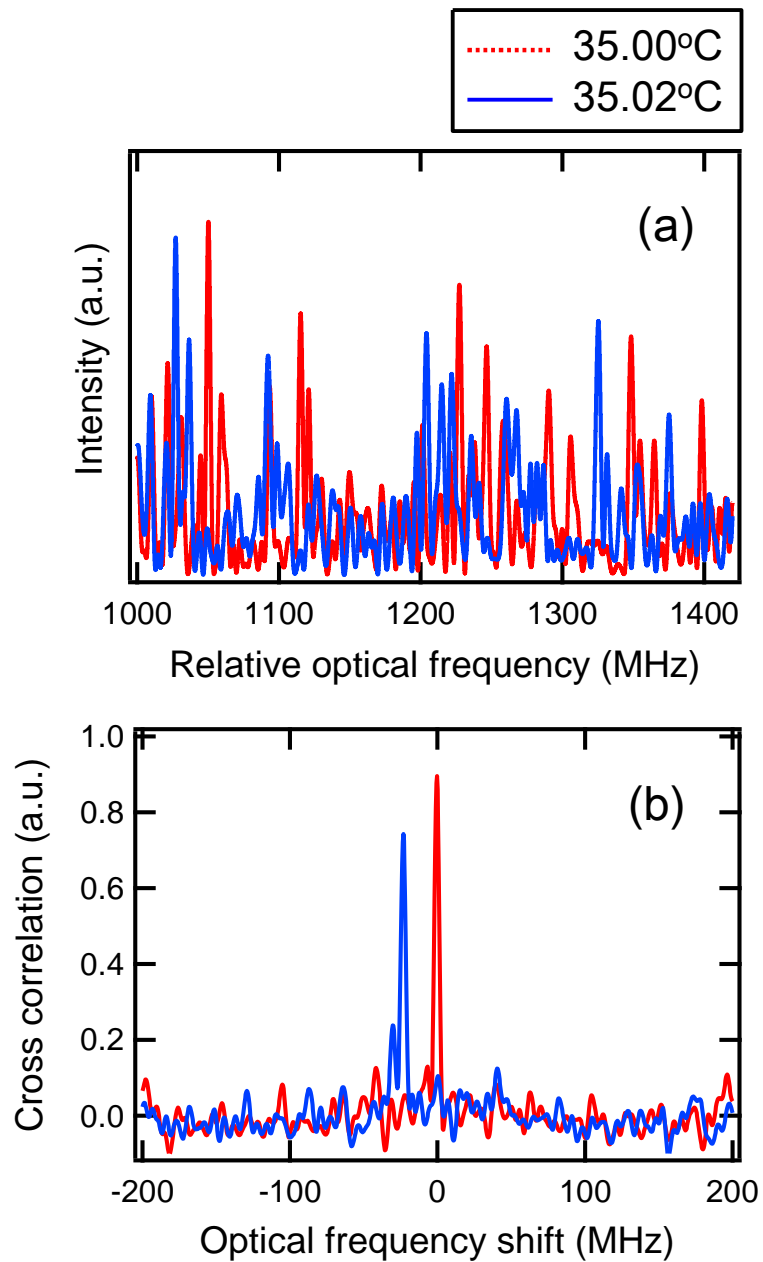


Figure 2-5. (a) Scatter power spectra, (b) cross-correlation of the scatter power spectra at 40 km measured at 35.00 and 35.02 °C. In the cross-correlation, the spectrum at 35.00°C was used as reference data. The segment size was 25 m. Laser 1 with  $L_c = 10$  km was used.

## 2.4. Experimental results and discussion

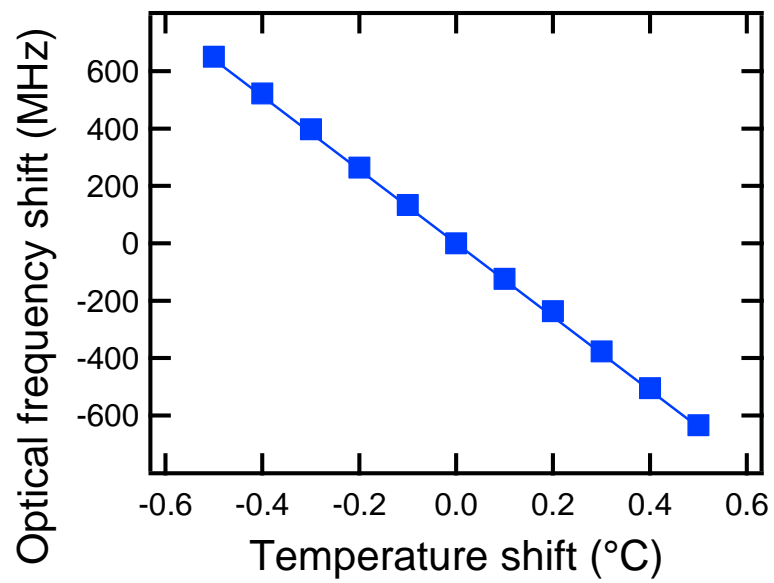


Figure 2-6. Temperature dependence of spectral shift of the scatter power spectrum measured at 40 km. The solid line is a linear least square fit. The segment size was 25 m.



### 2.4.2. Segment size and frequency sweep rate dependence

Figure 2-7 shows the segment size dependence of the repeatability of the scatter power spectrum at 20 km. The correlation decreased due to the phase noise difference among the scatters in the segment when the segment size was longer than the coherence length, as mentioned in Section 2.2. On the other hand, I found that the repeatability of the scatter power spectrum was also decreased when the segment size was small. This is due to the broadening of the spatial resolution of the C-OFDR measurement. If the beat frequency of C-OFDR corresponding to segment position is randomly fluctuated for each measurement, the scatter power spectra will become less correlated. At the scattering position  $z$ , which is at a distance greater than the coherence length  $L_c$ , the power spectrum of the beat signal of C-OFDR can be given by a Lorentz function whose spectral width  $\Delta f_b$  is twice the laser linewidth  $\Delta f$  [2-10]. In that case, the broadened spatial resolution  $\Delta z_{max}$  can be estimated with

$$\Delta z_{max} = \frac{c}{2n\gamma} \Delta f_b = \frac{c}{2n\gamma} 2\Delta f = \frac{c^2}{\pi n \gamma L_c}, \quad (2-4)$$

where we assume  $z=(c/2n\gamma)f_b$  for the relationship between the beat frequency  $f_b$  and  $z$ ,  $\Delta f=c/\pi L_c$  for the relationship between the laser linewidth and the coherence length  $L_c$ . Equation 2-4 indicates that the influence of the spatial resolution broadening can be suppressed by increasing the frequency sweep rate of the probe light.

Figure 2-8 shows the sweep rate dependence of the cross-correlation of the scatter power spectrum measured with Laser 2. As the sweep rate increased, the scatter power spectra for a small segment size become more correlated. Since the segment size indicates the spatial resolution for identification or sensing, the use of a higher sweep rate is an effective way to achieve applications that require high resolution. The spatial resolution could be further improved by combining a technique that compensates for

## 2.4. Experimental results and discussion

beat frequency fluctuations such as a resampling method based on concatenated phase signals for the region beyond the coherence length as our group has reported in [2-15], [2-16].

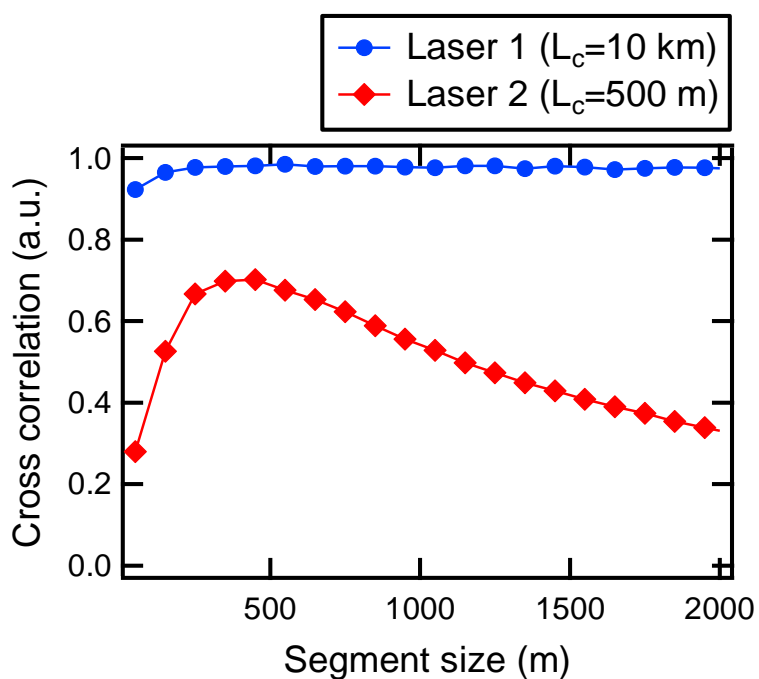


Figure 2-7. Segment size dependence of the cross-correlation of the scatter power spectrum at 20 km.

## 2. Rayleigh backscattering signature measured with C-OFDR

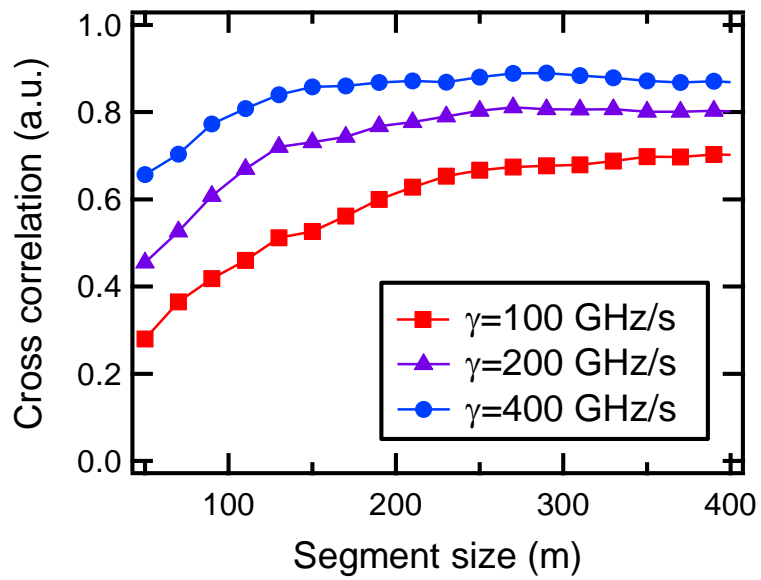


Figure 2-8. Frequency sweep rate dependence of the cross-correlation of the scatter power spectrum at 20 km.

## 2.4. Experimental results and discussion

### 2.4.3. Signal averaging for enhanced measurable range

With a complex scatter spectrum, the laser phase noise perturbs the scatter interference pattern itself when the position is at a distance greater than the coherence length. Signal averaging the complex scatter spectrum is thus not effective for long-range measurement. In contrast, for the scatter power spectrum in the proposed method, the influence of the laser phase noise is suppressed and does not depend on the scattering position. The measurable range can thus be further improved by employing signal averaging to reduce the detector noise such as thermal noise or shot noise.

Figure 2-9 shows the cross-correlation of the scatter power spectrum after signal averaging. I used a frequency sweep rate of 400 GHz/s, a time interval of 0.1 s, and a segment size of 50 m. The repeatability of the scatter power spectrum for long distances was improved by signal averaging regardless of laser type. I also found that the repeatability for Laser 2 significantly increased by signal averaging at around 50 km. For Laser 2, it is expected that an uncertainty of the scatter power spectrum due to the fluctuation of the segment position by the spatial resolution broadening of C-OFDR is reduced to a certain level by signal averaging. To prove this assumption, I observed the average scatter power spectra and Fresnel reflection peaks using a 50-km long SMF and Laser 2, where I used a segment size of 50 m and an averaging number of 10. Figure 2-10 shows the repeatability of the averaged scatter power spectra when the relative segment positions were changed. Figure 11 shows the observed Fresnel reflection intensity. The 3dB spatial resolutions of C-OFDR at 50 km were 80, 40, and 20 m for sweep rates of 100, 200 and 400 GHz/s, respectively, as shown in Fig. 2-11. These results agreed with the broadening of the correlated relative positions compared with the used segment size of 50 m shown in Fig. 2-10. Therefore, an effective segment size after signal averaging that contributes to cross-correlation becomes large

## 2. Rayleigh backscattering signature measured with C-OFDR

due to the spatial resolution broadening of C-OFDR, which results in increased repeatability for the measurement with Laser 2. In other words, the effective spatial resolution for signature applications is degraded, which should be taken into account particularly when the segment size is insufficiently large with the actual spatial resolution of C-OFDR.

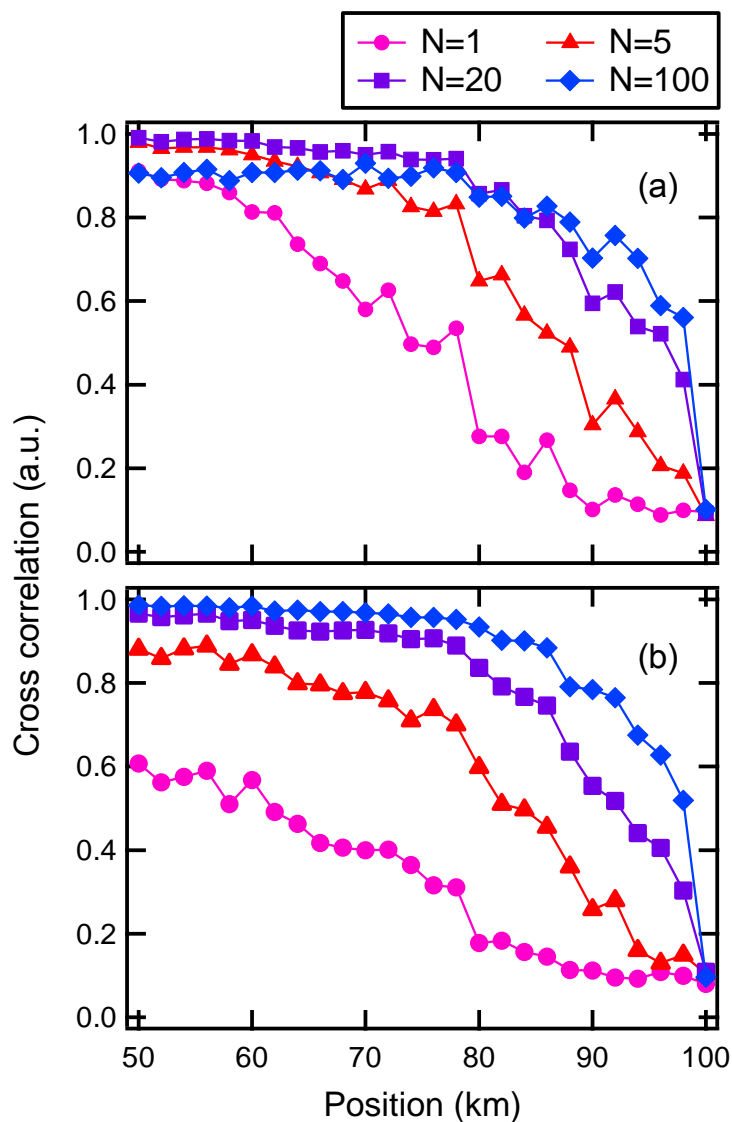


Figure 2-9. Averaging number dependence of the cross-correlation of the averaged scatter spectra measured with (a) Laser 1, (b) Laser 2.

## 2.4. Experimental results and discussion

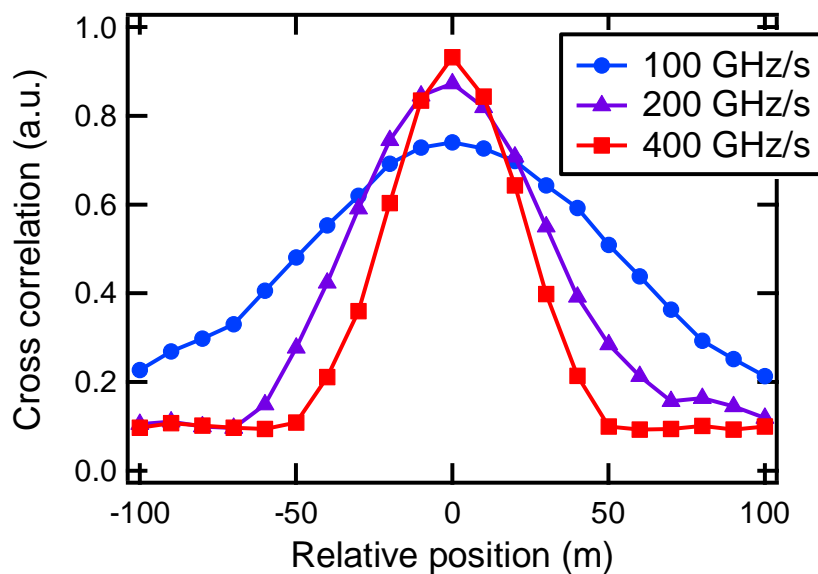


Figure 2-10. Dependence of cross-correlation of averaged scatter spectra on segment position difference.

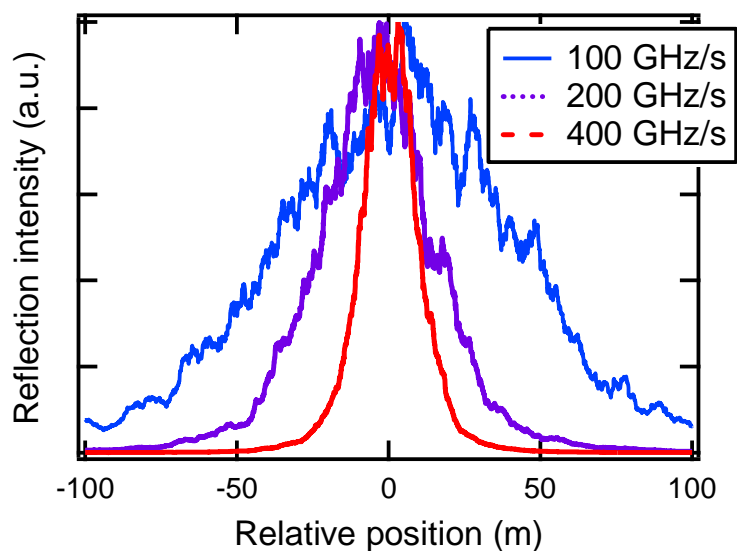


Figure 2-11. Fresnel reflection at the end of a 50-km long SMF.

### *2.4.4. Demonstration of long-range distributed measurement of spectral shift*

In this subsection, I report the demonstration of distributed, highly-sensitive measurement of Rayleigh backscattering spectral shift caused by temperature change beyond the laser coherence length. Figure 2-12 shows the configuration of the sensing fiber we used. I prepared three fiber sections at the end of a 100-km long SMF, and placed each section in different temperature-controlled water baths. I set stable temperatures for Sections A and C, and carried out the C-OFDR measurements while changing the temperature of Section B. Laser 1 was used as a light source, and the frequency sweep rate was 400 GHz/s. The averaging number and measurement interval were 200 and 0.1 sec, respectively. The segment size was set at 25 m, which was much larger than the spatial resolution of 2 m obtained from the Fresnel reflection observed at the end of the FUT.

Figure 2-13 shows the spectral shift of the averaged scatter spectrum along the FUT at each temperature. Linear spectral shifts caused by temperature changes were observed in Section B. The temperature sensitivity in this demonstration was estimated to be 0.003 °C by converting the full-width at half-maximum of the correlation peaks to the temperature. The measurable temperature range was estimated to be 1.4 °C, which would be expanded by using tunable laser sources with a wide frequency sweep range for a C-OFDR system.

## 2.4. Experimental results and discussion

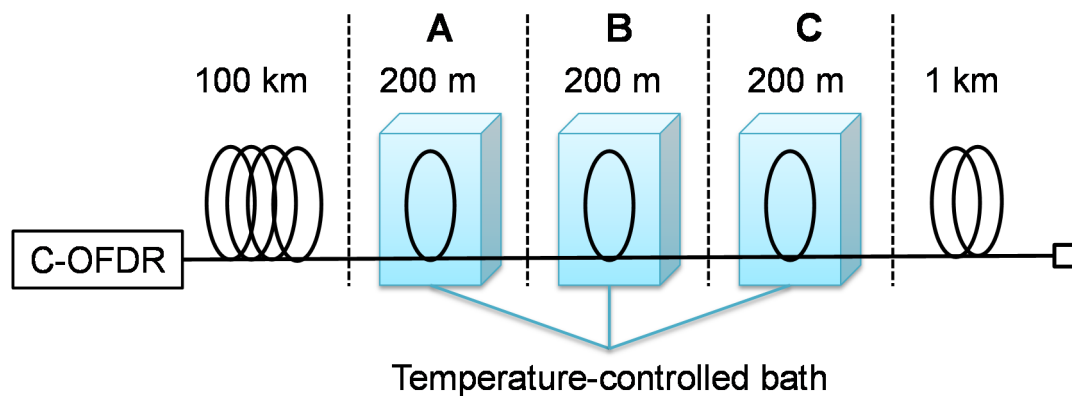


Figure 2-12. Configuration of sensing fiber.

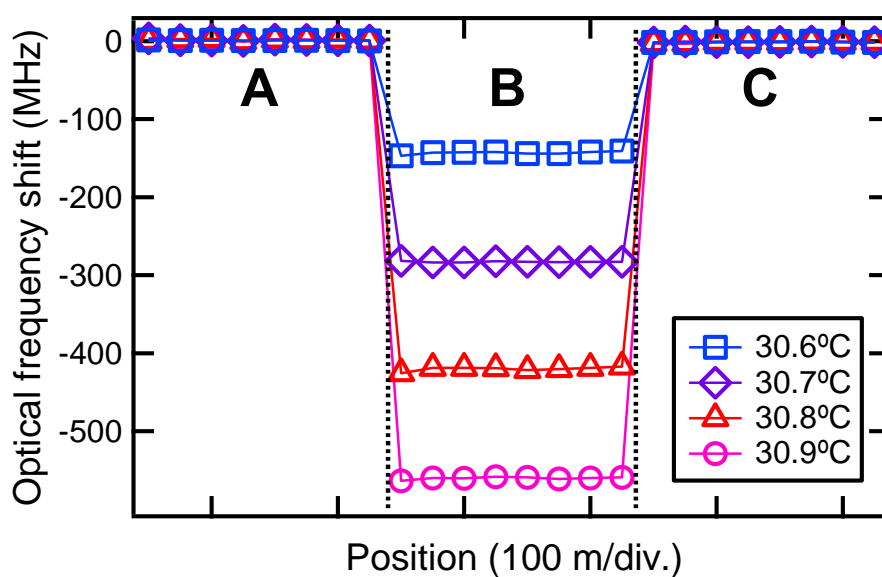


Figure 2-13. Spectral shift distribution of averaged scatter spectrum at each temperature in Section B. The spectrum at 30.5°C was used as reference data in the cross-correlation.



## **2.5. Conclusion**

I proposed a technique for the long-range C-OFDR measurement of a Rayleigh scatter signature beyond the laser coherence length by analyzing the optical power spectrum of the scatter in a local fiber segment. I confirmed experimentally that the influence of the laser phase noise did not depend on the measurement range and could be controlled by changing the signature size and the frequency sweep rate of the C-OFDR used in the proposed method. Moreover, signal averaging in proposed method was effective in reducing the detector noise resulting in further improvement of the measurable range. I also demonstrated distributed measurement of the spectral shift of scatter signature with a measurement range of 100 km, a spatial resolution of less than 30 m, a measurable temperature range of 1.4 °C, and a temperature sensitivity of 0.003 °C. I believe that our proposed method can extend the scalability of scatter signature applications to a long range.

## **3. Distributed measurement of differential mode delay along few-mode fiber**

### **3.1. Introduction**

MDM transmission using FMF and MIMO processing has been attracting considerable attention as a technique for realizing a large transmission capacity exceeding that of current SMF based transmission line [3-1]. DMD, which is defined as a relative group delay within the propagation modes, is an important parameter for designing and/or characterizing the MDM system, because MIMO processing becomes more complicated as the DMD increases. In recent studies, the DMD has been measured using various techniques including a time-domain method [3-2], a frequency-domain method [3-3], and a low-coherence interferometric method [3-4], which provide the total link DMD of an MDM system. The link DMD could be affected by the structural imperfections of FMFs or mode couplings at splice points [3-5], however, neither the accumulated DMD along an FMF link nor its measurement method has been well studied. High-resolution optical reflectometry could be one way to evaluate the accumulated DMD by measuring the Fresnel reflection as reported in [3-3]. However, such an event does not always occur at the position to be characterized. If we can measure the DMD at arbitrary positions along the FMF link nondestructively, it would help us to analyze and design the MDM systems.

In this chapter, I first propose a novel concept for characterizing the accumulation of the DMD in the FMF link. With the proposed method, the accumulated link DMD can be nondestructively characterized by measuring the delay between randomly distributed Rayleigh backscattering spectral shifts with different modes, which are

### *3. Distributed measurement of differential mode delay along few-mode fiber*

caused by slight natural environmental disturbances. I employ a coherent optical frequency domain reflectometry (C-OFDR) to achieve a highly accurate DMD measurement for fiber sections with length of several tens of meters. I experimentally confirm the feasibility of the proposed method with different kinds of two-LP mode fiber (TMF) links.

This chapter is organized as follows. Section 3.2 describes the principle of DMD distribution measurement using our proposed method. Section 3.3 reports the experimental setup we used. Section 3.4 contains our experimental results and discussion, and Section 3.5 provides the conclusion.

### 3.2. Measurement principle

The concept of our proposed method is illustrated in Fig. 3-1. This method utilizes Rayleigh backscattering spectra with different modes that are sensitively and synchronously shifted with respect to local environmental disturbances such as temperature or strain as describe in chapter 2 and Ref. [3-6]. In the reflectometry results, the spectral shifts will appear at different delay times between modes. The spectral shifts are thus correlated between modes with delay times that correspond to the accumulated link DMD since the position at which the environmental disturbance occurs is exactly the same for each mode.

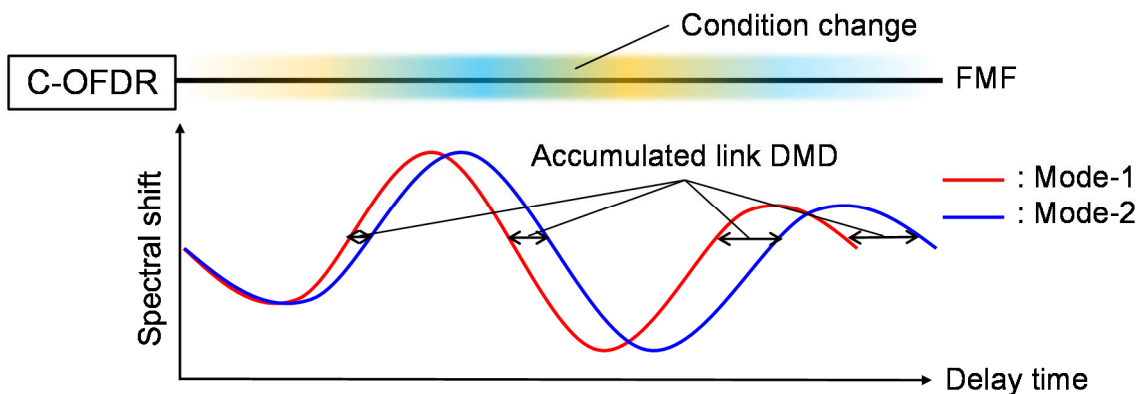


Figure 3-1. Concept of proposed method.

C-OFDR is an attractive way to support this concept because the spectral shifts of a short fiber section can be easily obtained by digital signal processing, which results in a highly accurate characterization of the link DMD. The spectral shifts can be measured by comparing Rayleigh backscattering spectra, which are calculated by windowing a relevant segment to the Fourier-transformed data of the beat signal, and performing an inverse Fourier transform [3-6]. The window size determines the accuracy of the spectral shift with respect to the environmental disturbances. For

### *3. Distributed measurement of differential mode delay along few-mode fiber*

example, a window size of several ns (several centimeters) corresponds to a spectral accuracy of hundreds of MHz, which provides a temperature accuracy of better than 1°C for silica-based fibers. The difference between the spectral shifts to the environmental disturbances for different modes can be ignored since it would be much smaller than the spectral accuracy of the measurement.

### **3.3. Experimental setup**

Figure 3-2 shows our experimental setup. The laser source was a continuously tunable laser diode whose wavelength sweep rate was 100 nm/s. I swept 4 nm, which corresponds to a delay time resolution of 2.15 ps, and a spatial resolution of 223  $\mu\text{m}$ . The setup included two interferometers namely an auxiliary interferometer to compensate for the sweep nonlinearity [3-7], and a main interferometer to detect the Rayleigh backscattering. The probe light was excited into the FUT with the  $\text{LP}_{01}$  mode, and the backscattering generated with the  $\text{LP}_{01}$  and  $\text{LP}_{11}$  modes was separated with a PLC-based mode demultiplexer (DEMUX) [3-8]. The backscattering with different modes was coherently and individually detected in two polarization diversity receivers. Band-pass filters (BPFs) were used to eliminate the high-frequency noise and the Fresnel reflection at the mode DEMUX. I calculated the scattering spectra with a 2.15-ns-wide width temporal window, which corresponded to a 22-cm fiber section. A Fourier transform and an inverse Fourier transform were performed on the beat signals individually, and the vector sum of the two polarization data was calculated to generate a polarization-independent spectrum in each mode. Then, the phase components of the scattering spectra were cancelled out, resulting to high repeatability measurements as described in chapter 2 and Ref. [3-9]. The configurations of the FUTs we used are shown in Fig. 3. I prepared two kinds of FUT, namely FUT-3.1 and 3.2, which consisted of step-index (SI) and graded-index (GI) TMFs whose DMDs per unit length were 2.2 and 0.07 ps/m, respectively. Thus the link DMD was expected to accumulate along each FUT as shown in Fig. 3. The fiber ends of both FUTs were bent to reduce the Fresnel reflection. Both FUTs were unspooled and loosely placed in an uncontrolled environment at around room temperature. With each FUT, I measured the

### 3. Distributed measurement of differential mode delay along few-mode fiber

scatter spectra twice with an interval of 15 minutes, and obtained the spectral shift by calculating the cross-correlation of the two data sets.

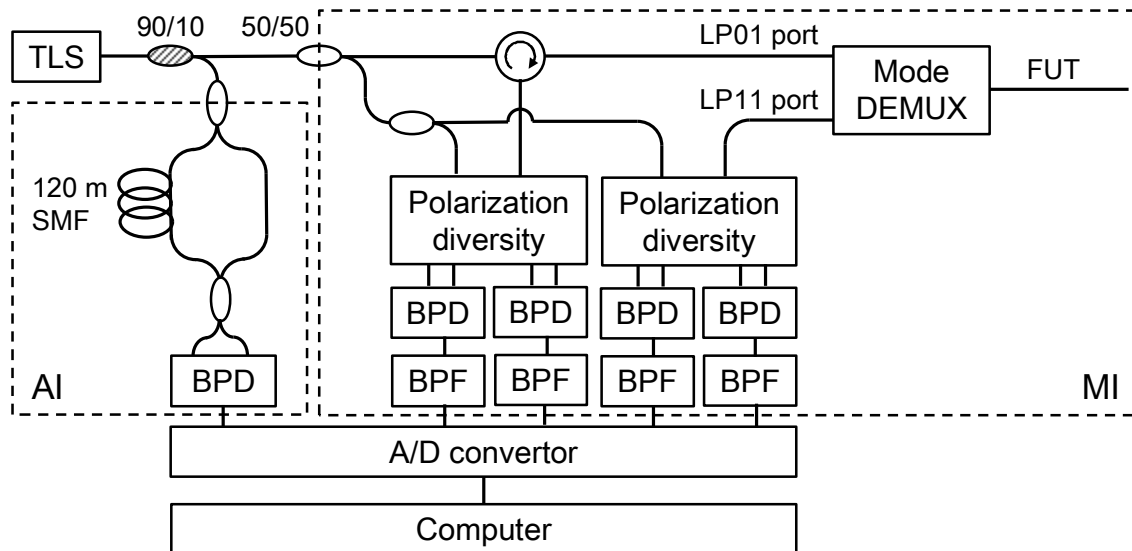


Figure 3-2. Experimental C-OFDR setup. TLS: tunable laser source, BPD: balanced photodetector, AI: auxiliary interferometer, MI: main interferometer.

### 3.3. Experimental setup

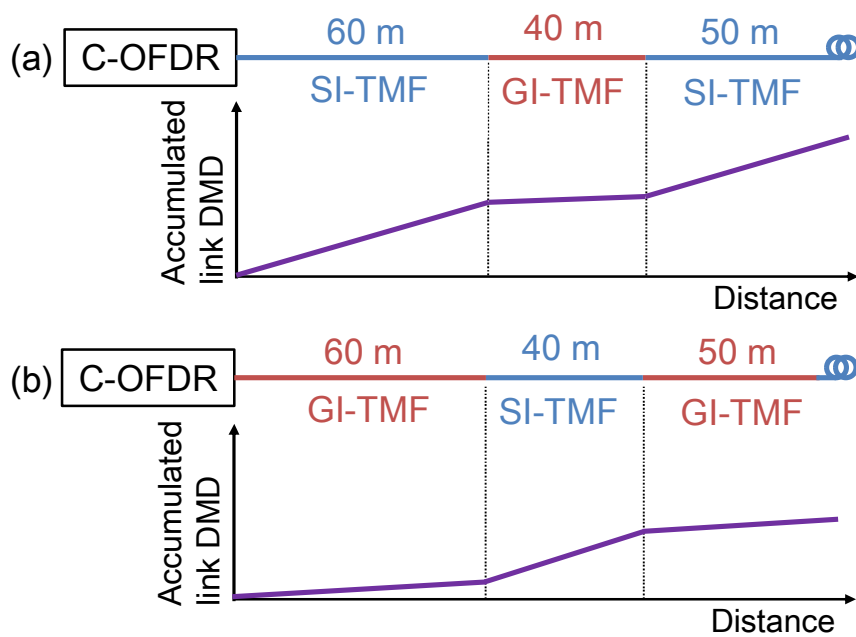


Figure 3-3. Configurations of FUTs and their accumulated link DMDs. (a) FUT-3.1, (b) FUT-3.2.



### 3.4. Experimental results

Figure 3-4 shows the distributed spectral shifts along FUT-3.1 and 3.2 measured in the  $LP_{01}$  and  $LP_{11}$  modes. In Fig. 3-4, the spectral shifts calculated for every 1000 points (2.15 ns) are plotted with a 1 point (2.15 ps) shift, and smoothed by averaging with the temporal window size. It can be seen that the spectral shift varied along the FUTs because of local environmental disturbances. The periodic nature of the spectral shifts is due to the round-trip configuration of the FUTs. Figures 3-4 (b) and (d) show the spectral shifts around 120-m position of the FUTs. The traces between the  $LP_{01}$  and  $LP_{11}$  modes are shifted with respect to the horizontal axes due to the accumulated DMD.

Figure 3-5 shows the accumulated link DMDs obtained from Fig. 3-4. The red squares show the accumulated link DMDs analyzed by calculating the cross-correlations of the data sets of the spectral shifts for every 386-ns width (40-m fiber section) between the  $LP_{01}$  and  $LP_{11}$  modes. Thus the red square indicates the mean amount of accumulated link DMD in the 40-m fiber section, in other words, the spatial resolution of the accumulated DMD was 40 m. The blue squares also show the results measured with the method described in [3-3], where Fresnel reflections caused by cutting the FUT at each position were measured for both modes. The solid lines are the calculations with the DMDs per unit length of the TMFs we used. A clear difference was observed between the DMDs in SI and GI, and the accumulated link DMD was in good agreement with the results obtained from the Fresnel reflections and calculations. The measurement error was within about 20 ps, which indicates that the low spectral accuracy of the measurement caused an error in the cross-correlation of the spectral shifts. I expect that the DMD accuracy could be improved with a larger window size, which would provide a highly sensitive measurement of spectral shifts as

### *3.4. Experimental results*

reported in [3-5]. With the proposed method, the window size should be as large as possible in the range of the corresponding fiber section where the environmental disturbance is considered to be sufficiently uniform for us to obtain the spectral shifts clearly.

### 3. Distributed measurement of differential mode delay along few-mode fiber

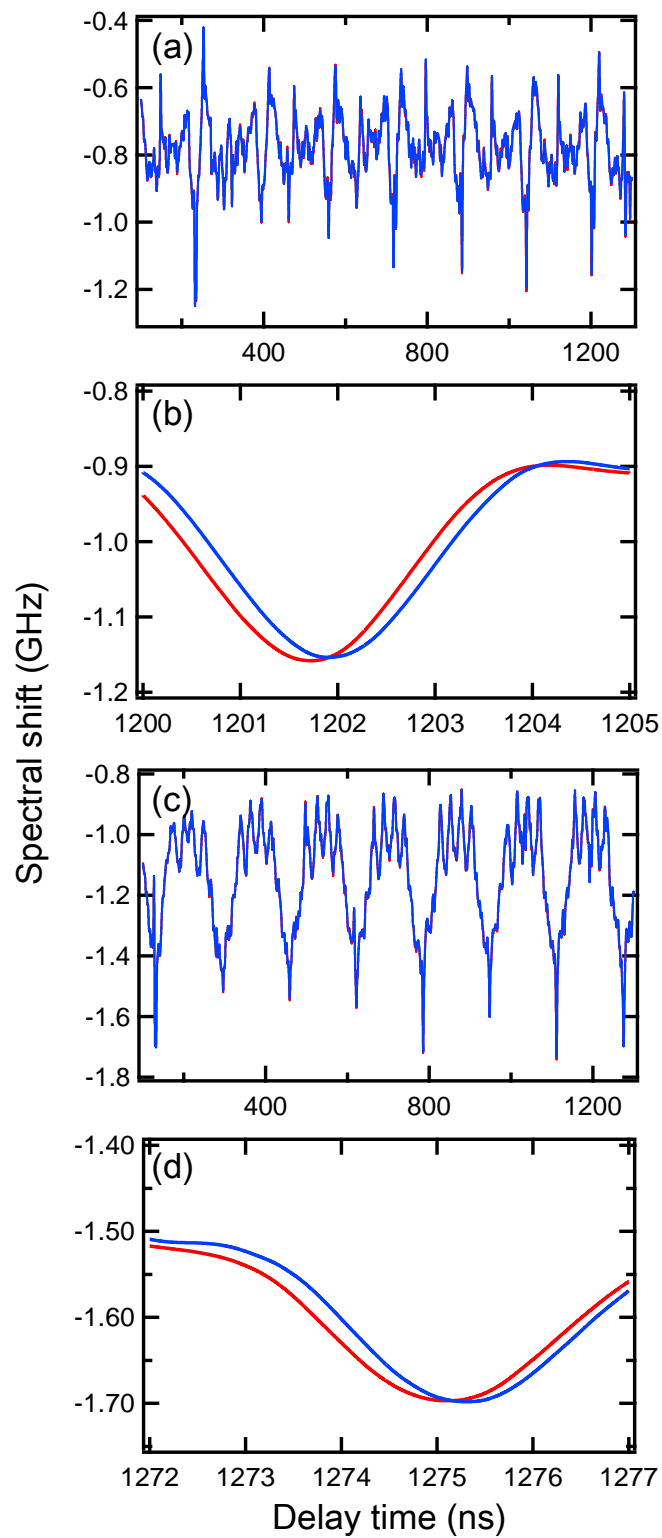


Figure 3-4. Spectral shift distribution of the scatter measured with (a), (b) FUT-3.1, (c), (d) FUT-3.2.

### 3.4. Experimental results

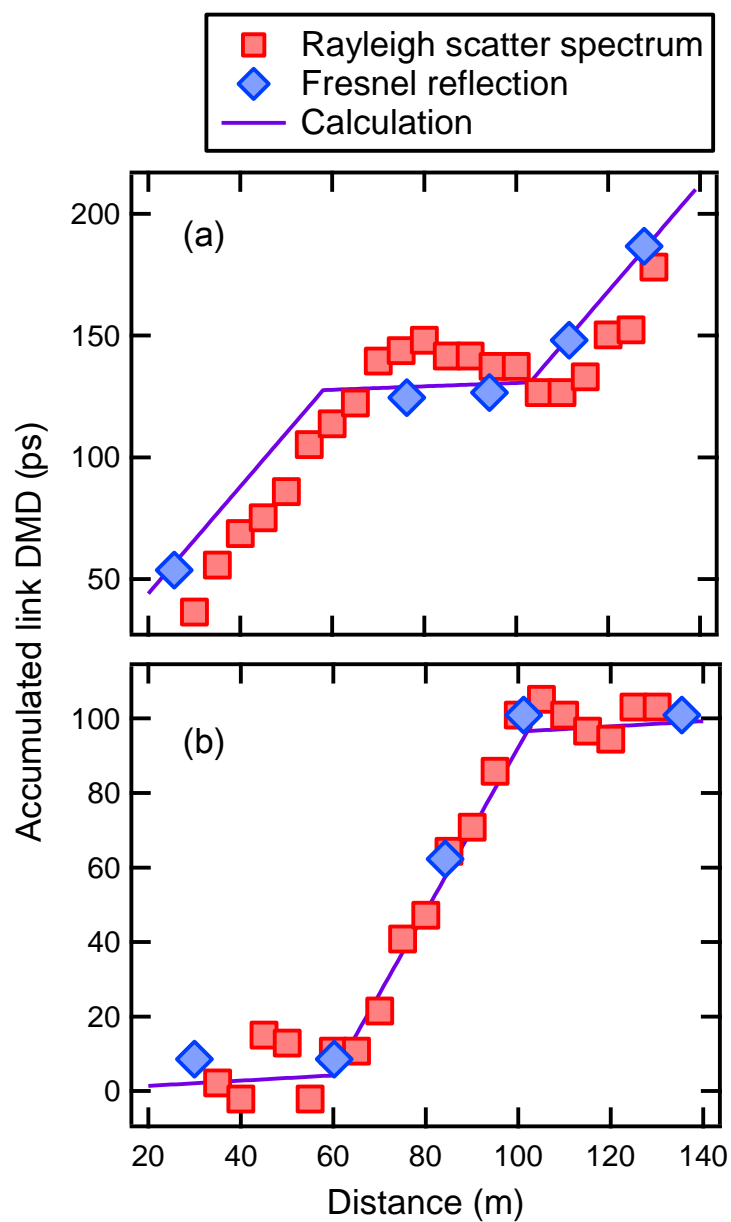


Figure 3-5. Accumulated link DMDs along (a) FUT-3.1, (b) FUT-3.2.

### **3.5. Conclusion**

I proposed the nondestructive characterization of the accumulated link DMD along an FMF by using the spectral shifts of Rayleigh backscattering measured with C-OFDR. The proposed method was experimentally confirmed with different kinds of TMF links where SI- and GI-TMFs were concatenated, and the each fiber section could be identified from the difference of DMD accumulation along the fiber by using the proposed method. The results agreed well with that of the destructive method and the estimations from the fiber parameters.

## 4. Distributed measurement of spatial mode dispersion along coupled multicore fiber

### 4.1. Introduction

Coupled MCF, which is designed with a lower core pitch compared with the non-coupled MCF, has been recently attracting considerable attention with its potential for realizing SDM transmission with high spatial channel density. One interesting property of coupled MCF is its Gaussian-like impulse response whose width increases in proportion to the square root of the propagation distance  $L$  as a result of the strong random mode coupling along the fiber, when the core pitch is adequately designed. This property is helpful for reducing the complexity of MIMO processing especially in long-haul transmissions, and a transmission distance exceeding a thousand kilometers has been achieved by using such strongly coupled MCF (SC-MCF) with 6 spatial channels [4-1].

For the purpose of characterizing SC-MCF, SMD has been defined and measured in a similar manner to polarization mode dispersion (PMD) [4-2], [4-3]. It has been reported that SMD is sensitively affected by fiber bending and twisting [4-2], [4-4] and so can be expected to change locally in a transmission line due to the external stress caused by cabling, cable installation and environmental changes after installation. However, the distribution of SMD along an SC-MCF has only been measured by cutting the fiber at arbitrary positions. If we can measure the SMD distribution non-destructively, it would help us to characterize SC-MCFs in many scenarios such as when identifying portions of transmission lines that affect the end-to-end characteristic, which is essential for system design.

#### *4. Distributed measurement of spatial mode dispersion along coupled multicore fiber*

In this chapter, I propose a non-destructive method for measuring the SMD distribution along an SC-MCF. The SMD distribution can be measured with the proposed method using the random interference pattern of the Rayleigh backscattering amplitudes obtained with coherent optical frequency domain reflectometry (C-OFDR). I experimentally confirm the feasibility of the proposed method with two kinds of SC-MCFs by observing their SMDs, which increase in proportion to  $\zeta L$ .

This chapter is organized as follows. Section 4.2 describes the principle of SMD distribution measurement using our proposed method. Section 4.3 reports the experimental setup we used. Section 4.4 contains our experimental results and discussion, and Section 4.5 provides the conclusion.

## 4.2. Measurement principles

### 4.2.1. Basic principle of SMD distribution measurement

Figure 4-1 shows a schematic diagram of SMD measurement with our proposed method. The Rayleigh backscattering amplitudes obtained with a coherent optical reflectometry technique is utilized to measure the SMD in arbitrary portions. With coherent optical reflectometry, the backscattering amplitudes have a randomly jagged appearance, which results from interference between multiple backscattered lights which meet in a spatially resolved portion of a fiber [4-5]-[4-7]. When the reflectometry is performed with an SC-MCF, the backscattered lights propagate from an arbitrary portion of the fiber to the launched fiber end with super-modes, which randomly couple with each other. Since the super-modes in the SC-MCF are associated with multiple paths with different delays and randomly coupling, the backscattering amplitude observed with the reflectometry can be considered superposed results of the delayed replicas of the backscattering interference pattern. Consequently, the accumulated SMD can be characterized with the auto-correlation of the observed backscattering amplitudes of an arbitrary portion of the fiber. Assuming that the backscattering replicas have a Gaussian distribution with a standard deviation of  $\sigma_s$ , the measured backscattering amplitude at the position of delay  $\tau$  can be described as

$$\tilde{\varepsilon}(\tau) = \sum_m e^{-\frac{(\Delta\tau_m)^2}{2\sigma_s^2}} e^{j\Delta\theta(\Delta\tau_m)} \varepsilon(\tau - \Delta\tau_m), \quad (4-1)$$

where  $\tilde{\varepsilon}(\tau)$  and  $\varepsilon(\tau)$  are the complex backscattering amplitudes with/without mode coupling, and  $\Delta\tau_m$  and  $\Delta\theta(\Delta\tau_m)$  are the relative delay and random phase component of the  $m$ th backscattering replica generated by mode coupling, respectively. Since the SMD  $\Delta\tau$  is defined as twice the standard deviation of the impulse response (optical intensity) [4-2], [4-3], Eq. (4-1) can be rewritten as



#### 4. Distributed measurement of spatial mode dispersion along coupled multicore fiber

$$\tilde{\varepsilon}(\tau) = \sum_m e^{-\frac{(\Delta\tau_m)^2}{(\Delta\tau)^2}} e^{j\Delta\theta(\Delta\tau_m)} \varepsilon(\tau - \Delta\tau_m). \quad (4-2)$$

As implied in Eq. (4-2), the probability distribution of the backscattering replica is determined by  $\Delta\tau$ . An auto-correlation of  $\tilde{\varepsilon}(\tau)$ ,  $R(\tau')$ , is performed to analyze the probability distribution as (see Appendix B.)

$$\begin{aligned} R(\tau') &= \int \tilde{\varepsilon}(\tau) \tilde{\varepsilon}(\tau + \tau') d\tau \\ &\propto \delta_{\tau',0} C(0) + e^{-\frac{\tau'^2}{2(\Delta\tau)^2}} C(\tau'), \end{aligned} \quad (4-3)$$

with

$$C(\tau') \equiv \sum_m e^{-\frac{2(\Delta\tau_m + \tau'/2)^2}{(\Delta\tau)^2}} e^{j[\Delta\theta(\Delta\tau_m) - \Delta\theta(\Delta\tau_m + \tau')]}, \quad (4-4)$$

where  $\delta_{\tau',0}$  is the Kronecker delta, and  $*$  denotes the complex conjugate. Since  $\varepsilon(\tau)$  randomly fluctuates along the delay time due to the interference between backscattered lights, we assume the correlation of  $\varepsilon(\tau)$  with itself in Eq. (3) as

$$\int \varepsilon(\tau) \varepsilon^*(\tau + \tau') d\tau \propto \delta_{\tau',0}, \quad (4-5)$$

The first term of Eq. (4-3) represents a correlation of  $\tilde{\varepsilon}(\tau)$  with itself, and the second term accounts for the correlation between backscattering replicas whose delay times differ. An example of  $|R(\tau')|$  is shown on the right in Fig. 4-1. In addition to the central peak, small peaks are distributed around the center, where the square root of the second moment of  $|R(\tau')|$  except for the central peak reflects the SMD. Therefore, the SMD distribution can be measured by performing an auto-correlation analysis of the backscattering amplitude in arbitrary sections [4-9]. It should be noted that the number of data points for the correlated backscattering section is related to the correlation

## 4.2. Measurement principles

noise, which comes from the imperfect randomness of the waveform used for the correlation. Many data points are required for the correlation to suppress measurement error. However, that leads to spatial accuracy degradation in the SMD distribution.

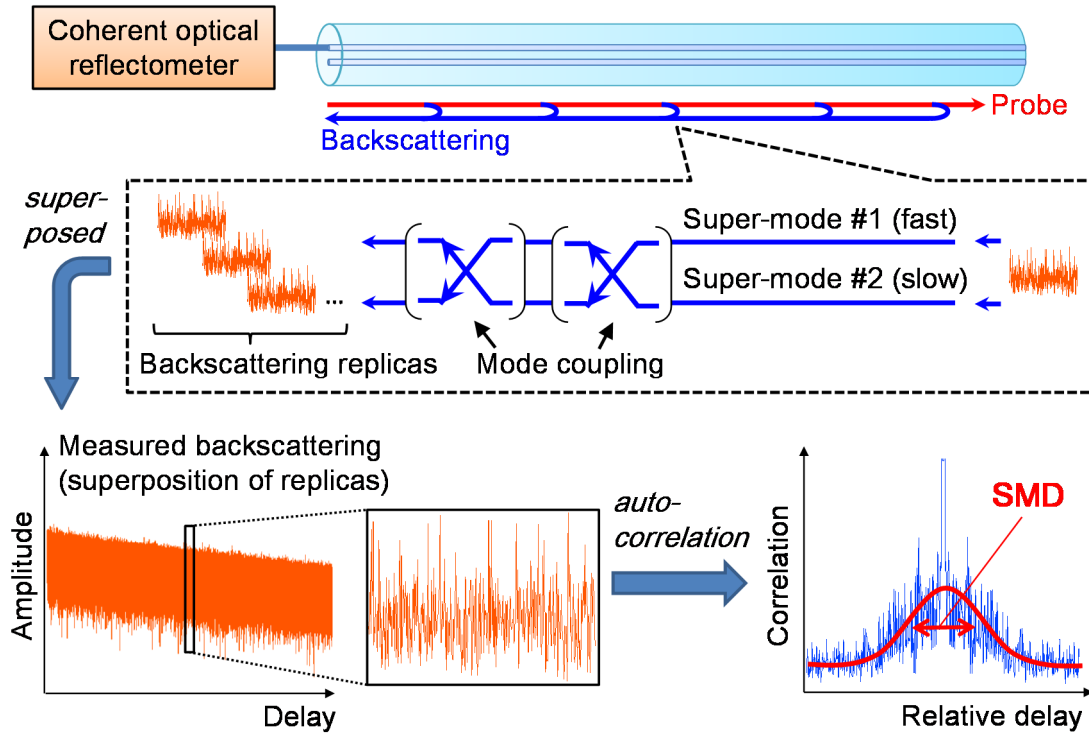


Figure 4-1. Schematic diagram of proposed SMD measurement.

According to previous reports, the SMD of an SC-MCF is of sub- $\mu\text{s}$  order even with a distance of tens of kilometers [4-1]-[4-4]. C-OFDR is an attractive way of realizing the proposed method because it enables us to obtain the backscattering amplitude with ps-order resolution [4-6]-[4-8].

The principle of our SMD measurement is similar to that of a low coherence interferometric method standardized as an alternative test method for PMD measurement [4-10], and our algorithm for characterizing SMD with an auto-correlation fringe is also based on Ref. [4-10]. With the interferometric method,

#### *4. Distributed measurement of spatial mode dispersion along coupled multicore fiber*

the overall dispersion is characterized from the auto-correlation fringe of low coherence signals from a broadband light source using a Michelson or Mach-Zehnder interferometer [4-10], [4-11]. In contrast, our proposed method uses randomly fluctuating Rayleigh backscattering amplitudes and their digitally processed auto-correlation fringes, thus allowing us to obtain the distributed SMD along fibers.

## 4.2. Measurement principles

### 4.2.2. Correlation noise suppression

In this subsection, I discuss the measurement accuracy of the proposed method and describe a technique for improving it.

There are two factors that degrade the measurement accuracy;

(1) Correlation fluctuation overlapping the Gaussian-like correlation fringe,

(2) Noise floor caused by uncorrelated backscattering components,

as shown in Fig. 4-2. The first factor is caused by the random interference between backscattering replicas, which is described as  $C(\tau)$  in Eq. (4-3) and (4-4). The second factor results from the imperfect randomness of the backscattering waveform.

To suppress these error factors, frequency-shift averaging (FSAV) is applied to the auto-correlation fringe. Figure 4-3 illustrates the FSAV technique in the SMD measurement. With this technique, the measurement process including the C-OFDR, extraction of the backscattering amplitude with an arbitrary section, and its auto-correlation, are performed multiple times, where the center optical frequencies (wavelengths) of the probe lights are different. After that, the multiple auto-correlation fringes are averaged. The phase differences between the backscattering replicas change with respect to the wavelength of the probe light. As a result, the correlation fluctuations are different for each measurement. Moreover, the backscattering waveform itself varies with respect to the probe wavelength [4-12], and so the noise floor of uncorrelated backscattering components also varies. Therefore, both of the above two error factors can be suppressed by averaging the auto-correlation fringes obtained with different wavelengths.

4. Distributed measurement of spatial mode dispersion along coupled multicore fiber

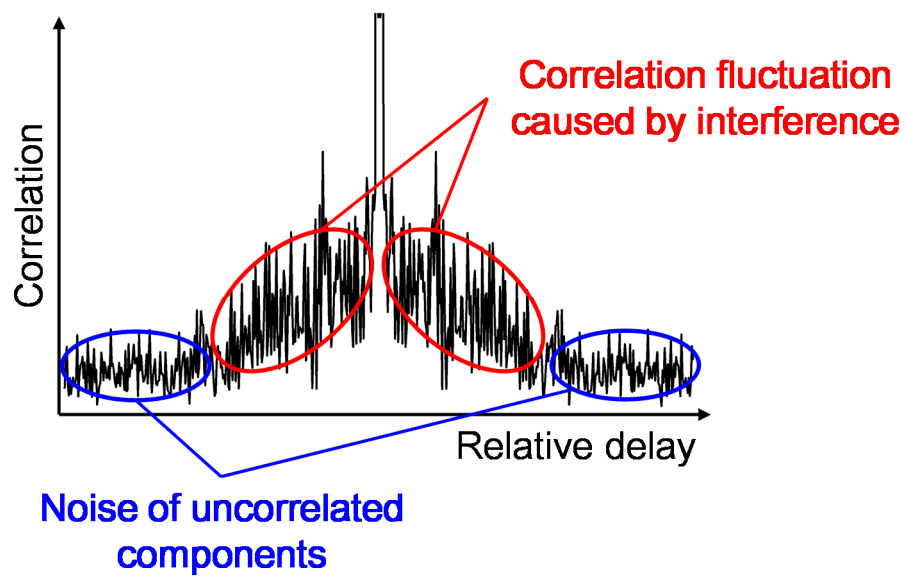


Figure 4-2. Error factors in SMD measurement.

## 4.2. Measurement principles

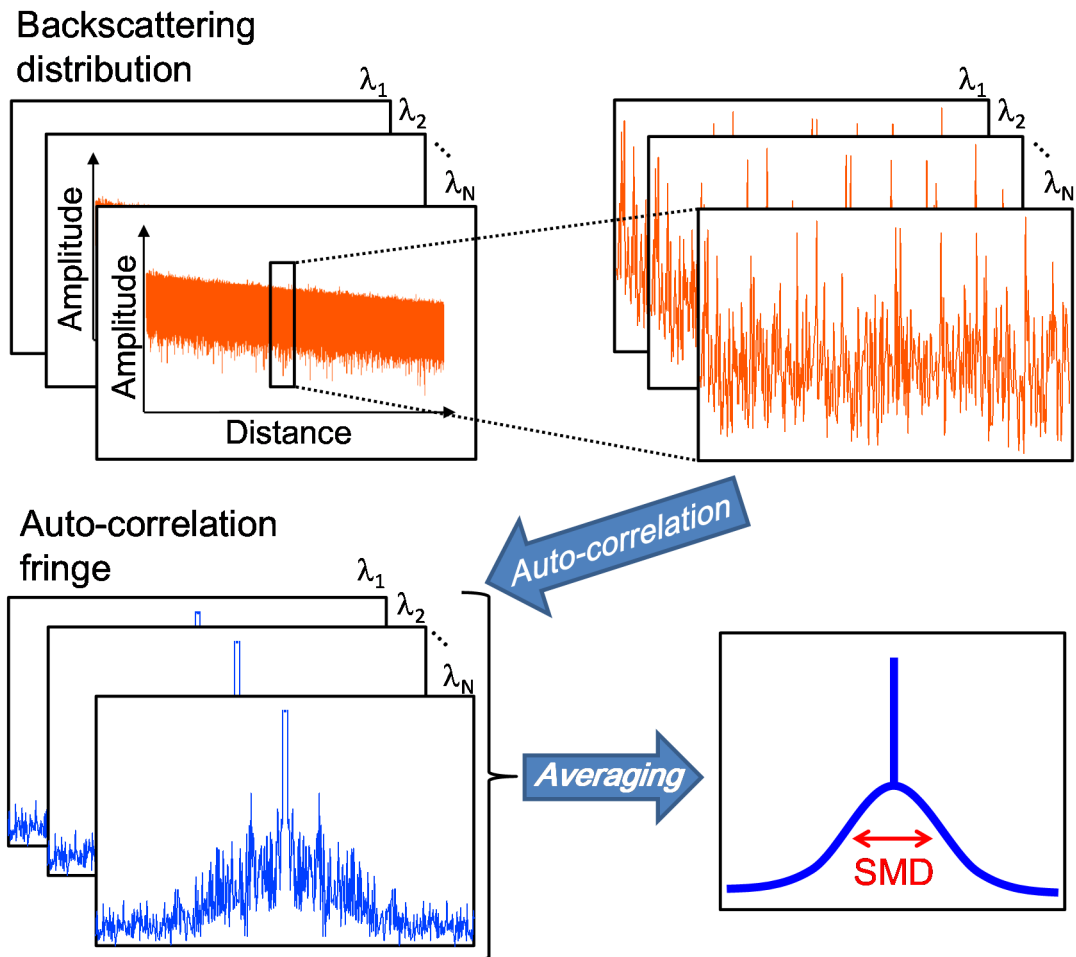


Figure 4-3. Schematic illustration of FSAV in SMD measurement.

### 4.3. Experimental setup

Figure 4-4 shows the C-OFDR setup used in our experiment. The laser source was a continuously tunable laser diode whose wavelength sweep rate was 100 nm/s. I swept 8 nm centered at 1550 nm, which corresponds to a delay time resolution of 1 ps, and a spatial resolution of 100  $\mu\text{m}$ . The probe light was launched into an arbitrary core of the FUT with a fan-in/fan-out (FI/FO) device. The backscattered light was coherently detected with a polarization diversity receiver, and acquired by an A/D converter with a sampling rate of 1.25 GS/s and sampling points of 100 MSa. In this setup, the measurable distance range was about 4 km, which was limited by the sampling rate. The measured delay resolution was almost the theoretical value over the measurement range achieved by compensating for the sweep nonlinearity of the laser with the concatenative reference method [4-13], [4-14] based on the reference signal obtained with the Mach-Zehnder interferometer shown on the left in Fig. 4-2. The backscattering amplitudes in the delay time domain were obtained by Fourier-transforming the beat signals. In the auto-correlation analysis, the inner product of the Jones vectors was calculated with two different polarization signals.

### 4.3. Experimental setup

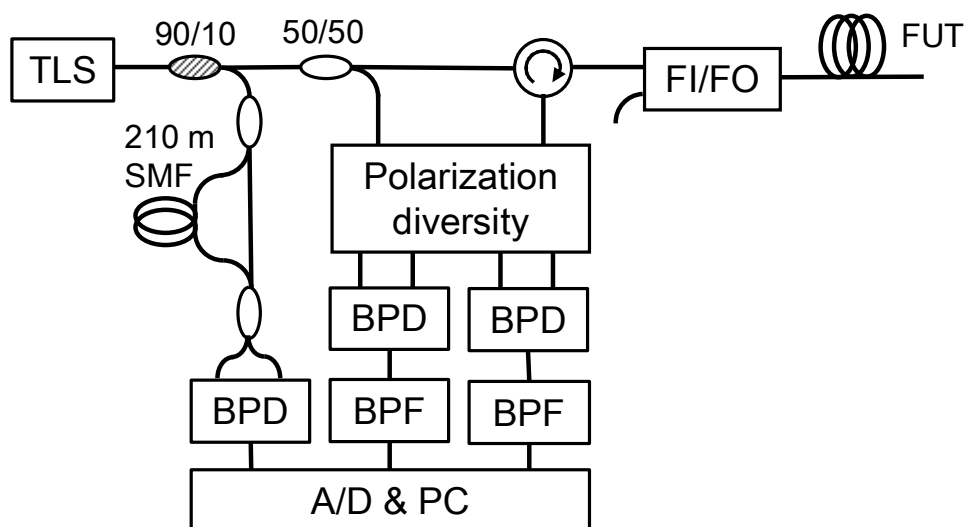


Figure 4-4. Setup for C-OFDR measurement. TLS: tunable laser source, SMF: single-mode fiber, BPD: balanced photodetector, BPF: band-pass filter.

I prepared three kinds of two-core fibers, FUT-4.1, 4.2 and 4.3 as shown in Tab. 4-1 and Fig. 4-5. To introduce strong mode coupling, the core alignments of FUT-4.3 were twisted along the fiber with a twisting rate of  $4\pi$  rad./m, which was achieved by rotating the preform during the drawing process [4-4]. I estimated the overall SMD and SMD coefficient of each FUT by using a fixed analyzer method [4-2], [4-4], [4-10]. Figure 4-6 shows the setup used for the fixed analyzer method. In this setup, SMFs were spliced under a cladding alignment condition on both the input and output sides of the FUT. The overall SMD was characterized by Fourier-transforming the output spectrum pattern and calculating the second moment of the transformed data. Figure 4-7 shows the Fourier-transformed results measured for  $1550 \pm 8$  nm. The SMD coefficients of FUT-4.1, 4.2 and 4.3 were estimated to be 35, 38 and 15 ps/çkm, respectively.



4. Distributed measurement of spatial mode dispersion along coupled multicore fiber

Table 4-1. Characteristics of FUTs.  $D$ : core pitch,  $\Delta$ : refractive index difference,  $\langle \tau \rangle$ : SMD coefficient,  $R$ : bending radius,  $L$ : fiber length.

	$D$ ( $\mu\text{m}$ )	$\Delta$ (%)	$\langle \tau \rangle$ (ps/çkm)	$R$ (mm)	$L$ (m)
FUT-4.1	20	0.35	35	80	10307
FUT-4.2	25	0.35	38	80	9069
FUT-4.3 (twisted)	25	0.35	15	50	794

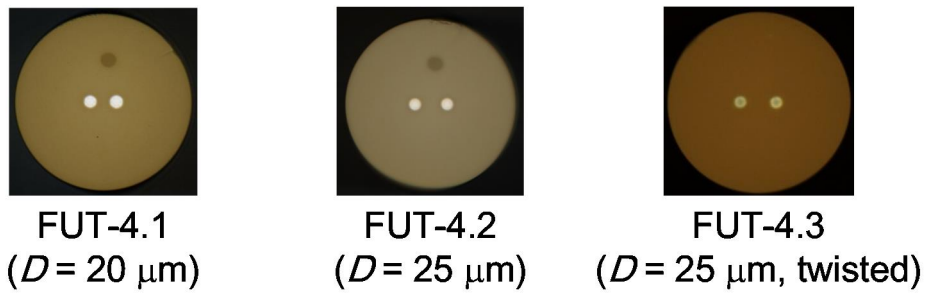


Figure 4-5. FUT cross-sections.

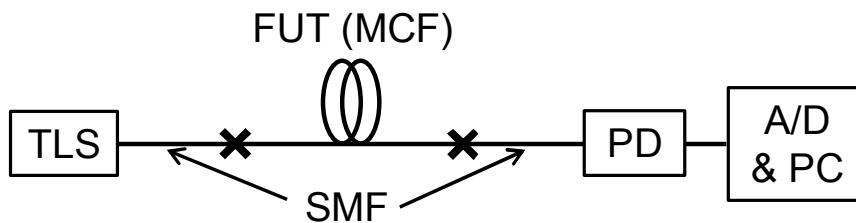


Figure 4-6. Setup for fixed analyzer method. PD: photodetector.

### 4.3. Experimental setup

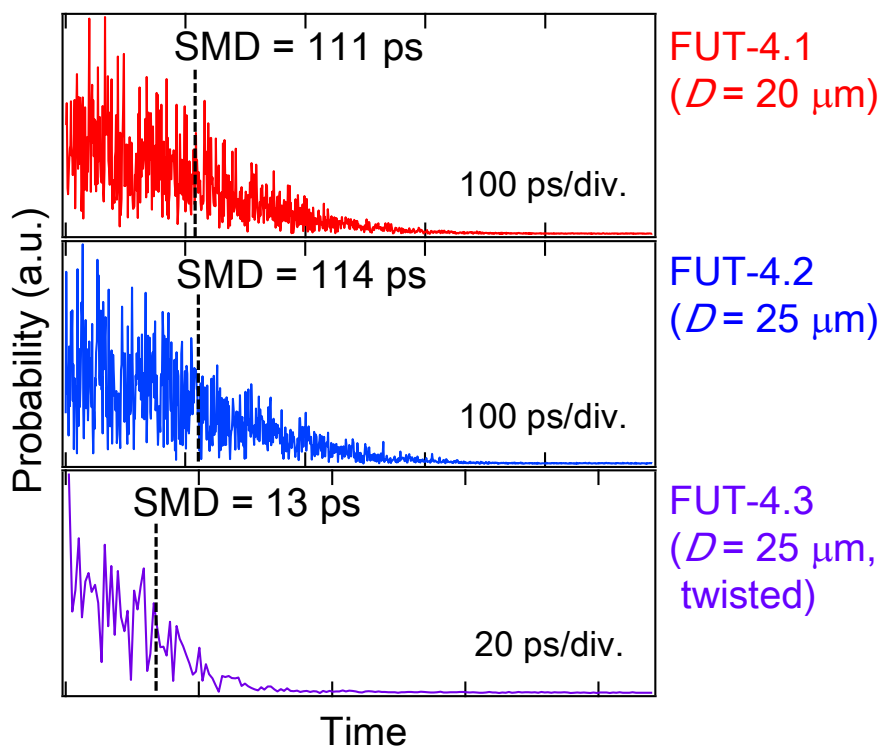


Figure 4-7. Fourier transforms of output spectra measured with fixed analyzer method.

## 4.4. Experimental results and discussion

Figure 4-6 shows auto-correlation fringes measured at arbitrary positions for each FUT. The auto-correlation of each position was calculated with 400000 data points of backscattering amplitude, which corresponds to a 40-m fiber section. A Gaussian-like correlation distribution was observed with each FUT, and their widths broadened with distance. Figure 4-7 shows the SMDs along each FUT characterized by calculating with the square root of the second moment of the auto-correlation fringes shown in Fig. 4-6. The calculations were performed with an algorithm based on that in the appendix of Ref. [4-10], where the central peak with a width of several times the delay resolution was eliminated. I observed the SMD growth, which was proportional to  $\zeta L$  for each FUT, as expected. By applying least square fittings to the measured SMDs, the SMD coefficients of FUT-4.1, 4.2 and 4.3 were estimated to be 40, 35 and 21 ps/ $\zeta$ km, respectively, and these values were in good agreement with the results characterized with the fixed analyzer method. The variation in the measured SMDs along each FUT was considered to be the result of measurement error caused by the correlation noise mentioned in Section 2, or the randomly fluctuating appearance of the correlation fringe caused by the phase difference among backscattering replicas as implied in Eq. (4-4).

#### 4.4. Experimental results and discussion

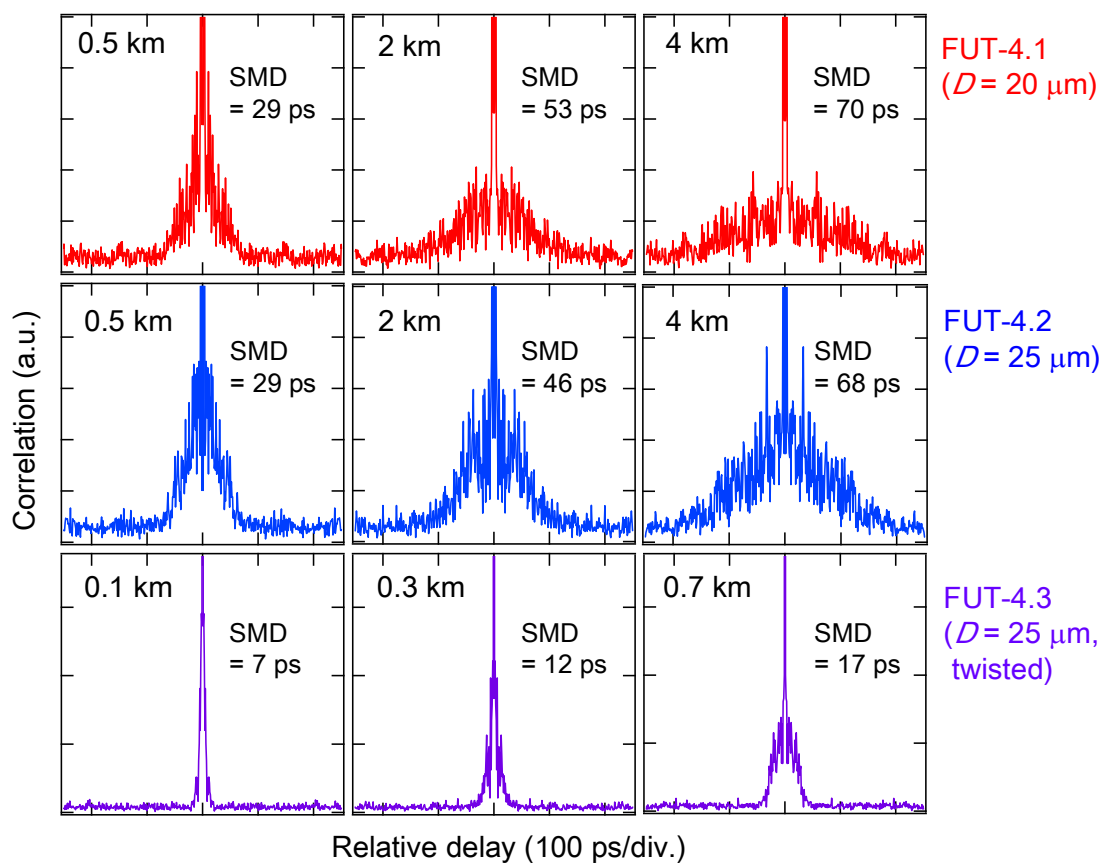


Figure 4-8. Auto-correlation fringes of backscattering amplitudes.

4. Distributed measurement of spatial mode dispersion along coupled multicore fiber

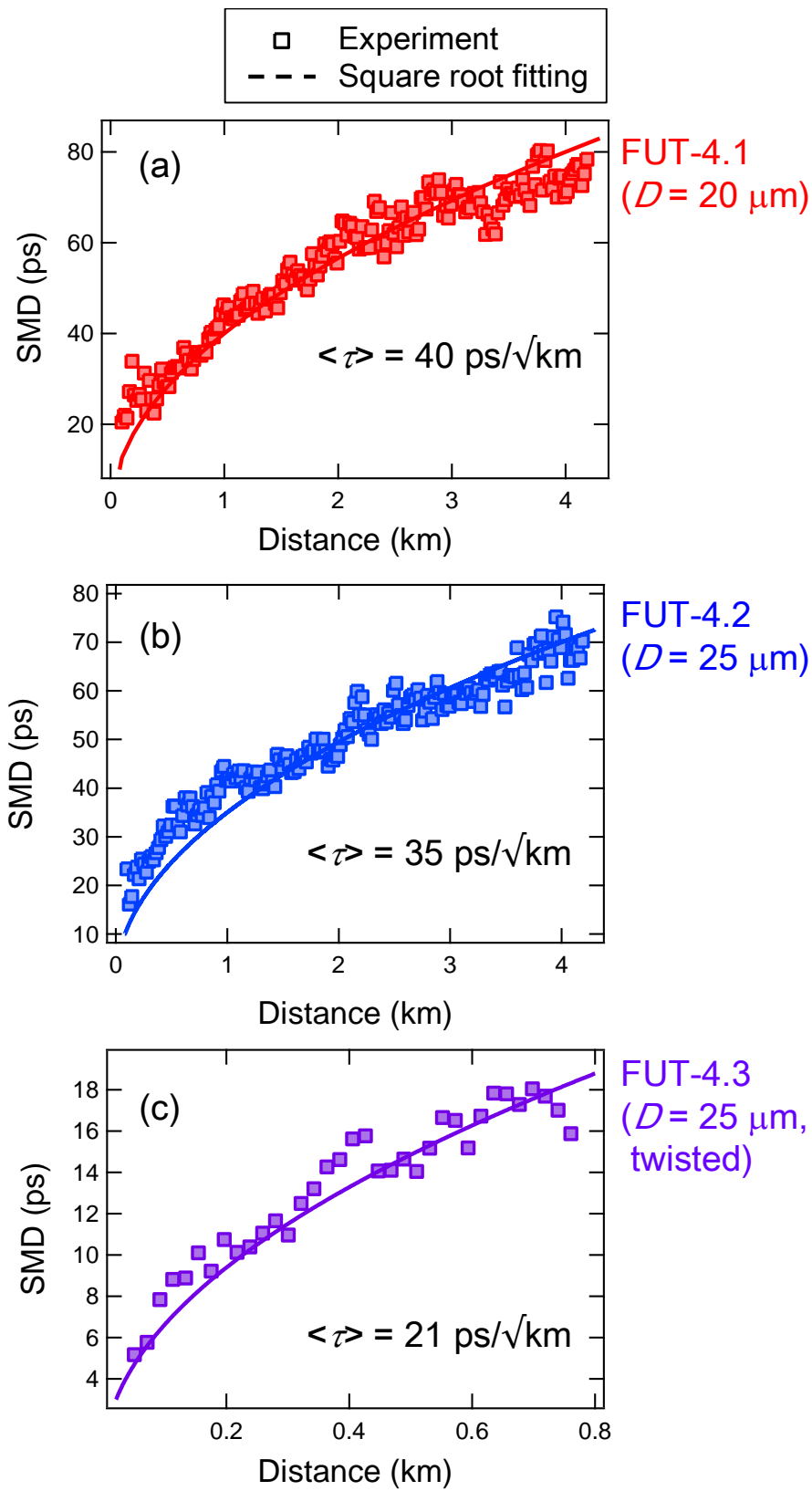


Figure 4-9. SMDs along (a) FUT-1, (b) FUT-2, (c) FUT-3.

#### 4.4. Experimental results and discussion

Next, I connected FUT-4.2 to the end of FUT-4.3, and investigated the SMD growth along the concatenated fibers, with a view to distinguishing the SMD difference caused by fiber twisting. Figure 4-8 shows the SMDs along the concatenated fibers plotted with respect to the square root of distance. A clear difference between the SMD coefficients of FUT-4.3 and 4.2 could be observed. According to the fittings, the SMD coefficients of the fiber sections of FUT-4.3 and 4.2 were estimated to be 21 and 38 ps/√km respectively, which agreed with the single-fiber characteristics shown in Fig. 4-7. With our method, the measurable distance range is in a trade-off relationship with the SMD resolution due to the sampling rate limit of the A/D converter. A higher sampling rate would help us to observe the SMD growth and distinguish the SMD difference more clearly over a long range.

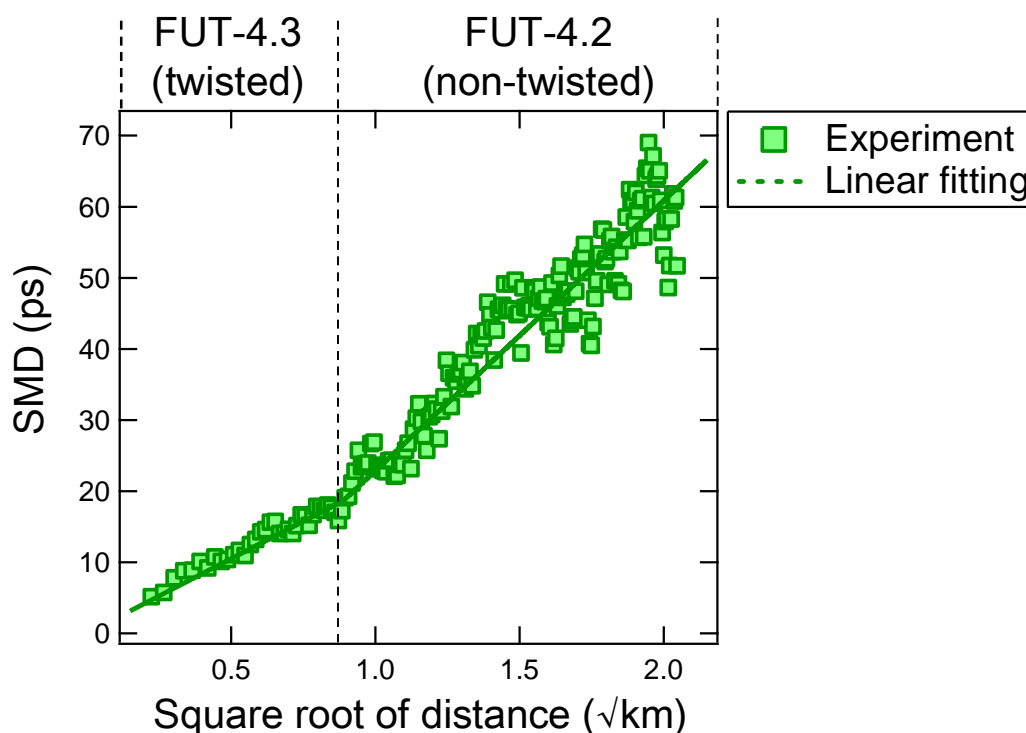


Figure 4-10. SMDs along FUT-4.2 and 4.3.

#### *4. Distributed measurement of spatial mode dispersion along coupled multicore fiber*

Finally, I investigated the effect of FSAV with FUT-4.1 experimentally to improve the measurement accuracy. C-OFDR measurements were performed up to 10 times while the center wavelength was shifted with 4 nm intervals in the C-band. Each C-OFDR measurement was performed with a wavelength sweep range of 4 nm, and the auto-correlation at each position was calculated with 100000 data points of backscattering amplitude, which corresponded to a 23 m fiber section. Figure 4-11 shows the auto-correlation fringes obtained with averaging numbers of 0, 2, and 10, at fiber positions of 0.5, 2, and 3.5 km, respectively. The correlation fluctuations and noise floors were reduced by FSAV, and a Gaussian-like distribution could be clearly observed after averaging 10 times. Figure 4-12 shows the results of SMD distribution measurements with/without FSAV. While the measured SMDs were randomly varied along the fiber before applying FSAV, a clear  $\zeta L$ -dependence could be observed in the FSAV results. Figure 4-13 shows the averaging number dependences of the SMD fluctuations. The SMD fluctuations were characterized with the least mean square error from  $\zeta L$ -fitting in a 2 to 4 km section. For comparison, I plotted the results obtained with the backscattering lengths of 6 and 90 m that we used for the auto-correlation. In spite of the 15-fold difference in the correlation lengths, the SMD fluctuation of the 6-m-length with FSAV could be reduced to smaller than that of the 90-m-length without FSAV. That means FSAV can be applied as a technique for improving the spatial resolution of SMD distribution.

4.4. Experimental results and discussion

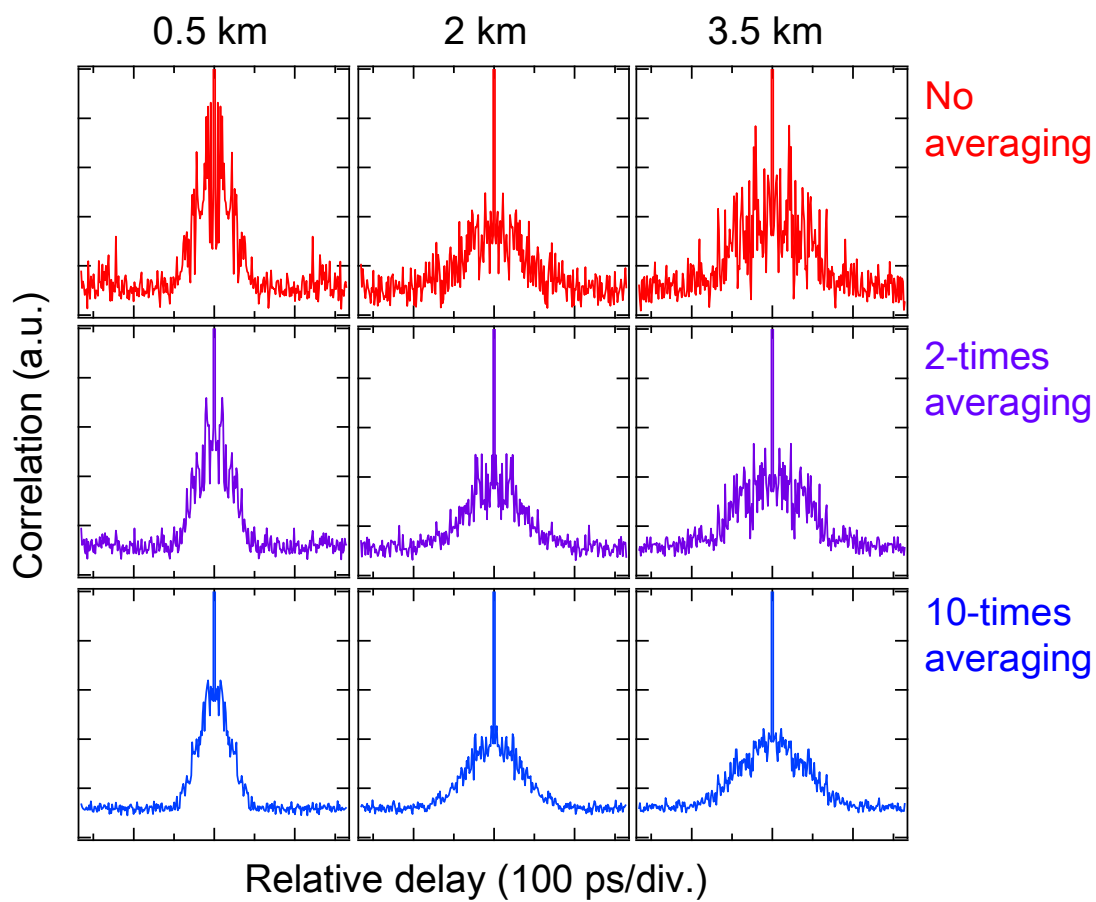


Figure 4-11. Auto-correlation fringes obtained with/without FSAV.



4. Distributed measurement of spatial mode dispersion along coupled multicore fiber

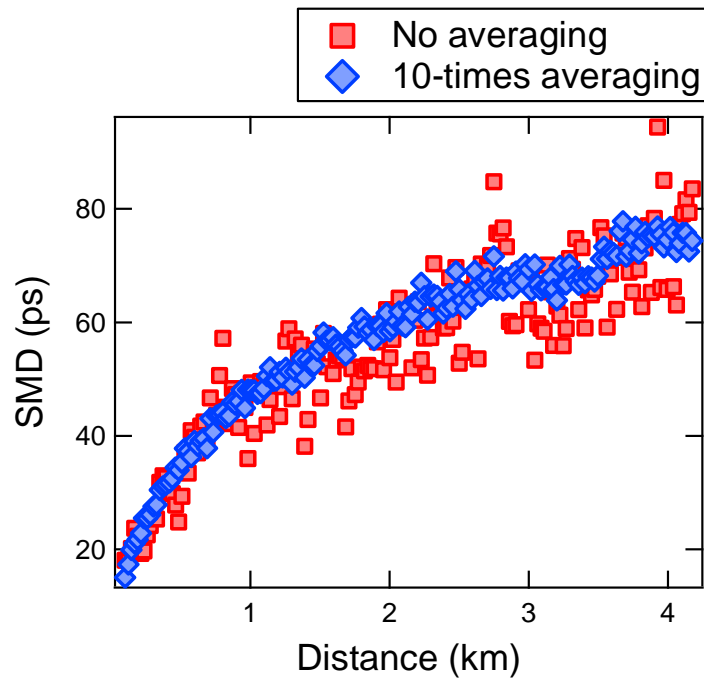


Figure 4-12. SMD distribution with/without FSAV.

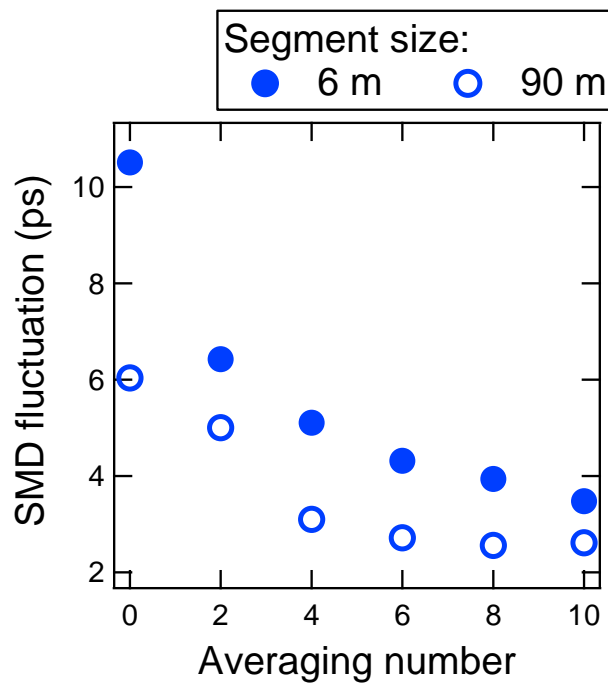


Figure 4-13. Averaging number dependence of SMD fluctuation.

## **4.5. Conclusion**

I proposed a technique for measuring the SMD distribution along an SC-MCF by auto-correlating the Rayleigh backscattering amplitudes obtained with C-OFDR. I used the proposed method to demonstrate SMD distribution measurement with three kinds of SC-MCFs, and the results agreed well with those obtained with the conventional method. Our method also enabled us to distinguish the difference between the SMDs in twisted and non-twisted fiber sections in concatenated SC-MCFs. I believe that our method will prove a powerful tool for investigating structural uniformity after fiber manufacture or cabling, or maintaining transmission lines after installation.



# 5. High-resolution measurement of differential mode delay of few-mode fiber link

## 5.1. Introduction

DMD in an FMF link is an important parameter as regards MDM systems. Recent studies have proposed some DMD reduction techniques including low-DMD fibers designed with graded-index based profiles [5-1], [5-2] and a DMD managed transmission line where positive- and negative-DMD fibers are combined [5-3] with the aim of reducing the complexity of MIMO processing. High-resolution DMD measurements are required if we are to characterize such low-DMD transmission lines accurately.

Certain DMD measurement methods have been reported including a time-domain method [5-4], and a frequency-domain (FMCW) method [5-5]-[5-8]. In the time-domain method, the temporal pulse width corresponds to the DMD resolution, and is typically a few tens of picoseconds. However, a shorter pulse width inevitably leads to a wider spectral width. As a result, the achievable resolution is limited by the pulse broadening caused by chromatic dispersion. Moreover, the setup needed for the time-domain method is complicated and expensive for introducing an ultra-short pulse source and a fast detection system. In contrast, the FMCW method is very attractive because the DMD measurements can be easily performed with a simple configuration and a slow detection system. However, the resolution of the FMCW method is also limited by chromatic dispersion because it is inversely proportional to the frequency sweep range of the probe light [5-8], [5-9]. Although the effect of chromatic dispersion

## *5. High-resolution measurement of differential mode delay of few-mode fiber link*

can be compensated for by using an auxiliary interferometer where the dispersion of the delay fiber is equal to that of the FMF for the FMCW setup [5-8], [5-9], such a delay fiber is not always available, and the dispersion is typically different for each propagation mode.

In this chapter, I present a way of realizing a high-resolution DMD measurement in a narrower optical bandwidth than with the conventional FMCW method. With our proposed method, the DMD is characterized by referencing the phases of the FMCW signals for different modes, and the resolution depends not only on the frequency sweep range but also on the temporal phase fluctuations. I also employ signal averaging with the proposed method to enhance the resolution by reducing the phase fluctuations caused by random noises or mode couplings.

This chapter is organized as follows. Section 5.2 reviews the principle of DMD measurement with the FMCW method using the conventional and proposed methods. Section 5.3 describes our FMCW configuration and experimental results. Section 5.4 provides the conclusion.

## 5.2. Measurement principles

### 5.2.1. Fourier-transforming analysis with conventional method

In this subsection, I review the principle of the conventional transmission-type FMCW method used to measure the DMD.

Figure 5-1 shows an example setup for the FMCW method. A continuous light wave whose frequency is swept with respect to time is divided by the coupler and used as a probe light and a local light. The probe light is launched into an FMF with multiple propagation modes, and detected with a coherent receiver. When the interference between the probe and local lights is taken into account, the beat signal  $I(t)$  can be written as

$$I(t) \propto \sum_m a_m \cos 2\pi\gamma\tau_m t, \quad (5-1)$$

where  $a_m$  and  $\tau_m$ , respectively, are the amplitude and delay time of the probe light in the  $m$ th mode, and  $\gamma$  is the frequency sweep rate. The phase noise is ignored in Eq. (5-1) for simplicity. As described in Eq. (5-1), the beat frequency of  $I(t)$  is proportional to the delay time, thus a Fourier transform of  $I(t)$  is performed for DMD analysis. Since the spectral resolution of the Fourier transform is inversely proportional to the measurement time  $T$ , and the beat frequency is proportional to  $\gamma$ , the DMD resolution  $\Delta\tau$  of the conventional method is

$$\Delta\tau = \frac{1}{\gamma T} = \frac{1}{F}, \quad (5-2)$$

where  $F$  is the frequency sweep range. The resolution is directly related to the sweep range, thus a widely swept light is required for a high-resolution measurement. However, a large  $F$  increases the effect of chromatic dispersion, and as a result, the resolution actually becomes larger than  $1/F$ .

5. High-resolution measurement of differential mode delay of few-mode fiber link

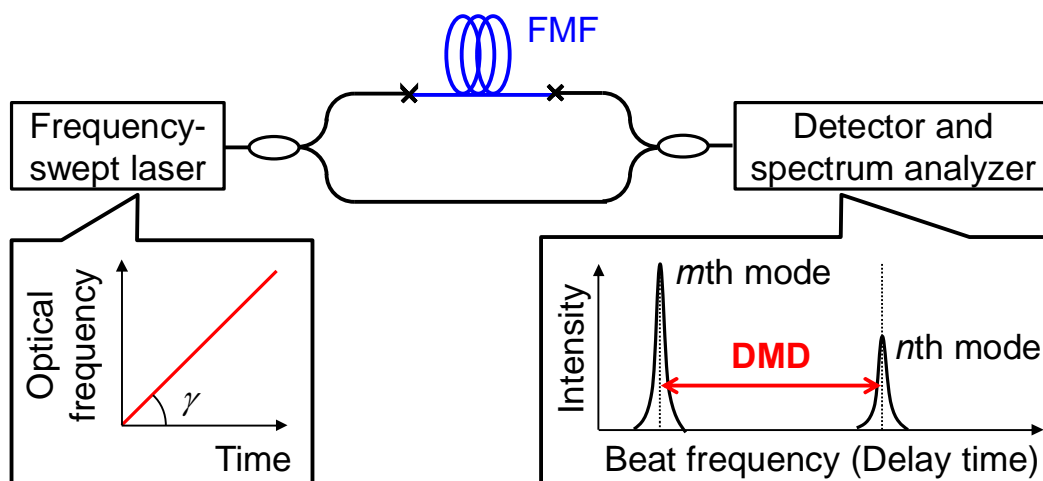


Figure 5-1. Basic setup for conventional FMCW method.

## 5.2. Measurement principles

### 5.2.2. Phase reference technique with proposed method

I introduce a phase reference technique for the FMCW method to realize higher-resolution DMD measurements without expanding  $F$ . Figure 5-2 shows the FMCW setup we used for the proposed method. With this method, we obtain the FMCW signals of different modes individually by utilizing a mode MUX and DEMUX. After that, the phase component of each beat signal is extracted by performing a Hilbert transform, in which the phase of the signal shifts by  $\pi/2$ , and by calculating an arc tangent with the original and transformed signals. The phase signal of the  $m$ th mode  $\theta_m(t)$  can be written as

$$\theta_m(t) = \tan^{-1} \frac{H[I_m(t)]}{I_m(t)} = 2\pi\gamma\tau_m t + \varphi_m(t) + \xi_m, \quad (5-3)$$

where  $I_m(t)$  and  $H[I_m(t)]$  are the beat signal of the  $m$ th mode and its Hilbert-transformed function, respectively,  $\varphi_m(t)$  is phase noise, and  $\xi_m$  is a phase constant. Then, the phase difference between the  $m$ th and  $n$ th modes is

$$\theta_n(t) - \theta_m(t) = 2\pi\gamma(\tau_n - \tau_m)t + \varphi_n(t) - \varphi_m(t) + \xi_n - \xi_m. \quad (5-4)$$

Figure 5-3 shows an example of the phase difference after unwrapping. The phase difference increases linearly with respect to time while randomly fluctuating due to the phase noise. Then, the temporal phase change rate, which is the angular frequency difference between the  $m$ th and  $n$ th modes, is related to the DMD as  $\tau_n - \tau_m$ . Thus the DMD can be characterized by applying a linear fitting to the phase difference and analyzing the change rate. Since the change rate can be determined when the total phase change in the measurement time is larger than the phase noise, the DMD resolution of the proposed method can be defined as

$$\Delta\tau = \frac{\sigma}{2\pi F}, \quad (5-5)$$



## 5. High-resolution measurement of differential mode delay of few-mode fiber link

where  $\sigma$  denotes the standard deviation of the phase fluctuation from linear fitting. The resolution depends not only on  $F$  but also on  $\sigma$ , thus a higher resolution can be realized without expanding  $F$  by reducing  $\sigma$  with certain methods such as the resampling technique reported in [5-9] and [5-10]. Moreover, the effect of chromatic dispersion on the proposed method depends on the differential dispersion between different modes, while the conventional method is affected by the individual dispersion of each mode. Since the differential dispersion is generally very small, the proposed method has the potential to achieve much higher resolution than the conventional method.

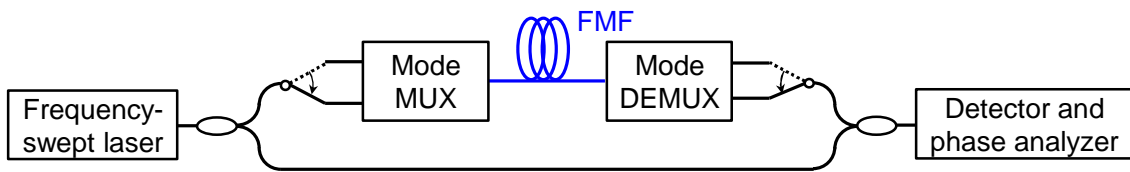


Figure 5-2. Setup for phase-referencing FMCW method.

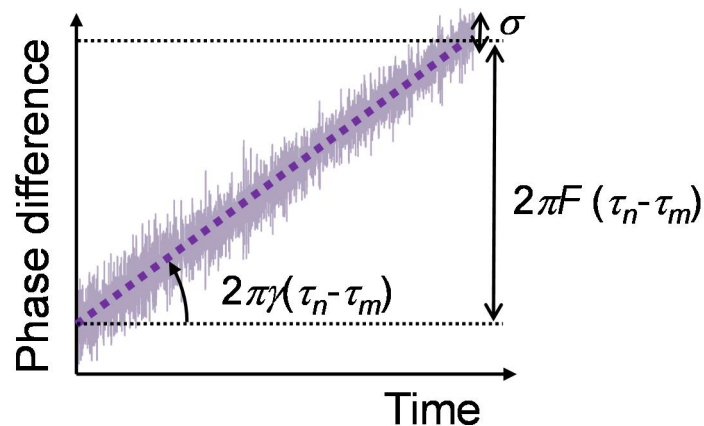


Figure 5-3. Unwrapped phase difference of beat signals.

## 5.2. Measurement principles

### 5.2.3. Mode coupling effect in proposed method

In Subsection 5.2.2, I assumed that the beat signals of different modes are detected individually. However, there are actually some undesired coupling modes in the FUT or mode MUX/DEMUX. In this subsection, I describe the effect of mode coupling in our proposed method and a technique for its reduction.

When mode coupling is taken into account, the beat signal obtained through the  $m$ th mode ports of the mode MUX/DEMUX can be written as a superposition of the signals whose beat frequencies (delay times) are different,

$$I'_m(t) \propto \cos \phi_m(t) + \sum_{i \neq m} \alpha_i \cos \phi_i(t), \quad (5-6)$$

$$\phi_m(t) \equiv 2\pi\gamma\tau_m t + \xi_m, \quad (5-7)$$

where  $\alpha_i$  is the relative amplitude of the  $i$ th coupled mode. I neglected the phase noise in Eq (5-6) for simplicity. In a similar manner to Eq. (5-3), the phase component of  $I\phi_m(t)$  can be calculated as (see Appendix C.)

$$\begin{aligned} \theta'_m(t) &= \tan^{-1} \frac{\sin \phi_m(t) + \sum_{i \neq m} \alpha_i \sin \phi_i(t)}{\cos \phi_m(t) + \sum_{i \neq m} \alpha_i \cos \phi_i(t)} \\ &= \phi_m(t) + \tan^{-1} \frac{\sum_{i \neq m} \alpha_i \sin[\phi_i(t) - \phi_m(t)]}{1 + \sum_{i \neq m} \alpha_i \cos[\phi_i(t) - \phi_m(t)]}. \end{aligned} \quad (5-8)$$

The first and second terms are the phase signals of the non-coupled  $m$ th mode, and the third term represents the temporally nonlinear phase fluctuation caused by the mode coupling. Since the DMD resolution of the proposed method is determined by the phase fluctuation, Equation (5-7) implies that the mode coupling causes the resolution degradation in our proposed method.

## 5. High-resolution measurement of differential mode delay of few-mode fiber link

To reduce the phase fluctuations and improve the resolution, a temporally moving averaging technique using multiple measurement data sets, namely time-shift averaging (TSAV), is applied for  $\theta_m(t)$ . Figure 5-4 shows a schematic diagram of the TSAV. With this technique, multiple delayed phase signals obtained at different times during the laser sweeping are averaged. Since the initial phases of the multiple signals are different, the phase fluctuation can be reduced by this averaging process. The fluctuation reduction mechanism in TSAV is similar to that of a well-known moving averaging technique. Since the phase fluctuations can be treated as high-frequency noises, the moving averaging is effective in reducing it by acting as a low-pass filter. However, when the moving averaging is utilized with single-phase data, the total time range, which corresponds to  $F$ , is reduced by the moving process, while the DMD resolution is inversely proportional to  $F$  as described in Eq. (5-5). In contrast, the fluctuation can be reduced while maintaining  $F$  with TSAV by using the delayed phases obtained with same time length. Note that the total time shift in TSAV is related to the effect of both the phase fluctuation reduction and chromatic dispersion. As TSAV is performed with a large time shift, the phase fluctuations can be more effectively reduced thanks to the low-pass filtering effect, although the fluctuations are unpredictable due to the mode coupling condition. However, the phase change rate of the non-coupled mode then becomes inconstant due to the chromatic dispersion. TSAV should be performed in an adequate range where the effect of chromatic dispersion is very small.

5.2. Measurement principles

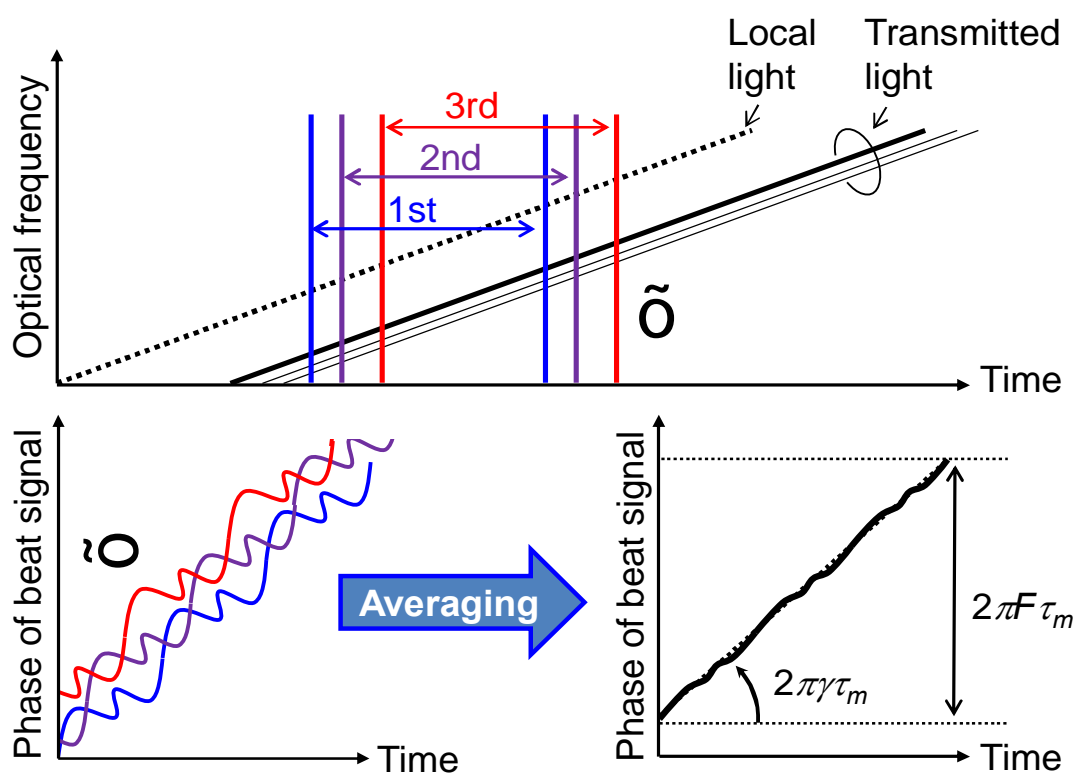


Figure 5-4. Schematic diagram of TSAV.

### 5.3. Experimental setup and results

#### 5.3.1. Experimental setup

Figure 5-5 shows our experimental setup. The laser source was a continuously tunable laser diode whose sweep rate was 12.5 THz/s. I swept 125 GHz, which corresponds to a delay time resolution of 8 ps with the conventional method. The setup included two interferometers, namely an auxiliary interferometer (AI) used for the resampling technique [5-9], [5-10], and a main interferometer (MI) to obtain the beat signal for each propagation mode of the FUT. As with the conventional FMCW method, the AI and MI had almost the same path length differences to compensate for the phase noise with the resampling technique. The probe light was excited into the FUT in each mode by using a mode MUX and DEMUX which consisted of spatial phase plates. The mode MUX/DEMUX supported the  $LP_{01}$  and  $LP_{11}$  modes, and the crosstalk between them was less than -20 dB.

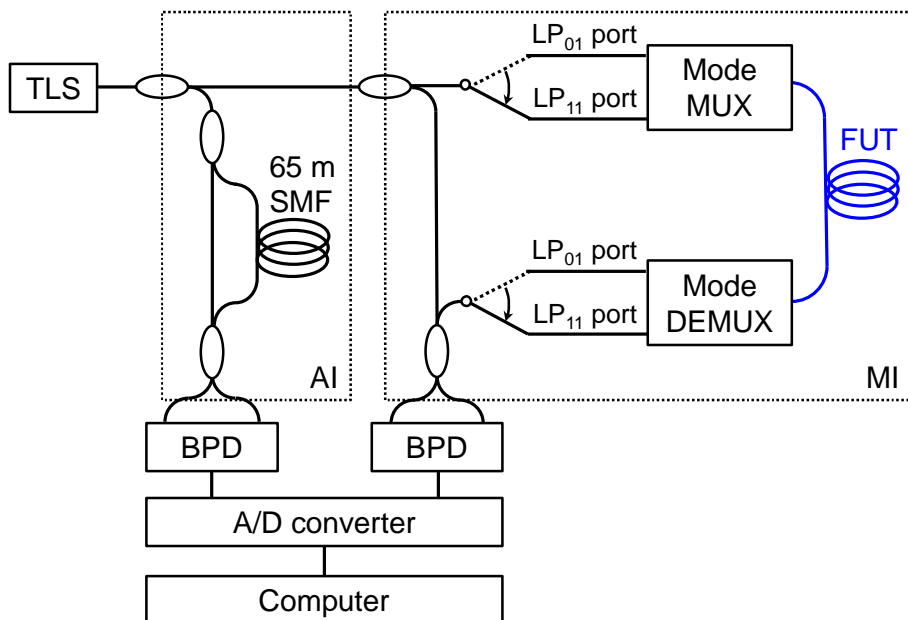


Figure 5-5. Experimental setup. TLS: tunable laser source, BPD: balanced photodetector.

### 5.3. Experimental setup and results

I prepared three kinds of two-mode fibers (TMFs) as FUTs: a 58 m-SI-TMF, a 57 m-GI-TMF, and an offset-spliced SI-TMF whose total length was 157 m. The fiber lengths were measured with an OTDR whose spatial resolution was 1 m. In the third FUT, we spliced 100 m- and 57 m-SI-TMFs, and the end of the FUT and the mode DEMUX, both with offset values of 2  $\mu\text{m}$ . The DMDs per unit length of the SI- and GI-TMFs were 2.2 and 0.07 ps/m, respectively. The respective dispersions of the LP<sub>01</sub> and LP<sub>11</sub> modes were 19.9 and 20.0 ps/(nm·km) in both FUTs.

## 5. High-resolution measurement of differential mode delay of few-mode fiber link

### 5.3.2. DMD measurement without mode coupling

Figure 5-6 shows the Fourier-transformed intensities of the beat signals of the  $LP_{01}$  and  $LP_{11}$  modes measured with the 58-m-SI- and 57-m-GI-TMFs. For comparison, the results obtained without the FUT (mode MUX and DEMUX were directly connected) are also shown in Fig. 5-6 (c). The beat frequency differences were 3.8, 2.3, and 2.3 kHz for the 58-m-SI-TMF, the 57-m-GI-TMF, and the MUX/DEMUX, respectively. By comparison with the MUX/DEMUX results, the DMD of the 58-m-SI-TMF was calculated to be 120 ps (2.07 ps/m). In contrast, Fig. 5-6 revealed no beat frequency difference between the 57-m-GI-TMF and MUX/DEMUX. This means that the DMD of the 57-m-GI-TMF could not be characterized with the conventional method in our experimental setup.

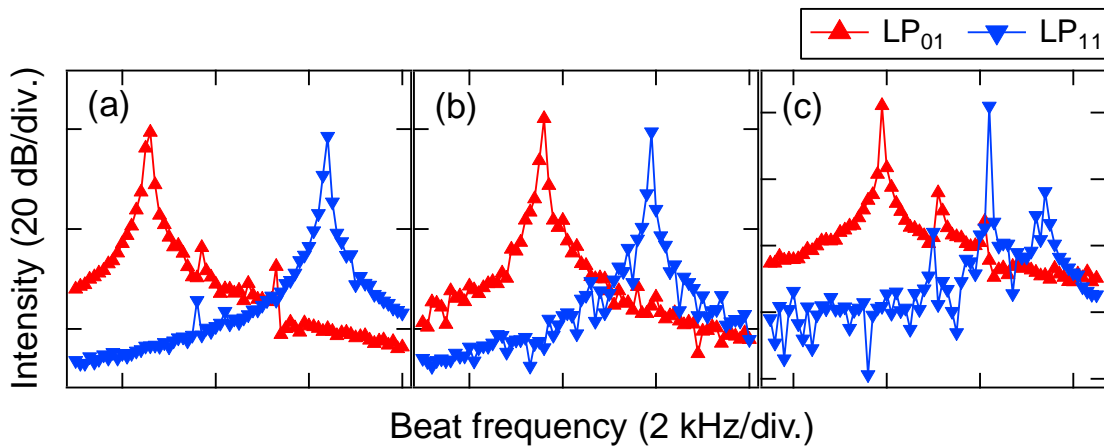


Figure 5-6. Fourier-transformed intensities of beat signals. (a) 58-m-SI-TMF, (b) 57-m-GI-TMF, (c) without FUT.

Figure 5-7 shows the phase differences between the beat signals of the  $LP_{01}$  and  $LP_{11}$  modes obtained with our proposed method. As expected, the phase differences

### 5.3. Experimental setup and results

increased linearly with respect to time for each FUT. The phase change rates differed for the FUT and MUX/DEMUX, even with the 57-m-GI-TMF. By applying linear fitting to Fig. 5-7, the DMDs of the 58-m-SI- and 57-m-GI-TMFs were measured and found to be 122 ps (2.10 ps/m) and 1.63 ps (0.03 ps/m), respectively. These results confirmed that our proposed method enables us to measure low DMDs that cannot be measured with the conventional method.

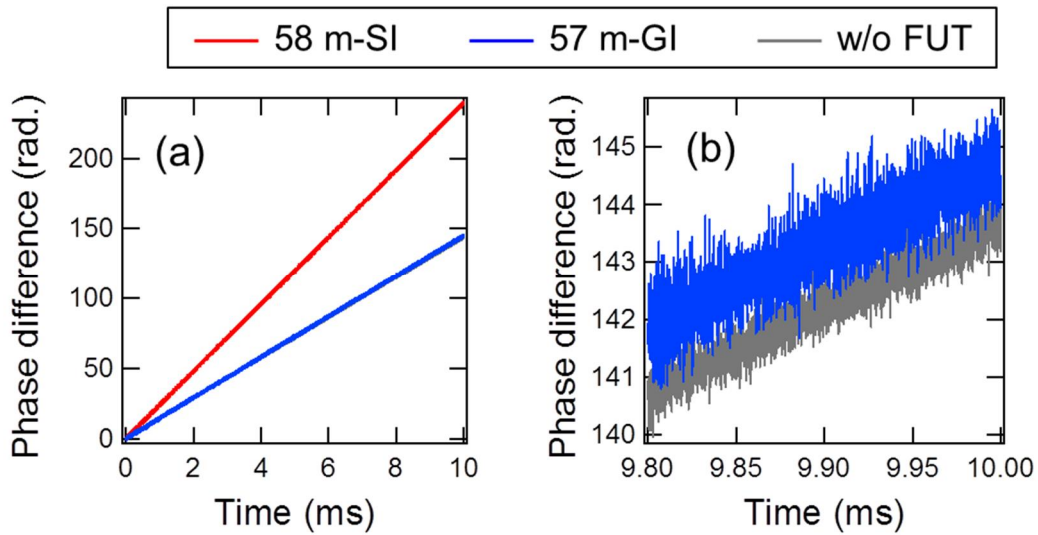


Figure 5-7. (a) Phase difference between beat signals of  $LP_{01}$  and  $LP_{11}$ , and (b) its extended view around 9.9 ms.

Figure 5-8 shows the phase fluctuations from the fittings. Since the DMD resolution of the proposed method is determined by the phase noise as mentioned in Section 5.2, the DMD resolutions could be characterized from Fig. 5-8. The resolutions were estimated to be 501 and 489 fs for the 58-m-SI-TMF and 57-m-GI-TMF, respectively, which were better than 1/15 the resolution obtained with the conventional method (8 ps).



5. High-resolution measurement of differential mode delay of few-mode fiber link

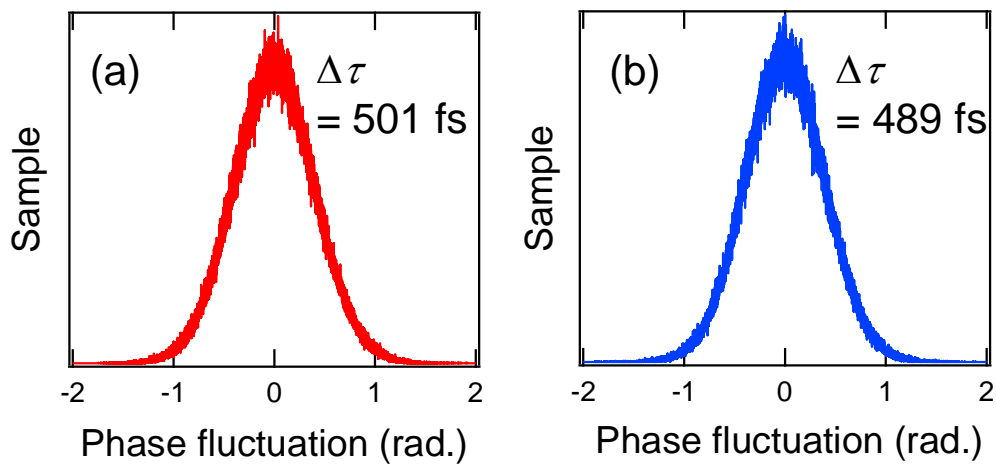


Figure 5-8. Phase fluctuation from linear fitting. (a) 58 m-SI-TMF, (b) 57 m-GI-TMF.

### 5.3. Experimental setup and results

#### 5.3.3. DMD measurement with mode coupling

Figure 5-9 shows the Fourier-transformed intensity of a beat signal measured with the offset-spliced SI-TMF where the propagation modes were coupled with each other at the splice points. In addition to the strong main peaks, which represent the non-coupled modes, small peaks caused by the mode coupling could be seen between the main peaks. The DMD between the non-coupled LP<sub>01</sub> and LP<sub>11</sub> modes characterized from the main peaks in Fig. 5-9 was 304 ps.

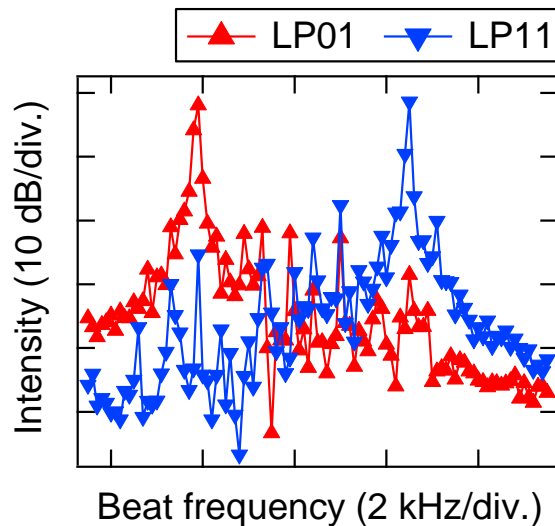


Figure 5-9. Fourier-transformed intensity of beat signals measured with offset-spliced SI-TMF.

Figure 5-10 shows the phase differences between the LP<sub>01</sub> and LP<sub>11</sub> modes measured with/without TSAV. For comparison, the result after non-shifted ensemble averaging is also represented in Fig. 5-10. The averaging numbers were 100 for both the shifted and non-shifted averaging. TSAV was performed with a total time shift range of 5 ms, which corresponded to an optical frequency shift of 62.5 GHz, where

## *5. High-resolution measurement of differential mode delay of few-mode fiber link*

the effect of chromatic dispersion could be neglected. I observed that the phase noises were reduced by averaging even in the non-shifted case. However, nonlinear phase fluctuations, which were considered to result from the mode couplings, still remained after the non-shifted averaging. In contrast, TSAV also reduced the nonlinear fluctuation. From the phase change rate in Fig. 5-10, the DMD was calculated to be 302 ps, which agreed well with the result in Fig. 5-9. I also characterized the DMD resolution from the phase fluctuation shown in Fig. 5-11. The resolutions obtained with non-averaging, non-shifted averaging, and TSAV were 685, 330, and 100 fs, respectively. The unsymmetrical characteristics of the phase fluctuations are considered to result from the mode coupling effects. By using our proposed method with TSAV, we achieved 1/80 the resolution of the conventional method without expanding the frequency sweep range. Our DMD measurement method can be extended to more than two modes if the corresponding mode MUX and DEMUX are available. Although the extinction ratio of MUXs/DEMUXs between higher order modes is generally lower than that between lower order modes, TSAV will be also effective for suppressing the effect of imperfect extinction.

### 5.3. Experimental setup and results

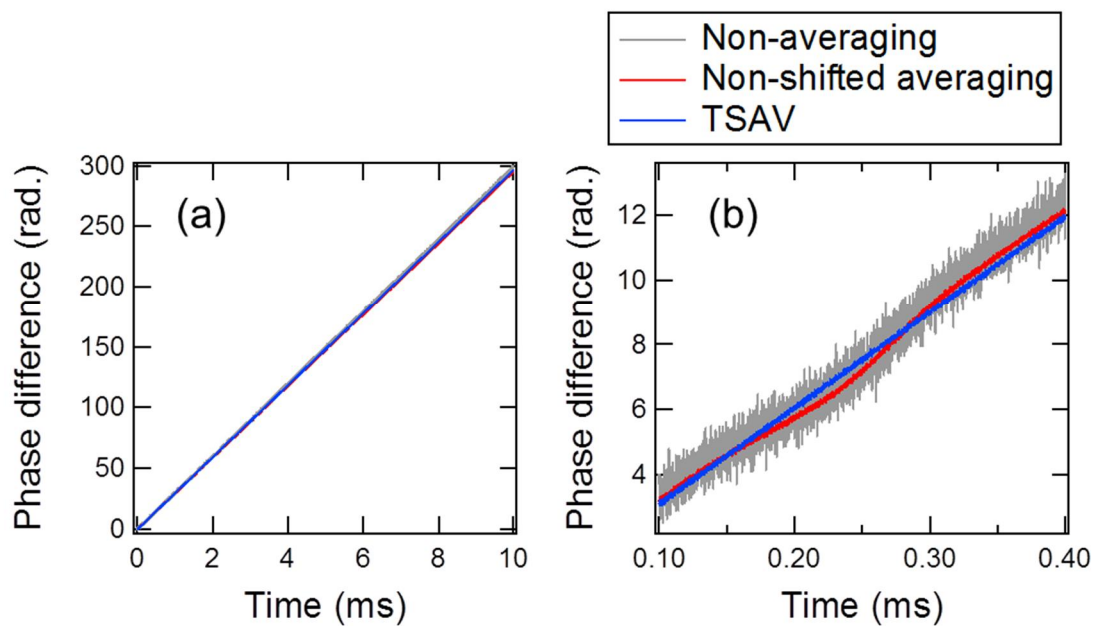


Figure 5-10. (a) Phase difference between beat signals of  $LP_{01}$  and  $LP_{11}$  modes measured with offset-spliced SI-TMF, and (b) its extended view around 0.25 ms.

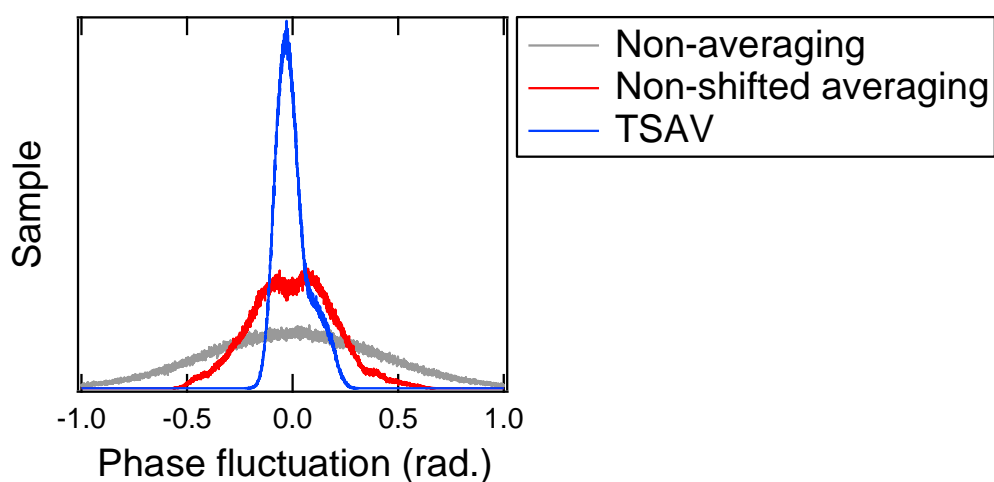


Figure 5-11. Phase fluctuation from linear fitting measured with offset-spliced SI-TMF.

## **5.4. Conclusion**

I proposed a high-resolution DMD measurement technique by referencing phases of FMCW signals with different modes. I confirmed experimentally that our proposed method could achieve resolution 15 times better than the conventional FMCW method, while the conventional method could not realize such an improvement without an increase in the optical bandwidth of the probe light. Moreover, signal averaging with the proposed method was effective in reducing the phase fluctuation resulting in a further improvement in the resolution even when there was weak mode coupling. I believe that the proposed method will be a powerful tool for characterizing low-DMD or large-dispersion FMF, devices, and MDM transmission systems.

## 6. Summaries and conclusions

I have described the development of the FMCW method for characterizing SDM transmission with a view to realizing the effective maintenance and management of future optical fiber networks. Utilizing the reflection-type FMCW method (C-OFDR), I have proposed and demonstrated distributed measurements of differential delay and delay spread along SDM fibers including both FMF and coupled-MCF. Moreover, I have also proposed the high-resolution end-to-end measurement of the DMD of an FMF link by using the transmission-type FMCW method.

In chapter 2, as a basis for the distributed delay measurement that I proposed in chapter 3, I have described the fundamental characteristics of the Rayleigh backscattering signature measured with C-OFDR. I have clarified its dependence on the laser phase noise and fiber temperature/strain change. I have also proposed techniques for suppressing both laser phase noise and detector noise to improve the repeatability of the backscattering signature. By applying the techniques, I have demonstrated the long-range measurement of the backscattering signature and its spectral shift caused by temperature changes along an SMF.

In chapter 3, I have proposed a nondestructive method for characterizing the accumulated link DMD along an FMF for the first time. This method was realized by utilizing the Rayleigh backscattering signature and its spectral shift described in chapter 2. I have demonstrated distributed DMD measurements along different kinds of TMF links with 20-ps accuracy and 40-m resolution by using the backscattering spectral shifts caused by natural and random environmental disturbances, and the results agreed well with those obtained with a destructive method and by calculation.

In chapter 4, focusing on the characterization of SC-MCF, I have proposed the first SMD distribution measurement method. The SMD distribution was characterized by auto-correlating the Rayleigh backscattering amplitude measured with C-OFDR. The concept of this method was inspired by the randomness of the backscattering waveform similar to a low-coherence signal, and the auto-correlation analysis was based on the low-coherence interferometric method. I have also described an FSAV technique for suppressing the correlation fluctuation and improving the measurement accuracy. The SMD distribution measurements were demonstrated with several kinds of SC-MCFs, and the results were in good agreement with an estimation obtained with conventional end-to-end measurements. After the FSAV, I achieved a measurement with a delay accuracy of a few ps and a spatial resolution of 6 m over a 4 km range.

In chapter 5, I described the high-resolution DMD measurement of an FMF link with phase signals obtained with the transmission-type FMCW method as a reference. While the conventional FMCW method used a Fourier-transform for spectral analysis, where the resolution is limited by the optical frequency sweep range, the proposed method overcame this limitation by analyzing the frequency directly from the temporal phase signal. Although the proposed method was based on the assumption that mode coupling could be ignored, the mode coupling effect could be mitigated by averaging multiple phase signals with different detection timings. By using the phase-referencing and its averaging method, I have achieved DMD measurement with fs-order resolution, which was 80 times better than the conventional method.

As summarized above, in this thesis I have proposed and demonstrated three new kinds of SDM characterization methods, namely the measurement of DMD distribution, SMD distribution, and end-to-end DMD with a high resolution. The feature of these methods is that the main techniques are performed with signal processing after

## *6. Summaries and conclusions*

acquiring the FMCW signals. Therefore, we can easily expand and improve the capability of the FMCW method while maintaining its simple configuration. I hope these methods will assist the future maintenance and management of SDM networks.





# Appendix

## Appendix A. C-OFDR beat signal with one-dimensional scatter model

In this appendix, I describe the deviation of the C-OFDR beat signal used in chapter 2 in detail.

The complex amplitude of frequency-swept light,  $E(t)$ , is given by

$$E(t) = E_0 \exp \left\{ j \left[ 2\pi \left( \nu_0 + \frac{\gamma}{2} t \right) t + \theta(t) \right] \right\}, \quad (\text{A-1})$$

where  $\nu_0$  is the initial optical frequency,  $\gamma$  is the sweep rate, and  $\theta(t)$  is the phase noise. Since the reflected or backscattered light can be treated as a time-delayed replica of  $E(t)$ , the back-propagated light, which is reflected at position  $z_R$ ,  $E_R(t)$ , can be described as

$$\begin{aligned} E_R(t) &= \sqrt{R} E(t - \tau_R) \\ &= \sqrt{R} E_0 \exp \left\{ j \left[ 2\pi \left( \nu_0 + \frac{\gamma}{2} t \right) t - 2\pi(\nu_0 + \gamma)\tau_R + \pi\gamma\tau_R^2 + \theta(t - \tau_R) \right] \right\}, \end{aligned} \quad (\text{A-2})$$

where  $R$  denotes the reflectivity at  $z_R$ .  $\tau_R$  is the round-trip delay, which is related to  $z_R$  with

$$\tau_R = 2nz_R / c, \quad (\text{A-3})$$

where  $n$  is the refractive index, and  $c$  is the speed of light in a vacuum. In Eq. (A-2),  $\tau_R^2$  can be neglected because it is much smaller than the other terms. With the one-dimensional scatter model illustrated in Fig. 2-2, the backscattered light  $E_S(t)$  can be described as a superposition of multiple random reflections,

$$E_S(t) = \sum_{i=1}^M a_{R,i} \exp \left\{ j \left[ 2\pi \left( \nu_0 + \frac{\gamma}{2} t \right) t - 2\pi(\nu_0 + \gamma) \tau_{R,i} + \theta(t - \tau_{R,i}) \right] \right\}, \quad (\text{A-4})$$

with

$$\tau_{R,i} = 2nz_{R,i} / c, \quad (\text{A-5})$$

where  $M$  is the number of scatterers in the fiber,  $a_{R,i}$  is the  $i$ th scatter amplitude, and  $z_{R,i}$  is the position of the  $i$ th scatterer. By mixing the backscattered light with the local light, the beat signal  $I_R(t)$  is represented as

$$\begin{aligned} I_R(t) &= |E(t) + E_S(t)|^2 \\ &= E_0^2 + \sum_{i=1}^M a_{R,i}^2 + \sum_{i=1}^M E_0 a_{R,i} \cos[2\pi(\nu_0 + \gamma) \tau_{R,i} + \theta(t) - \theta(t - \tau_{R,i})] \\ &\quad + 2 \sum_{i=1}^M \sum_{j=i+1}^M a_{R,i} a_{R,j} \cos[2\pi(\nu_0 + \gamma)(\tau_{R,j} - \tau_{R,i}) + \theta(t - \tau_{R,j}) - \theta(t - \tau_{R,i})]. \quad (\text{A-6}) \end{aligned}$$

Since the backscattered light is very weak compared with the local light ( $a_{R,i} \ll E_0$ ), the fourth term can be neglected. By taking only the AC part into account, Eq. (A-6) can be approximated as

$$I_R(t) \propto \sum_{i=1}^M a_{R,i} \cos[2\pi(\nu_0 + \gamma) \tau_{R,i} + \theta(t) - \theta(t - \tau_{R,i})], \quad (\text{A-7})$$

which is equivalent to Eq. (2-1) in chapter 2.

## Appendix B. Auto-correlation of Rayleigh backscattering amplitude in coupled multicore fiber

In this appendix, I describe the detailed calculation of the auto-correlation of the Rayleigh backscattering amplitude in the SC-MCF used in chapter 4.

With the backscattering amplitude  $\tilde{\varepsilon}(\tau)$  described in Eq. (4-2), its auto-correlation is calculated as

$$\begin{aligned}
R(\tau') &= \int \tilde{\varepsilon}(\tau) \tilde{\varepsilon}^*(\tau + \tau') d\tau \\
&= \int \left[ \sum_m e^{\frac{(\Delta\tau_m)^2}{(\Delta\tau)^2}} e^{j\Delta\theta(\Delta\tau_m)} \varepsilon(\tau - \Delta\tau_m) \right] \left[ \sum_m e^{\frac{(\Delta\tau_m)^2}{(\Delta\tau)^2}} e^{-j\Delta\theta(\Delta\tau_m)} \varepsilon^*(\tau - \Delta\tau_m + \tau') \right] d\tau \\
&= \sum_m e^{\frac{2(\Delta\tau_m)^2}{(\Delta\tau)^2}} \int \varepsilon(\tau - \Delta\tau_m) \varepsilon^*(\tau - \Delta\tau_m + \tau') d\tau \\
&\quad + \sum_m \sum_{n \neq m} e^{\frac{(\Delta\tau_m)^2 + (\Delta\tau_n)^2}{(\Delta\tau)^2}} e^{j[\Delta\theta(\Delta\tau_m) - \Delta\theta(\Delta\tau_n)]} \int \varepsilon(\tau - \Delta\tau_m) \varepsilon^*(\tau - \Delta\tau_n + \tau') d\tau, \quad (\text{B-1})
\end{aligned}$$

where  $\varepsilon(\tau)$  is the complex backscattering amplitude without taking mode coupling into account, and  $\Delta\tau_m$  and  $\Delta\theta(\Delta\tau_m)$ , respectively, are the relative delay and random phase component of the  $m$ th backscattering replica generated by mode coupling, and  $\Delta\tau$  is the SMD. Since  $\varepsilon(\tau)$  fluctuates randomly along the delay time due to the interference between backscattered lights, we assume the following relationship:

$$\int \varepsilon(\tau - \Delta\tau_m) \varepsilon^*(\tau - \Delta\tau_m + \tau') d\tau = \delta_{\tau', 0}, \quad (\text{B-2})$$

$$\int \varepsilon(\tau - \Delta\tau_m) \varepsilon^*(\tau - \Delta\tau_n + \tau') d\tau = \delta_{\Delta\tau_n, \Delta\tau_m + \tau'}. \quad (\text{B-3})$$

By substituting Eq. (B-2) and (B-3) into (B-1), the auto-correlation can be obtained as

$$\begin{aligned}
R(\tau') &= \delta_{\tau',0} \sum_m e^{\frac{2(\Delta\tau_m)^2}{(\Delta\tau)^2}} + \sum_m \sum_{n \neq m} e^{\frac{(\Delta\tau_m)^2 + (\Delta\tau_n)^2}{(\Delta\tau)^2}} e^{j[\Delta\theta(\Delta\tau_m) - \Delta\theta(\Delta\tau_n)]} \delta_{\Delta\tau_n, \Delta\tau_m + \tau'} \\
&= \delta_{\tau',0} \sum_m e^{\frac{2(\Delta\tau_m)^2}{(\Delta\tau)^2}} + e^{\frac{\tau'^2}{2(\Delta\tau)^2}} \sum_m e^{\frac{2(\Delta\tau_m + \tau'/2)}{(\Delta\tau)^2}} e^{j[\Delta\theta(\Delta\tau_m) - \Delta\theta(\Delta\tau_m + \tau')]}, \quad (\text{B-4})
\end{aligned}$$

which is equivalent to Eq. (4-3) in chapter 4.

## Appendix C. FMCW phase signal with mode coupling

In this appendix, I describe the calculation of the FMCW phase signal in detail taking mode coupling into account.

By using the FMCW beat signal of the  $m$ th mode  $I_m(t)$  described in Eq. (5-6) in chapter 5, its phase component  $\theta_m(t)$  can be calculated by

$$\begin{aligned}\theta'_m(t) &= \tan^{-1} \frac{H[I_m(t)]}{I_m(t)} \\ &= \tan^{-1} \frac{\sin \phi_m(t) + \sum_{i \neq m} \alpha_i \sin \phi_i(t)}{\cos \phi_m(t) + \sum_{i \neq m} \alpha_i \cos \phi_i(t)},\end{aligned}\quad (\text{C-1})$$

where  $H[I_m(t)]$  is the Hilbert transform of  $I_m(t)$ , and  $\alpha_i$  is the relative amplitude of the  $i$ th coupled mode with respect to the  $m$ th mode. Equation (C-1) can be schematically represented in a complex plane as a phasor sum, which is shown in Fig. C-1. In this illustration, the real and imaginary parts correspond to the beat signal and its Hilbert transform, respectively. When  $\theta_m(t)$  can be described as

$$\theta'_m(t) = \phi_m(t) + \varphi(t), \quad (\text{C-2})$$

$\varphi(t)$  can be obtained with the following equations:

$$\tan[\phi_m(t) + \varphi(t)] = \frac{\tan \phi_m(t) + \tan \varphi(t)}{1 - \tan \phi_m(t) \tan \varphi(t)} = \frac{\sin \phi_m(t) + \sum_{i \neq m} \alpha_i \sin \phi_i(t)}{\cos \phi_m(t) + \sum_{i \neq m} \alpha_i \cos \phi_i(t)}, \quad (\text{C-3})$$

$$\begin{aligned}& [\tan \phi_m(t) + \tan \varphi(t)] \left[ \cos \phi_m(t) + \sum_{i \neq m} \alpha_i \cos \phi_i(t) \right] \\ &= [1 - \tan \phi_m(t) \tan \varphi(t)] \left[ \sin \phi_m(t) + \sum_{i \neq m} \alpha_i \sin \phi_i(t) \right],\end{aligned}\quad (\text{C-4})$$

$$\begin{aligned} \tan \varphi(t) & \left[ 1 + \cos \phi_m(t) \sum_{i \neq m} \alpha_i \cos \phi_i(t) + \sin \phi_m(t) \sum_{i \neq m} \alpha_i \sin \phi_i(t) \right] \\ & = \cos \phi_m(t) \sum_{i \neq m} \alpha_i \sin \phi_i(t) - \sin \phi_m(t) \sum_{i \neq m} \alpha_i \cos \phi_i(t), \end{aligned} \quad (\text{C-5})$$

$$\tan \varphi(t) = \frac{\sum_{i \neq m} \alpha_i \sin[\phi_i(t) - \phi_m(t)]}{1 + \sum_{i \neq m} \alpha_i \cos[\phi_i(t) - \phi_m(t)]}. \quad (\text{C-6})$$

Therefore,  $\theta_m(t)$  can be described as

$$\theta'_m(t) = \phi_m(t) + \tan^{-1} \frac{\sum_{i \neq m} \alpha_i \sin[\phi_i(t) - \phi_m(t)]}{1 + \sum_{i \neq m} \alpha_i \cos[\phi_i(t) - \phi_m(t)]}, \quad (\text{C-7})$$

which is also illustrated in Fig. C-2. Equation (C-7) is equivalent to Eq. (5-8) in chapter 5.

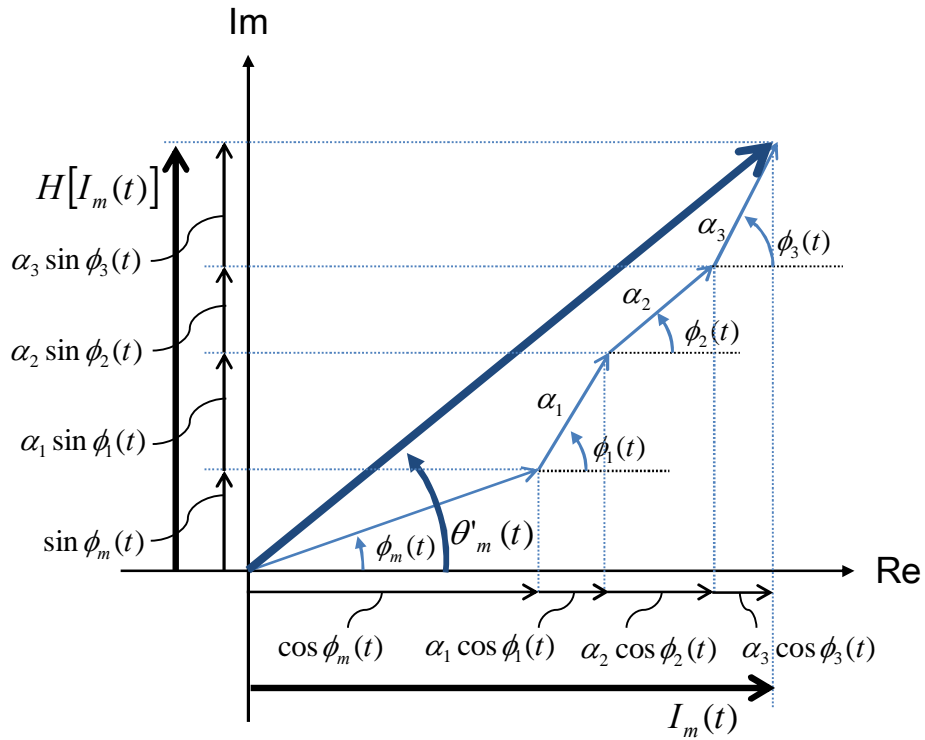


Figure C-1. Schematic diagram of Eq. (C-1).

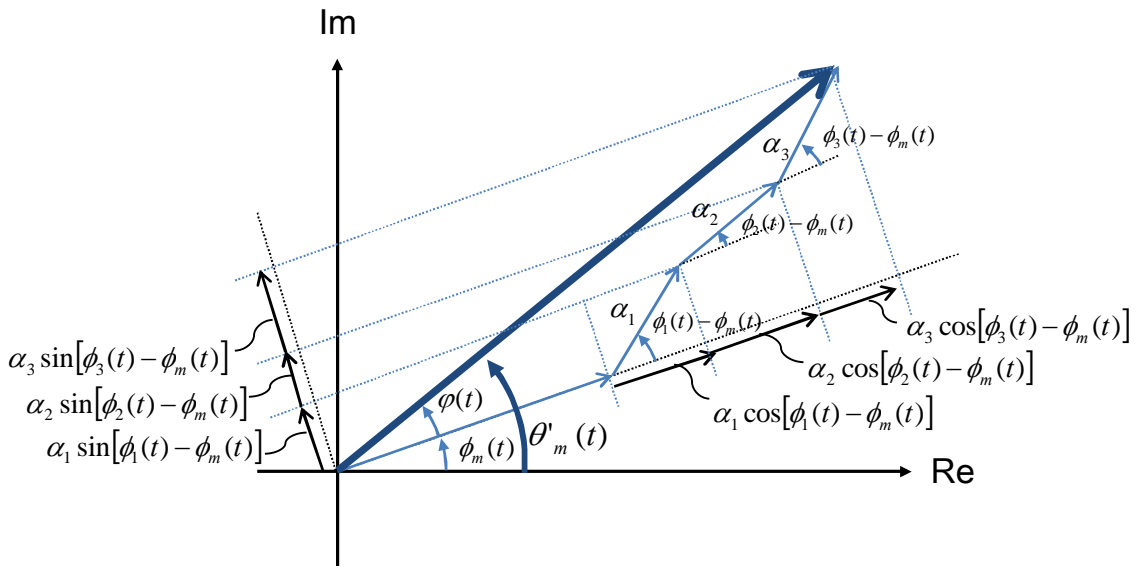


Figure C-2. Schematic diagram of Eq. (C-7).





# References

## Chapter 1.

- [1-1] J. Yamada, S. Machida, and T. Kimura, "2 Gbit/s optical transmission experiments at 1.3  $\mu$ m with 44 km single-mode fibre," *Electron. Lett.* **17**(13) 479-480 (1981).
- [1-2] H. Shinohara, "Broadband access in Japan: rapidly growing FTTH market," *IEEE Communications Magazine* **43**(9), 72-78 (2005).
- [1-3] Ministry of Internal Affairs and Communications [Online]. Available: [http://www.soumu.go.jp/menu\\_news/s-news/01kiban04\\_02000128.html](http://www.soumu.go.jp/menu_news/s-news/01kiban04_02000128.html)
- [1-4] T. Sakamoto, T. Matsui, S. Aozasa, K. Tsujikawa, and K. Nakajima, "World's Highest Density Optical Fiber for Space Division Multiplexing with Deployable Reliability," *NTT Technical Review* **15**(2) (2017). Available: <https://www.ntt-review.jp/archive/ntttechnical.php?contents=ntr201702ra2.html>
- [1-5] Y. Miyamoto and R. Kawamura, "Space Division Multiplexing Optical Transmission Technology to Support the Evolution of High-capacity Optical Transport Networks," *NTT Technical Review* **15**(6) (2017). Available: <https://www.ntt-review.jp/archive/ntttechnical.php?contents=ntr201706fa1.html>
- [1-6] N. S. Bergano and C. R. Davidson, "Wavelength division multiplexing in long-haul transmission systems," *J. Lightw. Technol.* **14**(6), 1299-1308 (1996).
- [1-7] K. Kikuchi, "Phase-diversity homodyne detection of multilevel optical modulation with digital carrier phase estimation," *IEEE J. Selected Topics in Quantum Electronics* **12**(4), 563-570, (2006).
- [1-8] D. P. Hand and P. St. J. Russell, "Solitary thermal shock waves and optical

- damage in optical fibers: the fiber fuse, *Opt. Lett.* **13**(9), 767-769 (1988).
- [1-9] R. -J. Essiambre, G. Kramer, P. J. Winzer, G. J. Foschini, and B. Goebel, *Capacity limits of optical fiber networks*, *J. Lightw. Technol.* **28**(4), 662-701 (2010).
- [1-10] A. Sano, T. Kobayashi, S. Yamanaka, A. Matsuura, H. Kawakami, Y. Miyamoto, K. Ishihara, and H. Masuda, *102.3-Tb/s (224 x 548-Gb/s) C- and Extended L-band All-Raman Transmission over 240 km Using PDM-64QAM Single Carrier FDM with Digital Pilot Tone*, in *Technical Digest of the Optical Fiber Communication Conference (OFC2012)*, paper PDP5C.3 (2012).
- [1-11] S. Berdagué and P. Facq, *Mode division multiplexing in optical fibers*, *Appl. Opt.* **21**(11), 1950-1955 (1982).
- [1-12] S. Randel, R. Ryf, A. Sierra, P. J. Winzer, A. H. Gnauck, C. A. Bolle, R. -J. Essiambre, D. W. Peckham, A. McCurdy, and R. Lingle, *6x56-Gb/s mode-division multiplexed transmission over 33-km few-mode fiber enabled by 6x6 MIMO equalization*, *Opt. Express* **19**(17), 16697-16707 (2011).
- [1-13] S. Inao, T. Sato, S. Sentui, T. Kuroha, and Y. Nishimura, *Multicore Optical Fiber*, in *Technical Digest of the Optical Fiber Communication Conference (OFC1979)*, paper WB1 (1979).
- [1-14] R. Ryf, N. K. Fontaine, B. Guan, R. -J. Essiambre, S. Randel, A. H. Gnauck, S. Chandrasekhar, A. Adamiecki, G. Raybon, B. Ercan, R. P. Scott, S. J. Ben Yoo, T. Hayashi, T. Nagashima, and T. Sasaki, *1705-km Transmission over Coupled-Core Fibre Supporting 6 Spatial Modes*, in *Proceedings of the 40th European Conference on Optical Communication (ECOC2014)*, paper PD.3.2 (2014).
- [1-15] T. Sakamoto, T. Mori, M. Wada, T. Yamamoto, F. Yamamoto, and K. Nakajima,

## References

- Strongly-coupled multi-core fiber and its optical characteristics for MIMO transmission systems, *Optical Fiber Technology* **35**, 8-18 (2017).
- [1-16] D. Soma, Y. Wakayama, S. Beppu, S. Sumita, T. Tsuritani, T. Hayashi, T. Nagashima, M. Suzuki, H. Takahashi, K. Igarashi, I. Morita, and M. Suzuki, 10.16 Peta-bit/s Dense SDM/WDM transmission over Low-DMD 6-Mode 19-Core Fibre across C+L Band, in *Proceedings of the 43rd European Conference on Optical Communication (ECOC2017)*, Th.PDP.A.1 (2017).
- [1-17] D. Gloge, Weakly Guiding Fibers, *Appl. Opt.* **10**(10), 2252-2258 (1971)
- [1-18] M. Salsi, C. Koebele, D. Sperti, P. Tran, P. Brindel, H. Mardoyan, S. Bigo, A. Boutin, F. Verluise, P. Sillard, M. Bigot-Astruc, L. Provost, F. Cerou, and G. Charlet, Transmission at 2x100Gb/s, over Two Modes of 40km-long Prototype Few-Mode Fiber, using LCOS based Mode Multiplexer and Demultiplexer, in *Technical Digest of the Optical Fiber Communication Conference (OFC2011)*, paper PDPB9 (2011).
- [1-19] N. Hanzawa, K. Saitoh, T. Sakamoto, T. Matsui, K. Tsujikawa, M. Koshiba, and F. Yamamoto, Two-mode PLC-based mode multi/demultiplexer for mode and wavelength division multiplexed transmission, *Opt. Express* **21**(22), 25752-25760 (2013).
- [1-20] E. Ip, G. Milione, Y. Huang, and T. Wang, Impact of Mode-Dependent Loss on Long-Haul Transmission Systems using Few-Mode Fibers, in *Technical Digest of the Optical Fiber Communication Conference (OFC2016)*, paper W41.4 (2016).
- [1-21] B. Inan, B. Spinnler, F. Ferreira, D. Borne, A. Lobato, S. Adhikari, V. Sleiffer, M. Kushnerov, N. Hanik, and S. Jansen, DSP complexity of mode-division multiplexed receivers, *Opt. Express* **20**(10), 10859-10869 (2012).

- [1-22] T. Sakamoto, T. Mori, T. Yamamoto, and S. Tomita, "Differential Mode Delay Managed Transmission Line for Wide-band WDM-MIMO System," in *Technical Digest of the Optical Fiber Communication Conference (OFC2012)*, paper OM2D.1.
- [1-23] Y. Sasaki, K. Hirakawa, I. Ishida, S. Matsuo, and K. Aikawa, "Evaluation of Inter-Core Skew in an Uncoupled Multicore Fibre," in *Proceedings of the 43rd European Conference on Optical Communication (ECOC2017)*, paper W.1.B.4 (2017).
- [1-24] S. Aozasa, T. Sakamoto, S. Nozoe, Y. Sagae, M. Wada, T. Mori, K. Tsujikawa, T. Yamamoto, and K. Nakajima, "Bending Radius Dependence of Spatial Mode Dispersion in Randomly Coupled Multi-Core Fiber," in *Technical Digest of the Optical Fiber Communication Conference (OFC2017)*, paper Th1H.4 (2017).
- [1-25] TIA-455-220-A, "Differential Mode Delay Measurement of Multimode Fiber in the Time Domain," *Telecommunication Industry Association* (2003).
- [1-26] T.-J. Ahn and D. Y. Kim, "High-Resolution Differential Mode Delay Measurement for a Multimode Optical Fiber Using a Modified Optical Frequency Domain Reflectometer," *Opt. Express* **13**(20), 8256-8262 (2005).
- [1-27] T.-J. Ahn, S. Moon, Y. Youk, Y. Jung, K. Oh, and D.Y. Kim, "New Optical Frequency Domain Differential Mode Delay Measurement Method for a Multimode Optical Fiber," *Opt. Express* **13**(11), 4005-4011 (2005).
- [1-28] N. K. Fontaine, R. Ryf, M. A. Mestre, B. Guan, X. Palou, S. Randel, Y. Sun, L. Grüner-Nielsen, R. V. Jensen, and R. Lingle Jr., "Characterization of Space-Division Multiplexing Systems using a Swept-Wavelength Interferometer," in *Technical Digest of the Optical Fiber Communication Conference (OFC2013)*, paper OW1K.2 (2013).

## References

- [1-29] W. Eickhoff and R. Ulrich, "Optical frequency domain reflectometry in single-mode fiber," *Appl. Phys. Lett.* **39**, 693-695 (1981).
- [1-30] U. Glombitza and E. Brinkmeyer, "Coherent frequency-domain reflectometry for characterization of single-mode integrated-optical waveguides," *J. Lightw. Technol.* **11**(8), 1377-1384 (1993).
- [1-31] L. Grüner-Nielsen, Y. Sun, J. W. Nicholson, D. Jakobsen, K. G. Jespersen, R. Lingle Jr., and B. Pálsdóttir, "Few Mode Transmission Fiber with Low DGD, Low Mode Coupling, and Low Loss," *J. Lightw. Technol.* **30**(23), 3693-3698 (2012).
- [1-32] K. Sato, R. Maruyama, N. Kuwaki, S. Matsuo, and M. Ohashi, "Optimized Graded Index Two-Mode Optical Fiber with Low DMD, Large  $A_{\text{eff}}$  and Low Bending Loss," *Opt. Express* **21**(14), 16231-16238 (2013).

## Chapter 2.

- [2-1] M. Barnoski and S. Jensen, "Fiber waveguides: a novel technique for investigating attenuation characteristics," *Appl. Opt.* **15**(9), 2112-2115 (1976).
- [2-2] W. Eickhoff and R. Ulrich, "Optical frequency domain reflectometry in single-mode fiber," *Appl. Phys. Lett.* **39**, 693-695 (1981).
- [2-3] K. Takada, I. Yokohama, K. Chida, and J. Noda, "New measurement system for fault location in optical waveguide devices based on an interferometric technique," *Appl. Opt.* **26**(9), 1603-1606 (1987).
- [2-4] M. Frogatt, B. Soller, D. Gifford, and M. Wolfe, "Correlation and keying of Rayleigh scatter for loss and temperature sensing in parallel optical networks," in *Technical Digest of the Optical Fiber Communication Conference (OFC2004)*, paper PD17 (2004).

- [2-5] Y. Koyamada, Y. Eda, S. Hirose, S. Nakamura, and K. Hogari, "Novel fiber-optic distributed strain and temperature sensor with very high resolution," *IEICE Trans. Commun.* **E89-B(5)**, 1722-1725 (2006).
- [2-6] D. Gifford, S. Kreger, A. Sang, M. Froggatt, R. Duncan, M. Wolfe, and B. Soller, "Swept-wavelength interferometric interrogation of fiber Rayleigh scatter for distributed sensing applications," *Proc. SPIE 6770, Fiber Optic Sensors and Applications V*, 67700F (2007).
- [2-7] E. Lally, M. Reaves, E. Horrell, S. Klute, and M. Froggatt, "Fiber optic shape sensing for monitoring of flexible structures," *Proc. SPIE 8345, Sensors and Smart Structures Technologies for Civil, Mechanical, and Aerospace Systems 2012*, 83452Y (2012).
- [2-8] P. Healey, "Fading in heterodyne OTDR," *Electron. Lett.* **20(1)**, 30-32 (1984).
- [2-9] U. Glombitza and E. Brinkmeyer, "Coherent frequency-domain reflectometry for characterization of single-mode integrated-optical waveguides," *J. Lightw. Technol.* **11(8)**, 1377-1384 (1993).
- [2-10] S. Venkatesh and W. Sorin, "Phase noise considerations in coherent optical FMCW reflectometry," *J. Lightw. Technol.* **11(10)**, 1694-1700 (1993).
- [2-11] S. Ohno, D. Iida, K. Toge, and T. Manabe, "Long-range C-OFDR measurement of Rayleigh scatter signature of fiber beyond laser coherence length," in *Technical Digest of the Optical Fiber Communication Conference (OFC2016)*, paper W4F.4 (2016).
- [2-12] Kersey, M. Davis, H. Patrick, M. LeBlanc, K. Koo, C. Askins, M. Putnam, and E. Friebele, "Fiber grating sensors," *J. Lightw. Technol.* **15(8)**, 1442-1463 (1997).
- [2-13] M. Inoue, F. Ito, X. Fan, and Y. Koshikiya, "Very long range quasi-Fourier

## References

- spectroscopy for narrowband lasers,ö *Opt. Express* **20**(26), B566-B573 (2012).
- [2-14] Y. Koshikiya, X. Fan, and F. Ito, öLong-range and cm-level spatial resolution measurement using coherent optical frequency domain reflectometry with SSB-SC modulator and narrow linewidth fiber laser,ö *J. Lightw. Technol.* **26**(18), 3287-3294 (2008).
- [2-15] X. Fan, Y. Koshikiya, and F. Ito, öPhase-noise-compensated optical frequency domain reflectometry with measurement range beyond laser coherence length realized using concatenative reference method,ö *Opt. Lett.* **32**(22), 3227-3229 (2007).
- [2-16] F. Ito, X. Fan, and Y. Koshikiya, öLong-range coherent OFDR with light source phase noise compensation,ö *J. Lightw. Technol.* **30**(8), 1015-1024 (2012).

## Chapter 3.

- [3-1] R. Ryf, S. Randel, A. H. Gnauck, C. Bolle, A. Sierra, S. Mumtaz, M. Esmaelpour, E. C. Burrows, R.-J. Essiambre, P. J. Winzer, D. W. Peckham, A. H. McCurdy, and R. Lingle Jr., öMode-Division Multiplexing Over 96 km of Few-Mode Fiber Using Coherent 6 x 6 MIMO Processing,ö *J. Lightw. Technol.* **30**(4), 521-531 (2012).
- [3-2] TIA-455-220-A, öDifferential Mode Delay Measurement of Multimode Fiber in the Time Domain,ö *Telecommunication Industry Association* (2003).
- [3-3] T.-J. Ahn et al., öNew optical frequency domain differential mode delay measurement method for a multimode optical fiber,ö *Opt. Express* **13**(11), 4005-4011 (2005).
- [3-4] J. Y. Lee et al., öFourier-domain low-coherence interferometry for differential mode delay analysis of an optical fiber,ö *Opt. Lett.* **31**(16), 2396-2398 (2006).



- [3-5] F. Ye et al., "Differential mode delay management in spliced multimode fiber transmission systems," in *Technical Digest of the Optical Fiber Communication Conference (OFC2013)*, paper OM3B.3. (2013).
- [3-6] D. K. Gifford et al., "Swept-wavelength interferometric interrogation of fiber Rayleigh scatter for distributed sensing applications," *Proc. SPIE 6770, Fiber Optic Sensors and Applications V*, 67700F (2007).
- [3-7] X. Fan et al., "Phase-noise-compensated optical frequency domain reflectometry with measurement range beyond laser coherence length realized using concatenative reference method," *Opt. Lett.* **32**(22), 3227-3229 (2007).
- [3-8] N. Hanzawa et al., "Two-mode PLC-based mode multi/demultiplexer for mode and wavelength division multiplexed transmission," *Opt. Express* **21**(22), 25752-25760 (2013).
- [3-9] S. Ohno et al., "Long-range measurement of Rayleigh scatter signature beyond laser coherence length based on coherent optical frequency domain reflectometry," *Opt. Express* **24**(17), 19651-19660 (2016).

## Chapter 4.

- [4-1] R. Ryf, N. K. Fontaine, B. Guan, R. -J. Essiambre, S. Randel, A. H. Gnauck, S. Chandrasekhar, A. Adamiecki, G. Raybon, B. Ercan, R. P. Scott, S. J. Ben Yoo, T. Hayashi, T. Nagashima, and T. Sasaki, "1705-km Transmission over Coupled-Core Fibre Supporting 6 Spatial Modes," in *Proceedings of the 40th European Conference on Optical Communication (ECOC2014)*, paper PD.3.2 (2014).
- [4-2] T. Sakamoto, T. Mori, M. Wada, T. Yamamoto, F. Yamamoto, and K. Nakajima, "Fiber Twisting- and Bending-Induced Adiabatic/Nonadiabatic Super-Mode

## References

- Transition in Coupled Multicore Fiber, *J. Lightw. Technol.* **34**(4), 1228-1237 (2016).
- [4-3] T. Hayashi, "Coupled Multicore Fiber for Space-Division Multiplexed Transmission," *Proc. SPIE 10130, Next-Generation Optical Communication: Components, Sub-Systems, and Systems VI*, 1013003 (2017).
- [4-4] S. Aozasa, T. Sakamoto, S. Nozoe, Y. Sagae, M. Wada, T. Mori, K. Tsujikawa, T. Yamamoto, and K. Nakajima, "Bending Radius Dependence of Spatial Mode Dispersion in Randomly Coupled Multi-Core Fiber," in *Technical Digest of the Optical Fiber Communication Conference (OFC2017)*, paper Th1H.4 (2017).
- [4-5] P. Healey, "Fading in Heterodyne OTDR," *Electron. Lett.* **20**(1), 30-32 (1984).
- [4-6] M. Froggatt, B. Soller, D. Gifford, and M. Wolfe, "Correlation and Keying of Rayleigh Scatter for Loss and Temperature Sensing in Parallel Optical Networks," in *Technical Digest of the Optical Fiber Communication Conference (OFC2004)*, paper PDP17 (2004).
- [4-7] S. Ohno, D. Iida, K. Toge, and T. Manabe, "Long-Range Measurement of Rayleigh Scatter Signature beyond Laser Coherence Length based on Coherent Optical Frequency Domain Reflectometry," *Opt. Express* **24**(17), 19651-19660 (2016).
- [4-8] U. Glombitza and E. Brinkmeyer, "Coherent Frequency-Domain Reflectometry for Characterization of Single-Mode Integrated-Optical Waveguides," *J. Lightw. Technol.* **11**(8), 1377-1384 (1993).
- [4-9] S. Ohno, D. Iida, K. Toge, and T. Manabe, "Distributed Spatial Mode Dispersion Measurement Along Strongly Coupled Multicore Fibre with C-OFDR," in *Proceedings of the 43rd European Conference on Optical Communication (ECOC2017)*, paper Tu.1.A.5 (2017).

- [4-10] ITU-T Recommendation G.650.2, "Definitions and test methods for statistical and non-linear related attributes of single-mode fibre and cable" (2015).
- [4-11] N. Gisin, J. -P. Von der Weid, and J. -P. Pellaux, "Polarization Mode Dispersion of Short and Long Single-Mode Fibers," *J. Lightwave Technol.* **9**(7), 821-827 (1991).
- [4-12] K. Shimizu, T. Horiguchi, and Y. Koyamada, "Characteristics and reduction of coherent fading noise in Rayleigh backscattering measurement for optical fibers and components," *J. Lightw. Technol.* **10**(7), 982-987 (1992).
- [4-13] X. Fan, Y. Koshikiya, and F. Ito, "Phase-Noise-Compensated Optical Frequency Domain Reflectometry with Measurement Range beyond Laser Coherence Length Realized using Concatenative Reference Method," *Opt. Lett.* **32**(22), 3227-3229 (2007).
- [4-14] F. Ito, X. Fan, and Y. Koshikiya, "Long-Range Coherent OFDR With Light Source Phase Noise Compensation," *J. Lightwave Technol.* **30**(8), 1015-1024 (2012).

## Chapter 5.

- [5-1] L. Grüner-Nielsen, Y. Sun, J. W. Nicholson, D. Jakobsen, K. G. Jespersen, R. Lingle Jr., and B. Pálsdóttir, "Few Mode Transmission Fiber with Low DGD, Low Mode Coupling, and Low Loss," *J. Lightw. Technol.* **30**(23), 3693-3698 (2012).
- [5-2] K. Sato, R. Maruyama, N. Kuwaki, S. Matsuo, and M. Ohashi, "Optimized Graded Index Two-Mode Optical Fiber with Low DMD, Large  $A_{\text{eff}}$  and Low Bending Loss," *Opt. Express* **21**(14), 16231-16238 (2013).
- [5-3] T. Sakamoto, T. Mori, T. Yamamoto, and S. Tomita, "Differential Mode Delay

## References

- Managed Transmission Line for Wide-band WDM-MIMO System,ö in *Technical Digest of the Optical Fiber Communication Conference (OFC2012)*, paper OM2D.1 (2012).
- [5-4] TIA-455-220-A, Differential Mode Delay Measurement of Multimode Fiber in the Time Domain, *Telecommunication Industry Association* (2003).
- [5-5] J. Y. Lee and D. Y. Kim, öDetermination of the Differential Mode Delay of a Multimode Fiber Using Fourier-Domain Intermodal Interference Analysis,ö *Opt. Express* **14**(20), 9016-9021 (2006).
- [5-6] T.-J. Ahn and D. Y. Kim, öHigh-Resolution Differential Mode Delay Measurement for a Multimode Optical Fiber Using a Modified Optical Frequency Domain Reflectometer,ö *Opt. Express* **13**(20), 8256-8262 (2005).
- [5-7] T.-J. Ahn, S. Moon, Y. Youk, Y. Jung, K. Oh, and D.Y. Kim, öNew Optical Frequency Domain Differential Mode Delay Measurement Method for a Multimode Optical Fiber,ö *Opt. Express* **13**(11), 4005-4011 (2005).
- [5-8] N. K. Fontaine, R. Ryf, M. A. Mestre, B. Guan, X. Palou, S. Randel, Y. Sun, L. Grüner-Nielsen, R. V. Jensen, and R. Lingle Jr., öCharacterization of Space-Division Multiplexing Systems using a Swept-Wavelength Interferometer,ö in *Technical Digest of the Optical Fiber Communication Conference (OFC2013)*, paper OW1K.2 (2013).
- [5-9] U. Glombitza and E. Brinkmeyer, öCoherent Frequency-Domain Reflectometry for Characterization of Single-Mode Integrated-Optical Waveguides,ö *J. Lightw. Technol.* **11**(8), 1377-1384 (1993).
- [5-10] Y. Koshikiya, X. Fan, F. Ito, Z. He, and K. Hotate, öHigh Resolution PNC-OFDR With Suppressed Fading Noise for Dispersive Media Measurement,ö *J. Lightw. Technol.* **31**(6), 866-873 (2013).

X. Fan, Y. Koshikiya, and F. Ito, "Phase-Noise-Compensated Optical Frequency Domain Reflectometry with Measurement Range Beyond Laser Coherence Length Realized Using Concatenative Reference Method," *Opt. Lett.* **32**(22), 3227-3229 (2007).

# List of figures

## Chapter 1.

Figure 1-1. Evolution of transmission capacities in commercial systems. ....	2
Figure 1-2. SDM fibers. ....	4
Figure 1-3. Optical intensity distribution of each LP mode. ....	5
Figure 1-4. Basic setup of impulse response measurement. ....	8
Figure 1-5. Basic setup of FMCW method. (a) Transmission and (b) reflection types. ...	8
Figure 1-6. Schematic diagram of measurement principle with FMCW method. ....	9
Figure 1-7. Study approaches in this thesis. ....	13
Figure 1-8. Thesis organization. ....	14

## Chapter 2.

Figure 2-1. Basic setup of C-OFDR. ....	20
Figure 2-2. One-dimensional scatter model. ....	20
Figure 2-3. Experimental setup of C-OFDR. ....	23
Figure 2-4. Cross-correlations of (a) complex scatter spectrum, (b) scatter power spectrum at each segment position. The segment size was 100 m. ....	25
Figure 2-5. (a) Scatter power spectra, (b) cross-correlation of the scatter power spectra at 40 km measured at 35.00 and 35.02 °C. In the cross-correlation, the spectrum at 35.00°C was used as reference data. The segment size was 25 m. Laser 1 with $L_c = 10$ km was used. ....	26
Figure 2-6. Temperature dependence of spectral shift of the scatter power spectrum measured at 40 km. The solid line is a linear least square fit. The segment	

size was 25 m. ....	27
Figure 2-7. Segment size dependence of the cross-correlation of the scatter power spectrum at 20 km. ....	29
Figure 2-8. Frequency sweep rate dependence of the cross-correlation of the scatter power spectrum at 20 km. ....	30
Figure 2-9. Averaging number dependence of the cross-correlation of the averaged scatter spectra measured with (a) Laser 1, (b) Laser 2. ....	32
Figure 2-10. Dependence of cross-correlation of averaged scatter spectra on segment position difference. ....	33
Figure 2-11. Fresnel reflection at the end of a 50-km long SMF. ....	33
Figure 2-12. Configuration of sensing fiber. ....	35
Figure 2-13. Spectral shift distribution of averaged scatter spectrum at each temperature in Section B. The spectrum at 30.5°C was used as reference data in the cross-correlation. ....	35

### Chapter 3.

Figure 3-1. Concept of proposed method. ....	39
Figure 3-2. Experimental C-OFDR setup. TLS: tunable laser source, BPD: balanced photodetector, AI: auxiliary interferometer, MI: main interferometer. ....	42
Figure 3-3. Configurations of FUTs and their accumulated link DMDs. (a) FUT-3.1, (b) FUT-3.2. ....	43
Figure 3-4. Spectral shift distribution of the scatter measured with (a), (b) FUT-3.1, (c), (d) FUT-3.2. ....	46
Figure 3-5. Accumulated link DMDs along (a) FUT-3.1, (b) FUT-3.2. ....	47

## Chapter 4.

Figure 4-1. Schematic diagram of proposed SMD measurement.....	53
Figure 4-2. Error factors in SMD measurement. ....	56
Figure 4-3. Schematic illustration of FSAV in SMD measurement.....	57
Figure 4-4. Setup for C-OFDR measurement. TLS: tunable laser source, SMF: single-mode fiber, BPD: balanced photodetector, BPF: band-pass filter.....	59
Figure 4-5. FUT cross-sections. ....	60
Figure 4-6. Setup for fixed analyzer method. PD: photodetector.....	60
Figure 4-7. Fourier transforms of output spectra measured with fixed analyzer method. .....	61
Figure 4-8. Auto-correlation fringes of backscattering amplitudes. ....	63
Figure 4-9. SMDs along (a) FUT-1, (b) FUT-2, (c) FUT-3. ....	64
Figure 4-10. SMDs along FUT-4.2 and 4.3. ....	65
Figure 4-11. Auto-correlation fringes obtained with/without FSAV. ....	67
Figure 4-12. SMD distribution with/without FSAV. ....	68
Figure 4-13. Averaging number dependence of SMD fluctuation.....	68

## Chapter 5.

Figure 5-1. Basic setup for conventional FMCW method. ....	74
Figure 5-2. Setup for phase-referencing FMCW method.....	76
Figure 5-3. Unwrapped phase difference of beat signals. ....	76
Figure 5-4. Schematic diagram of TSAV. ....	79
Figure 5-5. Experimental setup. TLS: tunable laser source, BPD: balanced photodetector.....	80
Figure 5-6. Fourier-transformed intensities of beat signals. (a) 58-m-SI-TMF, (b)	



57-m-GI-TMF, (c) without FUT..... 82

Figure 5-7. (a) Phase difference between beat signals of LP<sub>01</sub> and LP<sub>11</sub>, and (b) its  
 extended view around 9.9 ms. .... 83

Figure 5-8. Phase fluctuation from linear fitting. (a) 58 m-SI-TMF, (b) 57 m-GI-TMF.84

Figure 5-9. Fourier-transformed intensity of beat signals measured with offset-spliced  
 SI-TMF..... 85

Figure 5-10. (a) Phase difference between beat signals of LP<sub>01</sub> and LP<sub>11</sub> modes  
 measured with offset-spliced SI-TMF, and (b) its extended view around  
 0.25 ms. .... 87

Figure 5-11. Phase fluctuation from linear fitting measured with offset-spliced SI-TMF.  
 ..... 87

**Appendix**

Figure C-1. Schematic diagram of Eq. (C-1). .... 99

Figure C-2. Schematic diagram of Eq. (C-7). .... 99

## List of acronyms

SMF	single-mode fiber
FTTH	fiber-to-the-home
TDM	time division multiplexing
WDM	wavelength division multiplexing
SDM	space division multiplexing
MDM	mode division multiplexing
FMF	few-mode fiber
MCF	multicore fiber
LP	linearly polarized
MUX	multiplexer
DEMUX	demultiplexer
XT	crosstalk
MIMO	multiple-input multiple-output
FIR	finite impulse response
FUT	fiber under test
FMCW	frequency-modulated continuous wave
C-OFDR	coherent optical frequency-domain reflectometry
DMD	differential mode delay
C-OTDR	coherent optical time-domain reflectometry
SSB	single side band
RF	radio frequency
A/D	analog-to-digital

TMF	two-mode fiber
PLC	planer lightwave circuit
BPF	band-pass filter
SI	step-index
GI	graded-index
TLS	tunable laser source
BPD	balanced photodetector
AI	auxiliary interferometer
MI	main interferometer
SC-MCF	strongly coupled multicore fiber
SMD	spatial mode dispersion
PMD	polarization mode dispersion
FSAV	frequency-shift averaging
FI/FO	fan-in/fan-out
TSAV	time-shift averaging

# Acknowledgements

The work in this thesis has been greatly supported by a number of people, whom I would like to thank here.

First of all, I sincerely thank my former teacher, Prof. Satoru Adachi of the Division of Applied Physics, Faculty of Engineering, Hokkaido University, for his kind guidance and invaluable advice for this thesis. I also thank Prof. Kunimasa Saito of the Division of Media and Network Technologies, Graduate School of Information Science and Technology, and Prof. Yasunori Toda of the Division of Applied Physics, Faculty of Engineering, Hokkaido University, for their fruitful advice on this thesis. It is the greatest pleasure for me to be supported by the above respected professors to summarize this thesis.

This thesis is based on my research work conducted at NIPPON TELEGRAPH and TELEPHONE (NTT) Corporation. I express my sincere gratitude to Dr. Kazuyuki Shiraki and Dr. Fumihiko Ito, who were Project Manager and Group Leader at NTT Access Network Service Systems Laboratories, respectively, for giving me the opportunity to conduct this study. My special thanks go to Dr. Atsushi Nobiki, Project Manager of the Access Media Project, and Dr. Tetsuya Manabe, Group Leader of the Media and Equipment Management Group, for their continuous supports and encouragements. I also thank Mr. Noriyuki Araki, Dr. Kunihiro Toge, Dr. Daisuke Iida, Mr. Tatsuya Okamoto, Mr. Hiroshi Takahashi, Mr. Tomokazu Oda, and Mr. Yoshifumi Wakisaka, who are research members of the Media and Equipment Management Group, for cooperating with fruitful discussions. Especially, my deepest thanks must go to Dr. Manabe, Dr. Toge and Dr. Iida, who have continuously provided powerful

## *Acknowledgements*

encouragements throughout this work. My special thanks also go to Dr. Shin-ichi Aozasa, Dr. Taiji Sakamoto, and Ms. Saki Nozoe, for helping my experiments with their multicore fibers and mode multiplexers. Finally, I express my deep gratitude to Dr. Yusuke Koshikiya, Dr. Takashi Matsui, Mr. Masaki Wada, Mr. Yuto Sagae, Ms. Yoko Yamashita, and all of my colleagues, who have supported my company life with their heartwarming encouragements and kindnesses.

May 2018

Shingo Ohno

# List of publications and awards

## Papers related to this thesis

1. Shingo Ohno, Daisuke Iida, Kunihiro Toge, Tetsuya Manabe, "Long-range measurement of Rayleigh scatter signature beyond laser coherence length based on coherent optical frequency domain reflectometry," *Optics Express* **24**(17), 19651-19660 (2016).
2. Shingo Ohno, Kunihiro Toge, Daisuke Iida, Tetsuya Manabe, "Distributed spatial mode dispersion measurement along strongly coupled multicore fibers based on the correlation analysis of Rayleigh backscattering amplitudes," *Optics Express* **25**(24), 29650-29658 (2017).
3. Shingo Ohno, Daisuke Iida, Kunihiro Toge, Tetsuya Manabe, "High-resolution measurement of differential mode delay of few-mode fiber using phase reference technique for swept-frequency interferometry," *Optical Fiber Technology* **40**, 56-61 (2018).

## International conferences related to this thesis

1. Shingo Ohno, Daisuke Iida, Kunihiro Toge, Tetsuya Manabe, "Long-range C-OFDR measurement of Rayleigh scatter signature of fiber beyond laser coherence length," in *Technical Digest of the Optical Fiber Communication Conference (OFC2016)*, W4F.4, Anaheim, USA, March 2016.
2. Shingo Ohno, Daisuke Iida, Kunihiro Toge, Tetsuya Manabe, "Nondestructive characterization of differential mode delay in few-mode fiber link using Rayleigh backscattering spectral shifts," in *Technical Digest of the Optical Fiber*

*Communication Conference (OFC2017)*, Th4H.2, Los Angeles, USA, March 2017.

3. Shingo Ohno, Daisuke Iida, Kunihiro Toge, Tetsuya Manabe, "Distributed spatial mode dispersion measurement along strongly coupled multicore fibre with C-OFDR," in *Proceedings of the 43rd European Conference on Optical Communication (ECOC2017)*, Tu.1.A.5, Gothenburg, Sweden, September 2017.

### **Domestic conferences related to this thesis**

1. 大野慎悟, 岡本達也, 戸毛邦弘, 真鍋哲也, "位相雑音補償OFDRによる長距離レイリー散乱光波形の再現性評価", 2014年電子情報通信学会ソサイエティ大会, B-13-19, 徳島大学, 徳島, 2014年9月.
2. 大野慎悟, 岡本達也, 戸毛邦弘, 真鍋哲也, "C-OFDRで観測されるレイリー散乱光波形の再現性に関する考察", 2015年電子情報通信学会総合大会, B-13-31, 立命館大学, 草津, 2015年3月.
3. 大野慎悟, 飯田大輔, 戸毛邦弘, 真鍋哲也, "C-OFDRで観測されるレイリー散乱光波形を用いた長距離温度分布測定", 2015年電子情報通信学会ソサイエティ大会, B-13-19, 東北大学, 仙台, 2015年9月.
4. 大野慎悟, 飯田大輔, 戸毛邦弘, 真鍋哲也, "C-OFDRで観測される長距離レイリー散乱光波形の再現性に関する検討", 2015年度第6回光ファイバ応用技術研究会, OFT2015-69, 沖縄大学, 那覇, 2016年2月.
5. 大野慎悟, 飯田大輔, 戸毛邦弘, 真鍋哲也, "C-OFDRで観測されるレイリー散乱光波形を用いた温度分布測定の測定距離の拡大", 2016年電子情報通信学会総合大会, B-13-10, 九州大学, 福岡, 2016年3月.
6. 大野慎悟, 飯田大輔, 戸毛邦弘, 真鍋哲也, "位相比較周波数掃引光干渉法

## List of publications and awards

- による2モード光ファイバの高分解能DMD測定”，2016年電子情報通信学会ソサイエティ大会，B-13-15，北海道大学，札幌，2016年9月.
7. 大野慎悟，飯田大輔，戸毛邦弘，真鍋哲也，“位相雑音を補償した周波数掃引光干渉信号の位相比較による数モードファイバの高分解能DMD測定”，第30回光通信システムシンポジウム，P-9，東レ総合研修センター，三島，2016年12月.
  8. 大野慎悟，飯田大輔，戸毛邦弘，真鍋哲也，“位相比較周波数掃引光干渉法による数モード光ファイバのDMD測定の高分解能化”，2016年度第6回光ファイバ応用技術研究会，OFT2016-47，大阪府立大学 I-site なんば，大阪，2017年2月.
  9. 大野慎悟，飯田大輔，戸毛邦弘，真鍋哲也，“位相比較周波数掃引光干渉法を用いたDMD測定におけるモード結合の影響”，2017年電子情報通信学会総合大会，B-13-7，名城大学，名古屋，2017年3月.
  10. 大野慎悟，飯田大輔，戸毛邦弘，真鍋哲也，“C-OFDRを用いた強結合マルチコアファイバの空間モード分散分布測定”，2017年電子情報通信学会ソサイエティ大会，B-13-15，東京都市大学，東京，2017年9月.
  11. 大野慎悟，戸毛邦弘，飯田大輔，真鍋哲也，“後方レイリー散乱光干渉パターンを用いた強結合型マルチコアファイバの空間モード分散分布測定”，2017年度第4回光ファイバ応用技術研究会，OFT2017-48，関西大学，大阪，2017年11月.
  12. 大野慎悟，戸毛邦弘，飯田大輔，真鍋哲也，“強結合型マルチコアファイバの空間モード分散分布測定法における測定精度向上に関する検討”，2018年電子情報通信学会総合大会，B-13-19，東京電機大学，東京，



2018年3月.

## Patents related to this thesis

1. 大野慎悟, 伊藤文彦, 岡本達也, 高橋央, “光ファイバの伝搬定数測定装置及び方法”, 特願2014-044155, 2014年3月出願.
2. 大野慎悟, 岡本達也, 戸毛邦弘, 真鍋哲也, 高橋央, “光ファイバの温度・歪み分布測定方法および装置”, 特願2014-179599, 2014年9月出願.
3. 大野慎悟, 岡本達也, 戸毛邦弘, 真鍋哲也, “分岐を有する長距離光ファイバの試験方法、及び装置”, 特願2015-018486, 2015年2月出願.
4. 大野慎悟, 戸毛邦弘, 飯田大輔, 真鍋哲也, “伝搬モード間群遅延差測定方法及び伝搬モード間群遅延差測定システム”, 特願2015-243754, 2015年12月出願.
5. 大野慎悟, 飯田大輔, 戸毛邦弘, 真鍋哲也, “光ファイバの後方レイリー散乱光波形解析方法及び光ファイバの後方レイリー散乱光波形解析装置”, 特願2016-018792, 2016年2月出願.
6. 大野慎悟, 戸毛邦弘, 飯田大輔, 真鍋哲也, “空間チャネル間伝搬遅延時間差測定装置及び空間チャネル間伝搬遅延時間差測定方法”, 特願2016-143952, 2016年7月出願.
7. 大野慎悟, 飯田大輔, 戸毛邦弘, 真鍋哲也, “空間チャネル間伝搬遅延時間差測定方法及び空間チャネル間伝搬遅延時間差測定装置”, 特願2016-240489, 2016年12月出願.
8. 大野慎悟, 戸毛邦弘, 飯田大輔, 真鍋哲也, “空間チャネル間伝搬遅延時間差測定装置及び空間チャネル間伝搬遅延時間差測定方法”, 特願2017-

## List of publications and awards

- 017107, 2017年2月出願.
9. 大野慎悟, 飯田大輔, 戸毛邦弘, 真鍋哲也, “温度・歪センシング装置及び温度・歪センシング方法”, 特願2017-041300, 2017年3月出願.
  10. 大野慎悟, 飯田大輔, 戸毛邦弘, 真鍋哲也, “空間モード分散測定方法及び空間モード分散測定装置”, 特願2017-107670, 2017年5月出願.
  11. 大野慎悟, 飯田大輔, 戸毛邦弘, 真鍋哲也, “空間多重光伝送路評価装置及び方法”, 特願2017-139514, 2017年7月出願.
  12. 大野慎悟, 飯田大輔, 戸毛邦弘, 真鍋哲也, “光反射測定装置及びその方法”, 特願2017-177149, 2017年9月出願.
  13. 大野慎悟, 戸毛邦弘, 真鍋哲也, “光スペクトル線幅演算方法、装置およびプログラム”, 特願2018-075087, 2018年4月出願.

## Papers related to other works

1. Shingo Ohno, Satoru Adachi, Reina Kaji, Syun-ichi Muto, Hirotaka Sasakura, “Optical anisotropy and photoluminescence polarization in single InAlAs quantum dots,” *Applied Physics Letters* **98**, 161912/1-3 (2011).
2. Reina Kaji, Shingo Ohno, Takahito Hozumi, Satoru Adachi, “Effects of valence band mixing on hole spin coherence via hole-nuclei hyperfine interaction in InAlAs quantum dots,” *Journal of Applied Physics* **113**, 203511/1-6 (2013).
3. Chihiro Kito, Hiroshi Takahashi, Kunihiro Toge, Shingo Ohno, Tetsuya Manabe, “Field measurement of PON branches with end-reflection assisted Brillouin analysis,” *Journal of Lightwave Technology* **34**(19), 4454-4459 (2016).

## International conferences related to other works

1. Shingo Ohno, Reina Kaji, Satoru Adachi, “Optical anisotropy and polarization states in individual self-assembled InAlAs quantum dots,” in *6th International School and Conference on Spintronics and Quantum Information Technology (SPINTECH6)*, WP-45, Matsue, Japan, August 2011.
2. Satoru Adachi, Shingo Ohno, Reina Kaji, Shun-ichi Muto, “Strain-induced valence-band mixing on photoluminescence polarization in individual quantum dots,” in *12th International Conference on Optics of Excitons in Confined Systems (OECS12)*, Paris, France, September 2011.
3. Reina Kaji, Shingo Ohno, Takahito Hozumi, Satoru Adachi, “Impact of band mixing to heavy hole spin dephasing induced by nuclear field fluctuation,” in *18th International Conference on Electron Dynamics in Semiconductors, Optoelectronics and Nanostructures (EDISON18)*, We1-2, Matsue, Japan, July 2013.
4. Reina Kaji, Takahito Hozumi, Shingo Ohno, Satoru Adachi, “Electron and hole g-factor measurements via optically-induced nuclear spin polarizations in single InAs/GaAs quantum rings, in *13th International Conference on Optics of Excitons in Confined System (OECS13)*, Tu2-5, Rome, Italy, September 2013.

## Domestic conferences related to other works

1. 大野慎悟, 鍛冶怜奈, 足立智, 武藤俊一, “自己集合半導体量子ドットにおける光学異方性”, 第46回応用物理学会北海道支部/第7回日本光学会北海道地区 合同学術講演会, B-9, 室蘭工業大学, 室蘭, 2011年1月.
2. 大野慎悟, 鍛冶怜奈, 足立智, 武藤俊一, “自己集合半導体量子ドットでの光学異方性と発光の偏光状態変化”, 第58回春季応用物理学関係連合講演

## List of publications and awards

- 会, 5 p-KV-3, 神奈川工科大学, 厚木, 2011年3月.
3. 大野慎悟, 鍛冶怜奈, 足立智, 武藤俊一, “単一量子ドットの光学異方性: 異方的交換相互作用と歪誘起価電子帯混合”, 第72回秋季応用物理学会学術講演会, 1 p-K-4, 山形大学, 山形, 2011年8月.
  4. 大野慎悟, 鍛冶怜奈, 足立智, 武藤俊一, “自己集合量子ドットの対称性低下によるスピン状態混合: 光学異方性からの考察”, 第59回春季応用物理学関係連合講演会, 17 p-E 1-1 (講演奨励賞受賞記念講演), 早稲田大学, 東京, 2012年3月.
  5. 鍛冶怜奈, 大野慎悟, 穂積貴人, 足立智, “単一量子ドットにおける核磁場揺らぎの実測と電子・正孔スピン緩和”, 第17回半導体スピン工学の基礎と応用研究会 (PASPS-17), 九州大学, 福岡, 2012年12月.
  6. 大野慎悟, 鍛冶怜奈, 穂積貴人, 足立智, “InAlAs量子ドットでの価電子帯の非対称結合効果”, 第60回応用物理学会春季学術講演会, 28 p-G 20-6, 神奈川工科大学, 厚木, 2013年3月.
  7. 鬼頭千尋, 高橋央, 戸毛邦弘, 大野慎悟, 真鍋哲也, “遠端反射ブリルアン利得解析法による分岐下部損失フィールド測定”, 2016年電子情報通信学会総合大会, B-13-15, 九州大学, 福岡, 2016年3月.

## Patents related to other works

1. 飯田大輔, 戸毛邦弘, 大野慎悟, 真鍋哲也, “光ファイバ振動検知センサおよびその方法”, 特願2017-135691, 2017年7月出願.
2. 古敷谷優介, 大野慎悟, 飯田大輔, 戸毛邦弘, 真鍋哲也, “光時間領域反射測定方法および光時間領域反射測定装置”, 特願2017-176164, 2017年9月出願.

3. 古敷谷優介, 飯田大輔, 大野稔悟, 戸毛邦弘, 真鍋哲也, “光時間領域反射測定方法および光時間領域反射測定装置”, 特願 2017-176166, 2017年9月出願.

## **Awards**

1. 第31回応用物理学会講演奨励賞, 公益社団法人応用物理学会, 2012年3月受賞.
2. 2017年光ファイバ応用技術研究会奨励賞, 一般社団法人電子情報通信学会光ファイバ応用技術研究会, 2018年3月受賞.